Lehrstuhl für Biomedizinische Physik
Technische Universität München

K-edge subtraction and X-ray fluorescence imaging at the Munich Compact Light Source

September 2020

Stephanie Kulpe
PhD Thesis

Supervisor:
Prof. Dr. Franz Pfeiffer

Technische Universität München

Technische Universität München
Physik Department
Lehrstuhl für Biomedizinische Physik

K-EDGE SUBTRACTION AND X-RAY FLUORESCENCE IMAGING AT THE MUNICH COMPACT LIGHT SOURCE

Stephanie Kim Kulpe

Vollständiger Abdruck der von der Fakultät für Physik der Technischen Universität München zur Erlangung des akademischen Grades eines

Doktors der Naturwissenschaften (Dr. rer. nat.)

genehmigten Dissertation.

Vorsitzende:	Prof. Dr. Karen Alim
Prüfer der Dissertation:	1. Prof. Dr. Franz Pfeiffer
	2. Prof. Dr. Jan J. Wilkens

Die Dissertation wurde am 29.09.2020 bei der Technischen Universität München eingereicht und durch die Fakultät für Physik am 09.12.2020 angenommen.

Abstract

X-ray imaging is an invaluable tool for non-destructive material testing and commonly used in clinical diagnosis. While ongoing research aims at advancing conventional X-ray devices and the applied imaging techniques, the polychromatic nature of the used X-ray spectra will eventually limit the range for further improvements. At the same time, novel imaging techniques using monochromatic X-ray beams are being developed at synchrotron facilities. In contrast to a polychromatic X-ray beam that will be altered in energy distribution when passing through a body, a monochromatic beam can be optimized in energy for the specific imaging application and enable a reduction in dose while optimizing contrast. One imaging technique that takes advantage of a monochromatic X-ray beam is K-edge subtraction imaging (KES). It was first demonstrated at a synchrotron facility in 1983 and was soon proposed as an alternative to digital subtraction angiography (DSA), an imaging technique commonly used for coronary angiography in clinical imaging. Like for most X-ray imaging methods, the image contrast in DSA and KES imaging arises from differences in absorption. However, also the fluorescence signal of a sample can give valuable information. X-ray fluorescence (XRF) imaging can be used to determine elemental concentrations in a tissue sample and help evaluate the tissue health status. Additionally, this method is commonly used for non-destructive examinations of, e.g., cultural heritage objects.

In order to provide a monochromatic X-ray beam in a laboratory environment, compact synchrotron sources based on the principle of inverse Compton scattering have been developed over the past decades. They produce a quasi-monochromatic beam with tunable energy and a brilliance between the one of a rotating anode source and a third generation synchrotron. Additionally, the costs for installation, maintenance and operation of inverse Compton sources (ICSs) are significantly lower than for synchrotron facilities. This facilitates the access to a monochromatic X-ray beam and enables the transfer of imaging techniques that were limited to synchrotron facilities into a laboratory or pre-clinical environment.

For this thesis, KES and XRF were implemented at the Munich Compact Light Source (MuCLS) and their use for biomedical applications was investigated. KES experiments for angiography and fluoroscopy were performed both in projection and three-dimensional imaging as well as simulating a dynamically changing sample. It was shown that KES in computed tomography (CT) allows for the complete separation of iodine and calcium, which is a common issue in clinical imaging. Additionally, in dynamic KES there were significantly less artifacts compared to temporal subtraction, which is state of the art today. XRF was used to determine elemental concentrations of different trace elements in solutions and also to investigate its possible application for the reconstruction of a degraded daguerreotype. Additionally, XRF allowed for the determination of the contrast agent concentration in stained tissue samples. The results imply that imaging at a compact synchrotron source can provide similar benefits as using a synchrotron beam. Although further improvements of the setup and the

X-ray source are needed, both investigated imaging techniques are good candidates for future clinical application.

Zusammenfassung

Röntgenbildgebung ist ein wertvolles Instrument für die zerstörungsfreie Untersuchung von Materialien und wird häufig in der klinischen Diagnostik verwendet. Während die gegenwärtige Forschung zum Ziel hat, konventionelle Röntgengeräte und -bildgebungsverfahren stetig weiterzuentwickeln, wird letztlich die polychromatische Natur der verwendeten Röntgenspektren die Möglichkeit weiterer Entwicklung limitieren. Gleichzeitig werden neue Bildgebungsverfahren, die monochromatische Röntgenstrahlen verwenden, an Synchrotronanlagen entwickelt. Im Gegensatz zu polychromatischen Röntgenstrahlen, deren Energieverteilung sich beim Durchqueren eines Körpers verändert, kann die Energie des monochromatischen Strahls für die verwendeten Bildgebungsmethoden optimiert werden und so zu einer Dosisreduktion bei gleichzeitigem Kontrastgewinn führen. Eine Bildgebungsmethode, die die Vorteile eines monochromatischen Röntgenstrahls ausnutzt, ist die K-Kanten Subtraktionsbildgebung. Sie wurde 1983 zum ersten Mal an einer Synchrotronquelle angewandt und wurde schnell als mögliche Alternative zur digitalen Subtraktionsangiographie, einer Bildgebungsmethode, die häufig für Koronarangiographie im klinischen Alltag Verwendung findet, vorgeschlagen. Wie bei vielen anderen Röntgenbildgebungsmethoden, entsteht der Bildkontrast bei DSA und K-Kantensubtraktionsbildgebung aus Unterschieden in der Absorption. Allerdings kann auch das Fluoreszenzsignal einer Probe wertvolle Informationen liefern. Röntgenfluoreszenz-Bildgebung kann verwendet werden, um die elementare Konzentration in Gewebeproben zu bestimmen, und somit helfen, den Gesundheitszustand ebendieser zu beurteilen. Außerdem wird diese Methode häufig angewandt, um zerstörungsfrei Kulturobjekte zu untersuchen, zum Beispiel um degradierte Bilder zu rekonstruieren oder mehr über die Herstellung eines Gemäldes in Erfahrung zu bringen.

Um einen monochromatischen Röntgenstrahl in einer Laborumgebung verfügbar zu machen, werden seit mehreren Jahrzehnten kompakte Synchrotronquellen entwickelt, die auf dem Prinzip der inversen Comptonstreuung basieren. Diese Quellen produzieren einen quasi-monochromatischen, in der Energie verstellbaren Röntgenstrahl mit einer Brillianz zwischen der einer Drehanode und eines Synchrotrons der dritten Generation. Zusätzlich sind die Kosten für die Installation, die Wartung und den Betrieb einer inversen Comptonquelle deutlich niedriger als für eine Synchrotron-Anlage. Dies vereinfacht den Zugang zu einem monochromatischen Röntgenstrahl und erlaubt den Transfer von bildgebenden Verfahren, die bisher nur an Synchrotronstrahlungsquellen durchgeführt werden konnten, in eine Labor- oder präklinische Umgebung.

Für diese Dissertation wurden K-Kanten-Subtraktions- und Röntgenfluoreszenz-Bildgebung an der Munich Compact Light Source (MuCLS) angewandt und ihre Eignung für biomedizinische Anwendungen untersucht. K-Kanten-Subtraktionsexperimente für Angiographie und Fluoroskopie wurden sowohl für Projektionsaufnahmen als auch für dreidimensionale Bildgebung durchgeführt. Zusätzlich wurde eine sich dynamisch verändernde Probe simuliert. Es wurde hierbei gezeigt, dass K-Kanten-Subtraktion in Computertomografie (CT) die vollständige Trennung von Iod und Calcium erlaubt, was

aktuell häufig in klinischer Bildgebung nicht möglich ist. Außerdem traten bei der dynamischen K-Kanten-Subtraktionsbildgebung deutlich weniger Artefakte auf als in der zeitlichen Subtraktion, die der heutige klinische Standard ist. Röntgenfluoreszenz wurde verwendet, um die Konzentrationen von verschiedenen Spurenelementen in Lösung zu bestimmen und die Anwendung dieser Bildgebungsmethode für die Rekonstruktion eines degradierten Daguerreotypen wurde erörtert. Zusätzlich konnten mit Hilfe der Röntgenfluoreszenz die Konzentration des Kontrastmittels in einer gefärbten Gewebeprobe bestimmt werden. Die Ergebnisse implizieren, dass die Bildgebung an einer kompakten Synchrotronquelle ähnliche Vorteile bietet wie die Bildgebung an einem Synchrotron. Obwohl eine weitere Entwicklung der Versuchsaufbauten und der Röntgenquelle notwendig sind, sind die beiden Bildgebungsmethoden vielversprechende Kandidaten für zukünftige klinische Anwendungen.

Contents

1 Introduction

X-rays are an invaluable tool in our daily lives. They are used in airport security systems, for non-destructive material testing and most importantly for medical purposes. X-ray imaging is used for the diagnosis of various diseases and provides information about the inside of the body that is not accessible otherwise. Therefore, the improvement of X-ray imaging techniques through the development of technical equipment as well as processing algorithms is an important field of research. However, even today, medical diagnosis is compromised by image artifacts that arise partially from the polychromatic X-ray spectra provided by the clinical X-ray sources. Additionally, the awareness for the applied radiation dose has increased over the past decades so that many efforts are made to reduce it.

With the development of synchrotron sources, monochromatic, high flux and coherent X-ray beams have become available and also of interest for medical applications. With this, new imaging techniques were developed, taking advantage of the characteristics of these novel X-ray sources. One of these techniques is K-edge subtraction imaging (KES). It was mainly developed to overcome the issue of strong motion artifacts in cardiovascular imaging, such as coronary angiography, and to reduce the risk for patients in interventional procedures [Rubenstein, 1981; Rubenstein, 1986]. It has been shown that KES at synchrotrons allows for imaging with reduced or no artifacts [Houk, 1979; Elleaume, 2000]. Also, this imaging method could possibly solve the issue of high contrast agent concentrations needed for clinical imaging. High contrast agent concentrations stress the kidneys, especially of patients with reduced kidney function. Studies have shown that KES allows for the intravenous injection of contrast agent while producing improved image quality compared to conventional digital subtraction angiography [Elleaume, 2000; Schültke, 2005], thus reducing the overall quantity of injected contrast agent.

Synchrotron radiation has also been extensively used to examine the spatial distribution of trace elements in animal and human tissue. Since the X-ray fluorescence (XRF) signal of an element in a sample is directly proportional to its concentration, the concentration can be determined using appropriate calibration methods. Studies have shown that the concentration of several biologically relevant elements like zinc, iron, copper, calcium and lead show significant differences between normal, healthy and diseased tissue [Gherase, 2020]. These can be markers for different types of cancer, e.g., prostate cancer [Ide-Ektessabi, 2002] or ductal carcinoma in breast tissue [Silva, 2009], or give indication for diseases like Parkinson's or Alzheimer's [Popescu, 2009; Miller, 2006].

Although both KES and XRF contain specific diagnostic information not available in polychromatic imaging, they are not commonly applied in clinical diagnostics. Es-

pecially KES is dependent on monochromatic synchrotron radiation and the limited access to these large scale facilities prevents its clinical application. Additionally, the typical beam size provided by a synchrotron is far smaller than the beam size needed for clinical imaging. Over the past decades, compact synchrotron sources have been developed as an alternative means to serve the need for high monochromatic flux X-ray beams in a laboratory environment [Huang, 1998; Jacquet, 2014; Bacci, 2016]. Currently, many projects to build inverse Compton sources are ongoing, such as the cERL based laser-Compton X-ray source at KEK [Akagi, 2016], STAR [Bacci, 2016], the ASU Compact XFEL [Graves, 2017] and ThomX [Variola, 2011]. Another one is installed at the Munich Compact Light Source (MuCLS). Here, a Compact Light Source (CLS, Lyncean Technologies Inc., Fremont, USA), a storage ring-based inverse Compton source (ICS), is used to produce a quasi-monochromatic X-ray beam with tunable energy [Eggl, 2016]. Past experiments have shown that the monochromatic beam of this source provides similar benefits for imaging as a synchrotron X-ray beam. At the MuCLS, angiography images with improved contrast-to-noise ratio (CNR) are produced compared to images acquired with a conventional polychromatic X-ray spectrum [Eggl, 2017]. This also holds true for monochromatic CT, where the image quality is significantly improved compared to polychromatic CT [Achterhold, 2013].

In the course of this thesis, possible applications of KES and XRF were investigated at the MuCLS. While the main focus lay on biomedical imaging, XRF experiments were also performed to determine its usefulness for the reconstruction of degraded cultural heritage objects.

Outline

This thesis presents work on K-edge subtraction and X-ray fluorescence imaging at the MuCLS with the main focus on biomedical applications. The theoretical background of X-ray imaging is presented in Chapter 2. Chapter 3 introduces different types of X-ray sources and sets the MuCLS in context to other sources. Generally, KES is a common procedure at synchrotron sources. However, the implementation of this imaging method at the MuCLS required several developments that are shown in Chapter 4. Chapters 5, 6 and 7 present the experimental results obtained within this thesis. Hereby, the two former chapters focus on KES in projection and CT for static samples and show the developments needed in order to apply this method to dynamically changing samples. Chapter 7 is about the XRF experiments performed both for the reconstruction of degraded cultural heritage objects and for the elemental concentration analysis in samples for potential biomedical applications. Finally, a conclusion and outlook is given in Chapter 8.

2 Principles of absorption based X-ray imaging

In the beginnings of X-ray imaging, measurement times were typically several hours. Since then, technical development has reduced acquisition times and improved image quality. Today, X-rays are an invaluable tool for medical diagnostics and also nondestructive material testing. Therefore, this chapter summarizes the theoretical background of X-radiation and its detection to the extent necessary for understanding the findings of this thesis. If not stated elsewise, the information in this chapter is based on chapters 1 and 7 of "Elements of Modern X-ray Physics" by Jens Als-Nielsen and Des McMorrow [Als-Nielsen, 2011] and on chapter 2 of "An Introduction to Synchrotron Radiation" by Philip Willmott [Willmott, 2011].

2.1 X-rays as electromagnetic waves

X-rays are electromagnetic waves with wavelengths in the order of an ångström (10^{-10} m), with corresponding energies ranging from about 100 eV to 100 keV. One differentiates between so-called soft and hard X-rays, with hard X-rays having an energy of more than 5-10 keV [Attwood, 1999]. The latter are commonly used in medical radiography as they have a high penetration ability. For simplicity the magnetic field of the electromagnetic wave is neglected in the following. Mathematically, the electric field of an X-ray traveling in vacuum can be described by:

$$\boldsymbol{E}(\boldsymbol{r}, t) = \hat{\boldsymbol{e}}\, E_0\, e^{i(\boldsymbol{k}\cdot\boldsymbol{r}-\omega t)}, \tag{2.1}$$

where $(\boldsymbol{r}, t)$ are the position vector and the time, $\boldsymbol{E}$ is the electric field with norm E_0, $\hat{\boldsymbol{e}}$ is the unit vector and $\omega = kc$ is the angular frequency with c and k being the speed of light and the norm of the wave vector, respectively.

2.2 Interaction of X-rays with matter

In X-ray imaging, the image contrast arises from different interactions of X-ray photons with matter. The type of interaction thereby depends on the energy of the photon and the properties of the matter the photon penetrates. For the energy range of X-rays used in this thesis, three relevant interaction mechanisms exist, that are shown in Fig. 2.1: photoelectric absorption, elastic (Thomson) and inelastic (Compton) scattering. These are described in the following.

Photoelectric absorption

If the energy of an X-ray photon is equal or above the binding energy of the binding energy of an electron in an atomic shell, it can be fully absorbed by the atom. An electron from an inner shell is thereby released from the atom. Its kinetic energy is equal to the difference between binding energy and energy of the incident photon. An electron from an outer shell subsequently fills the remaining hole in the inner shell. During this transition, the electron releases the energy difference between these levels either via photon emission (fluorescence) or by liberation of another bound electron into the continuum (Auger electron emission). The probability of an X-ray photon to interact with an electron via photoelectric absorption can be described with the absorption cross section σ_p which depends on the atomic number Z of the interacting atom and the energy E of the incident photon via

$$\sigma_p \propto \frac{Z^4}{E^3}. \tag{2.2}$$

In imaging this dependence leads to a contrast between materials with different (effective) atomic numbers. Additionally, this means that low energy photons will be absorbed more strongly than high energy photons. This energy-dependent absorption enhances high-energy components of a polychromatic spectrum relative to low-energy ones while passing through an object. After the object, the apparent spectrum's mean energy is shifted towards higher energies and its bandwidth narrowed down. This process is called beam-hardening [Bille, 2002] and may lead to artifacts, especially in tomographic imaging.

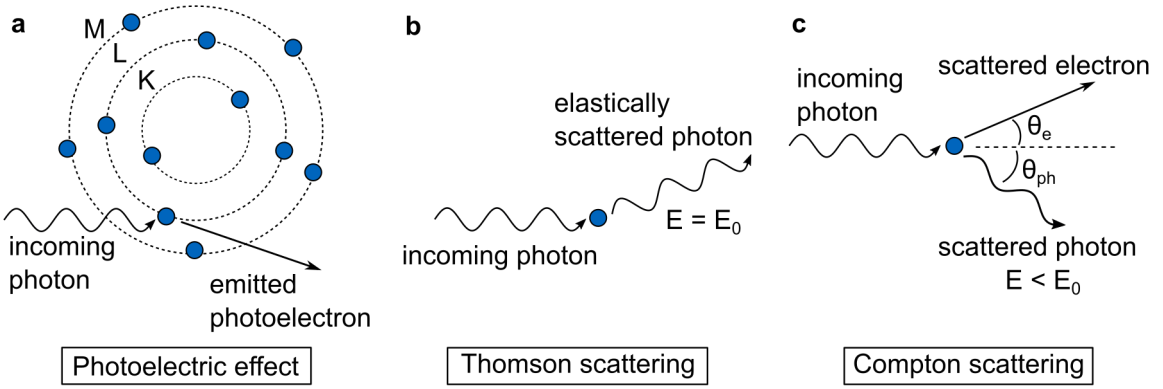

Figure 2.1: Interaction mechanisms of X-rays with matter: **a** Photoelectric effect: The incoming photon is absorbed by an electron in the inner shell which is consequently emitted into the continuum; **b** Thomson scattering: The incoming photon is scattered elastically at an electron, the scattered photon has the same energy as the initial photon; **c** Compton scattering: The incoming photon is scattered inelastically at an electron, transferring a part of its energy to the electron.

Thomson scattering

Thomson scattering is the process of elastic scattering of an X-ray at a (quasi) free electron. The scattering process can be described as a driven harmonic oscillator of a charged particle. The oscillating electric field of the incoming electromagnetic wave accelerates the electron, resulting in the emission of dipole radiation in parallel to the electric field vector. The outgoing wave is identical to the incoming wave with a phase shift of 180°, no energy is transferred to the electron. The ability of a free electron to scatter an electromagnetic wave is determined by the Thomson scattering length. It is defined as

$$r_0 = \frac{e^2}{4\pi\varepsilon_0 mc^2} = 2.82 \times 10^{-5}\,\text{Å}, \tag{2.3}$$

with e the charge of the electron, ε_0 the electric field constant and mc^2 the rest mass of the electron.

Compton scattering

In Compton scattering, the electromagnetic wave interacts with electrons in the outer shells of the atom. In the particle view, a photon collides with an electron, transferring momentum and kinetic energy from the photon to the electron. This process is inelastic, as the scattered photon will have a lower energy. The energy loss can be calculated by applying the conservation of momentum and energy, thus

$$\lambda - \lambda_0 = \lambda_C\,(1 - \cos\theta_{\text{ph}}), \tag{2.4}$$

where λ_0 is the wavelength of the incoming photon, λ is the wavelength of the scattered photon, θ_{ph} is the angle by which the photon is scattered and λ_C is the scattering length with $\lambda_C = \frac{h}{mc} = 2.43 \times 10^{-2}\,\text{Å}$.

Complex refractive index

In the wave picture, the interactions mentioned above can be summarized in the complex refractive index n:

$$n = 1 - \delta + i\beta, \tag{2.5}$$

with the imaginary part β being the absorption and the real part δ being the contribution to the phase shift. In the X-ray regime δ is in the order of 10^{-5} and β is even smaller. When the wave propagates through vacuum the refractive index n is 1. When entering into matter the wave number changes from $\boldsymbol{k} \cdot 1$ to $\boldsymbol{k} \cdot n$. The electromagnetic wave at an arbitrary point in space and time can then be described by:

$$\boldsymbol{E}(\boldsymbol{r}, t) = \boldsymbol{E_0} e^{i(n\boldsymbol{k}\cdot\boldsymbol{r} - \omega t)} = \underbrace{\boldsymbol{E_0} e^{i(\boldsymbol{k}\cdot\boldsymbol{r} - \omega t)}}_{\text{wave in vacuum}} \cdot \underbrace{e^{-i\boldsymbol{k}\cdot\boldsymbol{r}\delta}}_{\text{phase shift}} \cdot \underbrace{e^{-\boldsymbol{k}\cdot\boldsymbol{r}\beta}}_{\text{attenuation}}, \tag{2.6}$$

where the exponential terms account for the wave propagation in vacuum, the phase shift introduced by the interaction with matter and the attenuation. The attenuation

is associated with a loss in intensity which can be calculated by the absolute value of Eq. 2.6:

$$I = |\boldsymbol{E}(\boldsymbol{r}, t)|^2 = |E_0 e^{-\boldsymbol{k}\cdot\boldsymbol{r}\beta}|^2 = I_0 e^{-2\beta k r} = I_0 e^{-\mu r}. \tag{2.7}$$

Eq. 2.7 is referred to as the Lambert-Beer law with $\mu = 2\beta k$, the linear absorption coefficient. It describes the loss in intensity, $e^{-\mu d}$, of the beam with initial intensity I_0 when traveling through a medium with attenuation coefficient μ and thickness d.

2.3 Attenuation of X-rays

As already mentioned in Ch. 2.2, an X-ray beam is attenuated when it propagates through matter. This attenuation is described by the Lambert-Beer-Law:

$$I(x) = I_0 \exp[-\mu x], \tag{2.8}$$

with I_0 being the initial intensity of the beam, μ the linear attenuation coefficient of the material and $I(x)$ the intensity of the beam after propagating the distance x through the material (cf. Fig. 2.2).

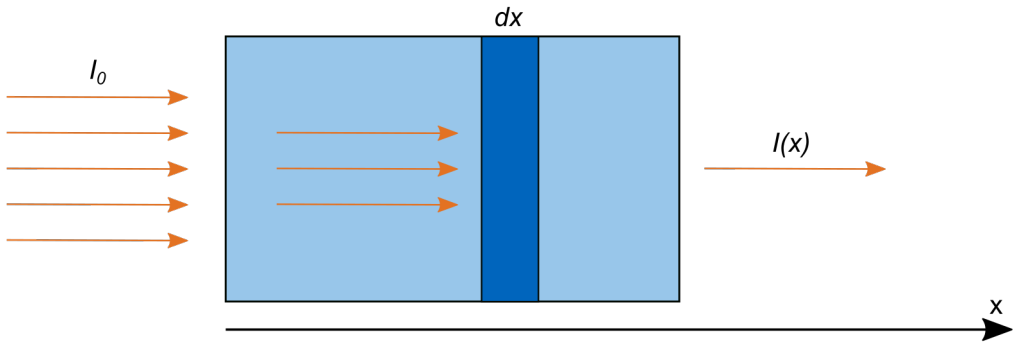

Figure 2.2: Attenuation of a beam passing through a sample: An X-ray beam with the initial intensity I_0 propagates through a material with attenuation coefficient μ. The intensity of the beam decreases according to the Lambert-Beer law.

The absorption coefficient is determined by the electron density and the electron binding energy of the material. Therefore, μ is different for a chemical substance existing in different allotropic forms, which have different densities, e.g., allotropes of carbon (diamond, graphite etc.). At the same time, compounds of different chemical substances may contain the same number of electrons and have similar densities, so their absorption properties can be similar. One therefore defines the absorption cross-section σ_a of an element. The relation between μ and σ_a is

$$\mu = \rho_a \sigma_a = \left(\frac{\rho_m N_A}{M}\right) \sigma_a, \tag{2.9}$$

with ρ_a, ρ_m, N_A and M being the atomic number density, the mass density, Avogadro's number and the molar mass, respectively.

In a composition of several materials, the probability of absorption in a layer $\mathrm{d}x$ is the sum over the individual atomic number densities $\rho_{a,j}$ times the absorption cross-sections $\sigma_{a,j}$, multiplied by the thickness $\mathrm{d}x$. The attenuation coefficient can be written as:

$$\mu = \sum_j \rho_{a,j}\sigma_{a,j}. \tag{2.10}$$

Additionally, for many X-ray sources the beam will usually not be monochromatic. In this case, the attenuation coefficient depends on the energy E and the thickness d of the different material types:

$$I(d) = \int_{E_{min}}^{E_{max}} I_0(E) \exp\left[-\int_0^d \mu(E,x)\mathrm{d}x\right] \mathrm{d}E, \tag{2.11}$$

where $\int_0^d \mu(E,x)\mathrm{d}x$ is the line integral, which simplifies to μd for homogeneous media.

2.3.1 Calculation of radiation dose

Although X-rays are an invaluable tool for medical diagnostics, the exposure to ionizing radiation is not without risk. When X-rays are absorbed in material, their energy is deposited inside of it and may cause damage in the deoxyribonucleic acid (DNA) of biological tissue. Therefore, in medical imaging dose regulation and optimization is a main aspect. While the infrequent use of X-ray or CT scans will not have negligible effects on a patient, multiple exposures to radiation over a short period of time can cause severe damage to cells and increase the risk for cancer [Mikla, 2014]. Although the experiments presented in this thesis are proof-of-principle, for some of them the delivered radiation dose was calculated. This chapter introduces the dose calculations performed for this thesis.

Air kerma

The kerma (kinetic energy released per unit mass) is defined as the sum of the initial kinetic energy $\mathrm{d}E$ of all charged particles liberated by uncharged ionizing particles in a volume element $\mathrm{d}V$ of mass $\mathrm{d}m$

$$K = \frac{\mathrm{d}E}{\mathrm{d}m} = \frac{1}{\rho}\frac{\mathrm{d}E}{\mathrm{d}V}, \tag{2.12}$$

with $\mathrm{d}m = \rho \mathrm{d}V$. Kerma is measured in units of Gray ([Gy] = J/kg) [Krieger, 2012; ICRP, 2012]. The kerma can be directly measured from the energy flux $\Psi = E\Phi$, with Φ being the photon flux, and the energy transfer coefficient μ_{tr}/ρ such that

$$K = \Psi \frac{\mu_{tr}}{\rho} = E\,\Phi\,\frac{\mu_{tr}}{\rho}. \tag{2.13}$$

Kerma can be calculated relative to different materials, usually water or air [Bille, 2002]. For dosimetry in diagnostic radiology, the International Atomic Energy Agency

(IAEA) recommends the usage of the air kerma [IAEA, 2007]. In radiography and fluoroscopy, the radiation dose is usually calculated by measuring the kerma in air and multiplying it with technical factors to obtain the patient dose [Mikla, 2014]. For computed tomography (CT) doses may be calculated from CTDI (computed tomography air-kerma dose index) and DLP (air-kerma dose-length product) measurements [Krieger, 2012].

Effective dose

The effective dose is the sum of the weighted equivalent doses in all tissues and organs of the body, given by the expression

$$E = \sum_T w_T H_T, \tag{2.14}$$

where H_T is the equivalent dose in organ or tissue T, and w_T is the weighting factor. The effective dose has the unit Sievert (Sv). The equivalent dose is derived from the mean organ absorbed dose D_T, i.e., the total amount of energy deposited in an organ (or tissue) T per mass of the organ, multiplied with a radiation weighting factor w_R accounting for the relative biological effectiveness of the incident radiation [Zankl, 1997; ICRP, 2012]:

$$H_T = D_T w_R. \tag{2.15}$$

For X-rays, the radiation weighting factor w_R is equal to unity, thus the absorbed and equivalent dose are numerically identical. The weighting factors w_T for different tissue types are mean values calculated by the International Commission on Radiological Protection (ICRP) from epidemiological measurements [Krieger, 2012]. The sum over all tissue types of the body is

$$\sum_T w_T = 1. \tag{2.16}$$

As neither organ equivalent nor effective dose are measurable quantities, conversion coefficients between organ doses and measurable dose quantities have been established. Usually, the organ and tissue dose conversion coefficients are calculated using radiation transport codes together with computational models of the human body [Zankl, 1997]. The IAEA International Code of Practice defines coefficients c such that

$$c = \frac{D_T}{K_{\text{air}}}, \tag{2.17}$$

with D_T being the organ dose and K_{air} the air kerma [IAEA, 2007]. The formula for the effective dose is

$$D_{\text{eff}} = K(E)_{\text{air}}\, f(E), \tag{2.18}$$

where $f(E)$ are the energy dependent conversion coefficients.

Research on these conversion coefficients is ongoing, especially for mammography, where dose limitations are an important aspect for screening programs. Several dose estimation methods have been developed, among others by Boone [Boone, 1999; Boone,

2002]. Coefficients for other organs have been calculated from Monte Carlo simulations, e.g., by Zankl et al. [Zankl, 1997]. The latter have been used for the experiments performed in this thesis.

2.3.2 Contrast-to-noise ratio (CNR)

The image quality required for a certain diagnostic objective limits the patient dose in medical imaging. Thus, image noise is a major factor limiting exposure times and therefore the minimum achievable dose [Mikla, 2014]. The contrast-to-noise ratio (CNR) is an important measure for image quality. It relates the contrast, i.e., the difference in the transmission signal, between two structures in the image to the noise level of the image. A CNR smaller than one hereby means that the contrast is smaller than the noise level. Thus the structures are not distinguishable. For the X-ray energies used for this thesis, the image contrast is mainly dominated by the photoelectric effect and therefore dependent on the attenuation coefficients of the materials [Bille, 2002].

The CNR between two regions of interest (ROIs) is calculated against the noise in the background region according to the following formula

$$\mathrm{CNR} = \frac{|S_{\mathrm{Ai}} - S_{\mathrm{Bi}}|}{\sqrt{\sigma^2_{\mathrm{back}}}}, \tag{2.19}$$

where S_{Ai} and S_{Bi} are the average signals in two ROIs containing structures of different materials and σ_{back} is the standard deviation in a background region [Desai, 2010; Bechara, 2012].

2.4 Use of contrast agents

X-ray absorption contrast between different tissue types is relatively low. In order to enhance the contrast between, e.g., blood vessels and surrounding tissues, a contrast agent can be injected. However, contrast agents can not only be used for the visualization of morphology but also for functional imaging, e.g., highlighting transport processes (e.g., in the bloodstream or the intestine), the elimination of substances (e.g., in kidney or liver) or barriers such as the blood-brain barrier.

Contrast in attenuation imaging is created by a difference of atomic numbers, material density and electron density between two substances or tissues. Therefore, the elemental composition of the contrast agent must be significantly different from the one of the biological tissue. Negative and positive contrast media were developed to achieve this task for different types of tissue. Negative contrast media have a lower atomic number, thus lower absorption, and positive ones a higher atomic number, thus higher absorption, than the tissue [Speck, 2018].

X-ray negative contrast agents are usually gases, mainly air or CO_2, that absorb less than the tissue or bone structures of the body. These are used, e.g., for imaging of the

joints [Dössel, 2016], for vascular imaging when the patient has an iodine allergy or for imaging of the large intestine as a second contrast agent.

Positive contrast media absorb X-rays more strongly than tissue structures. The most commonly used X-ray positive contrast agents are insoluble barium sulfate ($BaSO_4$) for imaging of the gastrointestinal tract and water-soluble contrast media for the evaluation of the vascular system, body cavities and organs. Additionally, heavy inert gases such as Xenon are used for respiratory imaging. Iodine-based contrast media are often applied for imaging of hollow cavities and organs of the body. They can be injected intravenously, e.g., for vascular imaging or imaging of the renal system, or given orally for imaging of the gastrointestinal tract if barium sulfate cannot be used (e.g., if there might be perforation of the intestine). For coronary catheter angiography, the contrast agent can also be applied directly in the investigated blood vessel. One distinguishes between ionic and non-ionic contrast media. Non-ionic contrast media are used more frequently in angiography since they have lower risk of causing vascular pain, endothelial damage and thrombosis than ionic contrast agents.

Although contrast media are typically safe and have low toxicity, there are some risks to the patient when they are applied. Generally, non-ionic contrast media are better tolerated than ionic ones as they cause less general reactions (e.g., allergic reactions), cause less osmolality-dependent effects (e.g., pain) and have better neural tolerance. The contrast media reactions can be classified into two groups: 1. General or largely dose-independent contrast media reactions and 2. Chemotoxic, local and cardiovascular effects and dose-dependent side-effects. Severe, general contrast media reactions are very rare and can be reduced by usage of non-ionic contrast media instead of ionic ones. Dose-dependent side effects include sensations of pain and heat, hyperthyroidism and renal impairment. Especially for patients with renal insufficiency, the latter is a high risk. Therefore, it is desired to reduce the amount of contrast media needed for those patients by switching to other imaging modalities or enhancing contrast by using subtraction techniques such as digital subtraction angiography [Speck, 2018].

2.5 Digital subtraction angiography (DSA)

Especially when imaging details in plain radiography that are overlapped by other substances like bone or tissue, special imaging methods are necessary, which often exploit the special properties of contrast agents. One of these methods is digital subtraction angiography (DSA). It is one of the most important techniques in the examination of blood vessels [Yamamoto, 2009]. DSA allows selective evaluation of arteries and veins without interfering background (e.g., bone) at a much lower contrast media concentration in the vascular regions of interest. In DSA, a series of images is acquired showing a bolus of injected contrast agent passing through vessels of interest. By subtracting an image obtained immediately before the injection of contrast agent (referred to as "mask") from the series of images obtained with contrast agent filling the target vessels, surrounding tissue can be removed [Tobis, 1983; Meijering, 1999; Speck, 2018].

2.5.1 History of Digital Subtraction Angiography

DSA was developed in the early 1970s when digital electronics became accessible for medical imaging. By 1978, the feasibility of DSA on human images was demonstrated and in 1980 prototype commercial DSA systems were introduced [Menken, 1985]. Especially intravenous DSA benefited from new technological developments and became a standard tool for medical diagnostics by the early 1980s [Pelz, 1985]. Since then, DSA has been developed to improve image quality and reduce imaging artifacts.

The subtraction technique is based on the assumption that the tissues surrounding the vessels remain unchanged in density and position during the imaging procedure. However, artifacts in DSA often occur due to misalignment of successive images in the sequence, e.g., due to patient motion [Meijering, 1999]. Several techniques have been developed to reduce artifacts and improve the diagnostic quality directly during image acquisition, e.g., automatic re-masking or dual-energy subtraction techniques [Brody, 1982]. Yet, these techniques are technically challenging so that post-processing algorithms were developed and used. A main challenge was also to reduce the computation time of the correction algorithms such that they are fast enough for the integration into clinical routine [Meijering, 1999]. Today, research on techniques and algorithms for the reduction of artifacts in DSA is ongoing, however the rapid motion of the heart, and the lung due to breathing are still challenging to correct [Yamamoto, 2009].

While DSA significantly improved the diagnostic quality, the applied dose varies depending on the imaged body region and is typically higher than for previously used angiographic methods [Zeitler, 1992]. Therefore, the search for methods that reduce the patient dose began soon after the introduction of DSA [Brody, 1982; Okamoto, 2000; Niu, 2015]. However, the reduction of radiation dose is usually associated with an increase of the noise level, thus impairing the image quality. Additionally, the use of electronic image processing often lead to a further increase in noise compared to traditionally used angiographic methods [Brody, 1982]. To maintain image quality while reducing radiation dose, denoising algorithms for DSA have been developed. Recently, applying these algorithms, studies have shown dose reduction by 75 % at the same image quality [Söderman, 2013].

To overcome the limitations of DSA, alternative imaging methods have been developed, e.g., for patients with contradictions to DSA. These techniques are mainly computed tomography angiography (CTA) [Knez, 2001; Mowatt, 2008; Achenbach, 2010], providing 3D information of the vascular system, and magnetic resonance angiography [Sandstede, 1999; Hartung, 2011], being a radiation-free imaging method.

2.5.2 Quantitative analysis

In DSA, two subsequent radiographs are acquired and subtracted from one another. In the first image, the “mask”, the blood vessels are imaged without contrast agent. Behind the patient the decreased X-ray beam intensity I_M

$$I_M = I_0\, e^{-\mu D} \tag{2.20}$$

can be measured, where I_0 is the initial beam intensity, μ is the mean attenuation coefficient and D is the thickness of the patient [Dössel, 2016]. Before or during the acquisition of the second image, a contrast agent is injected into the blood vessels. This changes the line integral in the blood vessels from μG to $\mu_I G$, μ_I being the attenuation coefficient of the contrast agent and G the thickness of the blood vessels. The intensity of the X-ray beam behind the patient I_F then changes to

$$I_F = I_0 \, e^{-[\mu(D-G)+\mu_I G]}. \tag{2.21}$$

The two images are then subtracted logarithmically pixelwise, resulting in:

$$\ln I_F - \ln I_M = \ln I_0 - \mu(D-G) - \mu_I G - \ln I_0 + \mu D = G(\mu - \mu_I) \approx -\mu_I G \tag{2.22}$$

as $\mu_I \gg \mu$ for biological tissue. Consequently, only the stained blood vessels remain. Therefore, the gray value in the resulting subtraction image is only dependent on the thickness of the blood vessel [Dössel, 2016].

This imaging method has the advantage that only the desired structures remain in the final image, enabling improved diagnostics. Yet, this method has drawbacks. The main problem faced when using this method are motion artifacts caused by respiration and cardiac motion. These lead to blurring of the images that can however be reduced with image post-processing techniques that are usually computationally complex [Yamamoto, 2009]. Additionally, the time span of the diagnostic is a limitation to this method. As the images have to be taken after one another with the interruption by the injection of the contrast agent, this examination method can be very time consuming and possible movements of the patients have to be corrected by image processing.

2.6 K-edge subtraction (KES) imaging

In contrast to DSA, K-edge subtraction (KES) imaging exploits the sharp increase of the photoelectric absorption at the K-edge of the contrast agent to enhance the visible difference between contrasted structures and surrounding tissue. This allows for acquisition of the images directly one after another or even simultaneously with special setups.

2.6.1 History of K-edge subtraction imaging

The principle of KES was first suggested by B. Jacobson in 1953, who proposed the use of monochromatic X-rays to increase contrast in absorption imaging. He proposed to exploit the energy dependence of the absorption coefficient for contrast generation as well as for concentration determination of an element in an object. To this end, he suggested the subtraction of two or more images acquired at different monochromatic X-ray energies to produce an image only showing the differences in absorption and the

concentration of an element in an object [Jacobson, 1953]. Although KES can also be implemented by filtering a polychromatic spectrum, this imaging method became more common in the 1980s combined with the increasing availability of monochromatic synchrotron radiation. The first studies of KES were performed by Rubenstein et al. [Rubenstein, 1981; Rubenstein, 1986] at the Stanford Synchrotron Radiation Laboratory demonstrating the feasibility of coronary angiography. The first *in vivo* KES images were made of the coronary arteries of an anesthetized dog [Hughes, 1985]. In the beginnings of KES, the main application was coronary angiography since there were great struggles in DSA to get artifact free images [Tobis, 1983] and safely perform the invasive procedures also concerning the use of high doses of contrast agent [Pelz, 1985; Thompson, 1989]. The developments in KES led to real time angiography of animals [Umetani, 1991; Umetani, 1993] and first results of human patients [Thompson, 1989; Dix, 1995]. Elleaume et al. thereby showed that the KES coronary angiography at synchrotrons provides improved image quality in comparison to DSA at a conventional X-ray source while reducing the risk for the patient using transvenous injection of contrast agent [Elleaume, 2000]. Afterwards, several other studies were performed demonstrating the benefits of KES for coronary [Dix, 2003; Bertrand, 2005] and neurovascular angiography [Schültke, 2005]. At the same time, KES was also applied in computed tomography [Thompson, 1984; Dilmanian, 1991]. Studies focused mainly on brain tumour vasculature [Le Duc, 2000; Suortti, 2000] and perfusion analysis [Nachaliel, 1992; Dilmanian, 1997]. However, the application of KES at synchrotrons has not been limited to angiography. Studies on functional lung imaging [Giacomini, 1998; Bayat, 2001] and bone growth have been conducted [Thomlinson, 2018] as well. While developments for angiographic imaging aim for the use as a diagnostic tool, the research on functional lung imaging mainly focuses on understanding pulmonary diseases such as asthma [Monfraix, 2005; Venegas, 2005; Bayat, 2006] and possible lung injuries from mechanical ventilation [Layachi, 2013; Bayat, 2013]. KES is also used for research on bone growth, musculoskeletal diseases and for investigating the uptake of pharmaceuticals [Panahifar, 2016], e.g., strontium-based drugs, which are used for the treatment of osteoporosis [Cooper, 2012]. Other studies demonstrated that KES is well suited for the determination of contrast agent concentrations [Elleaume, 2002] and allows for the calculation of the electron density with high precision [Torikoshi, 2003; Tsunoo, 2008].

Although the studies performed at synchrotron sources have shown very promising results, the application of KES in clinics is restricted due to the limited accessibility of synchrotron facilities. However, the development of compact synchrotron sources now provides a monochromatic beam in a laboratory setting and enables KES imaging in a pre-clinical setting.

While K-edge filtering at ICSs has been used for the characterization of the X-ray source and the measurement of the local X-ray spectrum [Williams, 2009; Golosio, 2012], the properties of ICSs' monochromatic X-ray spectra have been shown to be beneficial for biomedical imaging. The first experiments showing the benefit of monochromatic X-rays produced at a compact X-ray source were performed by Carroll et al. in 2003 [Carroll, 2003a]. In their study, they compared images from breast and finger phantoms

and a mouse pelvis, which were taken with conventional polychromatic spectra and with the monochromatic X-ray beam produced at an ICS at Vanderbilt University. The monochromatic images of the breast phantom thereby provided better image quality than the conventional images and allowed for the identification of more lesions in the tissue. The benefits of monochromatic X-rays produced by ICSs were confirmed in further studies by Yamada et al. [Yamada, 2009] and Kuroda et al. [Kuroda, 2011] at the LCS, focusing on refraction and phase-contrast imaging of bones. A major advantage of ICSs in comparison to conventional sources is that the spectrum can be tuned to the K-edge of the applied contrast agent. This provides a higher contrast in the acquired images [Yamada, 2009; Eggl, 2017]. Carroll showed the improvement in signal due to the higher X-ray absorption by the iodine contrast agent when tuning the X-ray beam directly to the K-edge and discussed its application for molecular and cellular imaging and therapy [Carroll, 2003b]. A study of KES using barium sulfate as a contrast agent was conducted by Kuroda et al. [Kuroda, 2014]. They demonstrated the feasibility of the imaging technique using a human head phantom at the LCS at AIST. Although the volume concentration ratio of the contrast agent was only 3 %, the contrast enhancement was seen to be 5 %. The experiments on KES imaging at the MuCLS are presented in Ch.s 5 and 6.

2.6.2 Basic principle

In KES imaging, images are acquired using X-ray energies directly below and above the K-edge of a contrast agent injected into the desired structures. The intensities of the X-ray beams at the lower energy, I_{low}, and at the higher energy, I_{high}, behind the imaged tissue can be described with

$$I_{\text{low}} = I_{0,\text{low}}\, e^{-[\mu_{T,\text{low}}(D-G)+\mu_{c,\text{low}}G]} \tag{2.23}$$

and

$$I_{\text{high}} = I_{0,\text{high}}\, e^{-[\mu_{T,\text{high}}(D-G)+\mu_{c,\text{high}}G]}, \tag{2.24}$$

where $\mu_{T,\text{low}}$ and $\mu_{T,\text{high}}$ are the mean attenuation coefficients of the surrounding tissue with thickness D at lower and higher energy and $\mu_{c,\text{low}}$ and $\mu_{c,\text{high}}$ are the attenuation coefficients of the contrast agent in the stained structure with thickness G, at lower and higher energy, respectively. To obtain an image only showing the contrasted structures, these radiographs are then subtracted logarithmically after dark current and flatfield correction.

$$\begin{aligned} \ln\frac{I_{\text{high}}}{I_{0,\text{high}}} - \ln\frac{I_{\text{low}}}{I_{0,\text{low}}} &= \ln\frac{I_{0,\text{high}}}{I_{0,\text{high}}} - \mu_{T,\text{high}}(D-G) - \mu_{c,\text{high}}G \\ &\quad - \ln\frac{I_{0,\text{low}}}{I_{0,\text{low}}} + \mu_{T,\text{low}}(D-G) + \mu_{c,\text{low}}G \\ &\approx (\mu_{c,\text{low}} - \mu_{c,\text{high}})G, \end{aligned} \tag{2.25}$$

as the attenuation coefficient of most tissues hardly changes over the range of a few keV ($\mu_{T,\text{low}}(D-G) - \mu_{T,\text{high}}(D-G) \approx 0$). The contrast in the calculated image

therefore only depends on the change in attenuation of the contrast agent, which has an absorption discontinuity in between the two energies.

2.7 Computed tomography

The technique of CT overcomes the limitations of conventional radiography where only a projection of a three-dimensional object onto a two-dimensional plane is measured and there is an inevitable loss of spatial information. In a CT scan, radiographic projections are taken over a wide range of projection angles. This makes it possible to fully reconstruct the three-dimensional structure of the object.

Thereby, a lower limit for the number of projection angles is needed to be able to perfectly reconstruct the volume. For a good reconstruction, the angular distance $\Delta\theta$ between two measurement points has to match the radial distance $\Delta q/q_{max}$ between them. Additionally, one has to measure at least over $180° = \pi$. So:

$$\Delta\theta = \frac{\pi}{N_{\text{proj}}} \approx \frac{\Delta q}{q_{\text{max}}} = \frac{2}{N_{\text{pix}}}, \tag{2.26}$$

with N_{pix} and N_{proj} being the size of the object measured in pixels and the number of projections, respectively. Therefore the relation between N_{pix} and N_{proj} is given by:

$$N_{\text{proj}} \approx \frac{\pi}{2} N_{\text{pix}}. \tag{2.27}$$

2.7.1 Filtered backprojection

In the following, a perfectly narrow monochromatic X-ray beam is assumed. Additionally, the beam is assumed to be parallel so that every X-ray and therefore every projection will be independent of all others [Als-Nielsen, 2011].

Now the reconstruction of a two-dimensional slice through an object $f(x, y)$ shall be explained. When taking a radiograph of a two-dimensional object, one gets a one-dimensional projection in the detector plane. The projection is measured as an intensity distribution which is directly dependent on the line integral of the absorption coefficient, with:

$$\ln\left[\frac{I_0}{I}\right] = \int \mu(x, y)\mathrm{d}y'. \tag{2.28}$$

The measured projection can be written as:

$$P_\theta(r) = \int f(x, y)\, \delta(x\cos(\theta) + y\sin(\theta) - r)\mathrm{d}x\mathrm{d}y, \tag{2.29}$$

where $f(x, y)$ is the 2D slice through the object which has to be reconstructed, θ is the angle of projection, and r is the distance from the origin (cf. Fig. 2.3). $P_\theta(r)$ is called Radon transform.

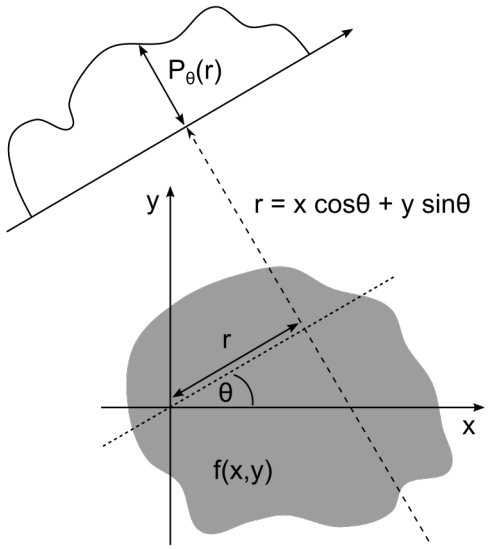

Figure 2.3: Projection of an object at an angle θ and a distance r from the origin.

To reconstruct the object out of the single projections from different angles, one uses Fourier analysis. Since it is impossible to gain 2D information from a 1D projection, the direct inversion of the Radon transform is not possible. Therefore, the Fourier Slice theorem is applied stating that the 1D Fourier transform (FT) of the projection $P_\theta(r)$ is an axial line through the 2D FT of the original function $f(x, y)$ at the same angle θ [Als-Nielsen, 2011] (cf. Fig. 2.4). This means that one can obtain the full 2D FT of $f(x, y)$ by combining the 1D FT of many angles. This again allows for the reconstruction of the object since a 2D function (the object in the plane) is uniquely determined if its full 2D Fourier transform is known.

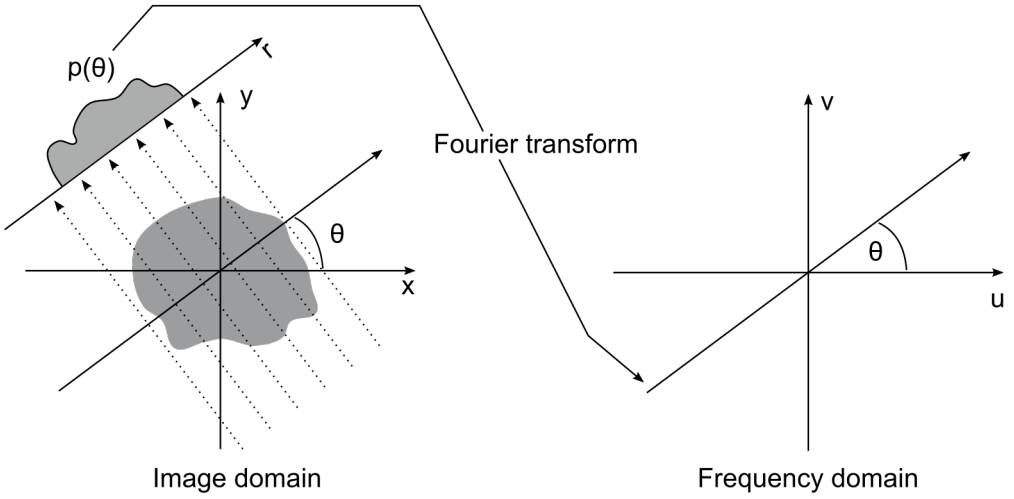

Figure 2.4: The 1D Fourier transform of a projection taken at an angle θ is an axial line through the 2D Fourier transform of the original function at the same angle.

In the frequency space, the projections are given by:

$$P_\theta(q) = \int_{-\infty}^{\infty} p_\theta(r)\, e^{+i2\pi qr} \mathrm{d}r = \int_{-\infty}^{\infty}\int_{-\infty}^{\infty} f(x,y)\, e^{+i2\pi q(x\cos(\theta)+y\sin(\theta))} \mathrm{d}x\mathrm{d}y, \tag{2.30}$$

with $r = x\cos(\theta) + y\sin(\theta)$ and $p_\theta(r)$ the line integrals of the object function $f(x,y)$. The initial function $f(x,y)$ can now be calculated by inverting the integral in Eq. 2.30. By doing this, i.e., doing a simple back projection from frequency to image domain, the measurement points will be smeared out. The reason for this is that the angular distance between the points increases with increasing distance from the origin (cf. Fig. 2.5). Therefore, the density of the measurement points is lower for high frequencies than for lower ones, which will lead to smearing of the points.

To simplify calculations, polar coordinates are introduced in the inverse FT with $u = q\cos(\theta)$ and $v = q\sin(\theta)$ with $\mathrm{d}u\mathrm{d}v = |q|\mathrm{d}q\mathrm{d}\theta$. Then:

$$\begin{aligned} f(x,y) &= \int_{-\infty}^{\infty}\int_{-\infty}^{\infty} P_\theta(u,v)\, e^{-i2\pi(xu+yv)}\, \mathrm{d}u\mathrm{d}v \\ &= \int_0^{\pi}\int_{-\infty}^{\infty} P_\theta(q\cos(\theta), q\sin(\theta))\, e^{-i2\pi q(x\cos(\theta)+y\sin(\theta))} |q|\, \mathrm{d}q\mathrm{d}\theta. \end{aligned} \tag{2.31}$$

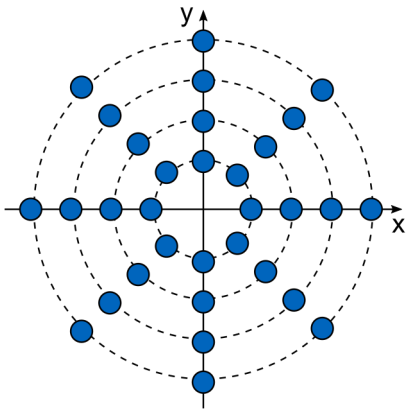

Figure 2.5: In the image domain, the angular distance between the points will increase with increasing distance from the origin. Having a smaller density of measurement points for high frequencies than for lower ones will lead to the smearing of the points.

With this procedure a filter $|q|$ is introduced, so that lower frequencies are weighted less than the higher ones (high pass filter). Summarizing

$$\int_{-\infty}^{\infty} P_\theta(q\cos(\theta), q\sin(\theta))\, e^{-i2\pi q((x\cos(\theta)+y\sin(\theta))} |q|\, \mathrm{d}q \tag{2.32}$$

to

$$P_\theta^F(x\cos(\theta), y\sin(\theta)), \tag{2.33}$$

leads to the filtered backprojection (FBP) of the object:

$$f(x,y) = \int_0^{\pi} P_\theta^F(x\cos(\theta), y\sin(\theta))\, \mathrm{d}\theta. \tag{2.34}$$

2.7.2 Statistical iterative reconstruction

While the FBP algorithm is computationally fast and relatively easy to implement, there are some limitations such as the required number of equally spaced projections and the ability to reduce noise. Therefore, with increasing computational capacities, iterative reconstruction algorithms that take advantage of statistical models and prior knowledge of the sample have emerged. Additionally, the statistical iterative reconstruction (SIR) approach can manage missing data (e.g., lost projections) as well as more complex geometries and is capable of reducing noise while requiring far fewer projections. However, the algorithm is more complex and needs more computational time and resources than FBP [Fessler, 2000].

The basic principle of iterative reconstruction consists of the following steps: First an estimate for the reconstructed image is generated, e.g., through FBP, and is forward projected. This estimate is then compared to the measured projections and updated based on the differences. This process is repeated until the estimate converges against the real measurement. Analytically the volume of the object to be constructed $\mathbf{f}$ is related to the experimentally measured set of projections $\mathbf{p}$ with the system matrix A via

$$A\mathbf{f} = \mathbf{p}. \tag{2.35}$$

Additionally, prior knowledge and a combination of forward and data model have to be included into the SIR. The forward model thereby generates a simulation of the expected experiment, while the data model calculates the log-likelihood minimization of the difference between measurement data and the forward projection. The algorithm then tries to find the minimum of the penalized log-likelihood function L, with

$$L = ||A\mathbf{f} - \mathbf{p}||_w^2, \tag{2.36}$$

with w being the statistical weights gained by the experimental statistics. However, the minimization problem is ill-conditioned since there are many possible solutions. Therefore, a regularizer $R(f)$ is added, which penalizes the reconstructed data such that data with high physical probability is preferred. This changes the optimization problem to

$$L = ||A\mathbf{f} - \mathbf{p}||_w^2 + \lambda R(f), \tag{2.37}$$

with λ being the Lagrange multiplier as the regularization strength. There are many different regularizer functions with the simplest being the quadratic regularizer. This one considers discrepancies between neighboring pixels and therefore discourages "roughness" in the images. Generally, the regularizer has the form

$$R(f) = \sum_i \sum_{j \epsilon N_i} \omega_{ij} \Phi(f_i - f_j), \tag{2.38}$$

where the index i runs over all image voxels and the index j over all the direct neighbors of voxel i, with N_i denoting the direct neighborhood of i. The weighting coefficients ω_{ij} vary depending on the distance of the neighboring pixels and are 1 for adjacent

neighbors, $1/\sqrt{2}$ for diagonal pixels and 0 otherwise. The potential function assigns a cost to $f_i - f_j$ and is ideally a convex function to keep the optimization stable [Fessler, 2000].

The CT data presented here was reconstructed with a SIR algorithm using the Huber regularizer, which is a modified version of the quadratic regularizer. The Huber regularization function is based on the Huber potential [Huber, 1964] being

$$\Phi = \begin{cases} \frac{(f_i - f_j)^2}{2\gamma^2} & \text{for } |f_i - f_j| \leqslant \gamma \\ \frac{|f_i - f_j| - \gamma/2}{\gamma} & \text{for } |f_i - f_j| > \gamma \end{cases}, \tag{2.39}$$

where γ is the regularization threshold [Huber, 1964; Hahn, 2014]. It specifies the transition from quadratic to linear behavior such that the regularization function preserves edge discontinuity [Zhang, 2013].

2.8 X-ray fluorescence

Two basic processes follow the absorption of an X-ray photon by an atom, X-ray fluorescence and the emission of an Auger electron. After the absorption of the X-ray and emission of an electron from an inner shell, an electron from an outer shell fills the remaining hole left by the photoelectron emission. The difference in the binding energy in this transition can be emitted as an X-ray photon (fluorescence) or transferred to another less bound electron, which is consecutively emitted into vacuum (Auger electron). The former process will be discussed in more detail in this chapter.

2.8.1 Basic principle

Any material or element can emit fluorescent light when illuminated by X-ray photons of the appropriate energy. Characteristic X-rays originate from the transition of an outer-shell electron to the hole left behind by an electron following photoelectric absorption of an X-ray photon. This process takes place in the order of 10 fs to 100 fs [Willmott, 2011]. The fluorescent X-rays have a narrow bandwidth since the energy difference between the two involved energy levels is well-defined. Thus, the X-rays are characteristic for the type of atom they originate from. The frequency ν of the K_α-line of an element can be calculated according to Moseley's law with

$$\nu = K(Z-1)^2, \tag{2.40}$$

with $K = 2.47 \times 10^{15}$ Hz and Z the atomic number of the atom. From Heisenberg's uncertainty principle $\Delta E \Delta t \propto \hbar$, with Δt being the lifetime of the state, it can be derived that the natural linewidth of fluorescent X-ray is in the order of 0.01 eV [Willmott, 2011]. However, not every electron transition between energy levels allows for the emission of a fluorescent X-ray. The emission is based on the electric dipole selection rules. Firstly, the change in angular orbital momentum Δl between the two

energy levels must be ± 1, since photons have an angular momentum of $1\hbar$. Secondly, the change of electron spin must be $\Delta s = 0$. Lastly, as the total angular momentum j is defined as the vector sum of angular and electron spin momenta $\mathbf{j} = \mathbf{l} + \mathbf{s}$, the change in total angular momentum is $\Delta j = 0, \pm 1$, while transitions from $j = 0$ to $j = 0$ are prohibited [Podorsak, 2006].

Nomenclature of fluorescent lines

The nomenclature for fluorescence lines follows the one for absorption lines with K, L etc., where, e.g., K describes the lower energy level the electron relaxes to. However, since several transmissions are possible (c.f. Fig. 2.6a), the nomenclature is more complex. For the characteristic K-line, the electron relaxes to electron state K or $1s$ ($n = 1$). The transition with the smallest energy difference will be labeled with α, the successive lines with β, γ, etc. So, a transition of an electron from electron state L ($n = 2$) to K will be the K_α transition, while the transition from state M to K will be the K_β transition. Transitions from one shell to another do not all have the same energy because of the fine structure in the shell levels. As shown in Fig. 2.6a, the lines are actually further split as the energy depends also on spin-orbit interactions, i.e., the orientation of the spin momentum vector with respect to the orbital momentum vector. These additional lines are labeled with natural numbers as suffices, e.g., α_1 and α_2 [Willmott, 2011].

Fluorescence yield

A vacancy in an electronic shell will be followed by either the emission of a fluorescent photon or an Auger electron. The branching ratio between these two processes is described by the fluorescence yield ω for a given atom and its atomic shell. The fluorescence yield of a specific shell is defined as the number of characteristic photons emitted per vacancy in the shell. It can also be seen as the probability of fluorescent photon emission as opposed to Auger electron emission [Pogorelsky, 2016]. Generally, the rate of spontaneous fluorescence is proportional to the third power of the energy difference between the upper and lower state. Therefore, the K emission lines are more probable and hence more intense than L emission lines. Additionally, fluorescence is stronger for heavier atoms due to the stronger nuclear charge and therefore larger energy differences between adjacent shells. In contrast, the probability of Auger electron emission $1 - \omega$ is inversely related to the energy difference between excited atom and atom after Auger emission. Therefore, the Auger emission will be high for atoms with low atomic numbers since the relatively small positive charge in the nucleus will lead to a small binding energy of the electron and promote the emission of Auger electrons. In Fig. 2.6b the fluorescence yields ω_K and ω_L are plotted as a function of the atomic number together with the probability for Auger electron emission, being $1 - \omega$. ω_K is zero at $Z = 0$ and increases in a sigmoid-shaped curve to almost 1 at very high Z. In contrast, w_L is zero for all elements with $Z < 20$ and only increases to about 0.5 for elements with $Z = 100$. This trend continues for the fluorescence yield of the M-line

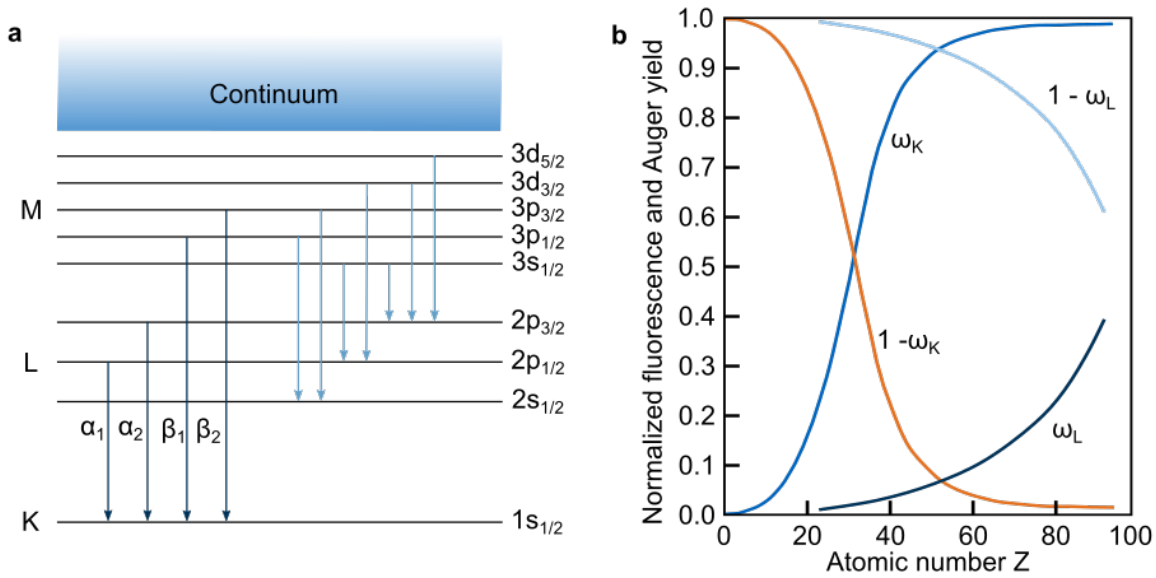

Figure 2.6: **a** Possible X-ray fluorescence emissions after photoelectric absorption: K-lines are shown in dark blue, where the α-lines display transmissions from L to K shell, and β from M to K shell. The light blue lines show the possible transitions for L-line emissions; **b** Fluorescence yields ω and probabilities for Auger electron emission for K and L shells. ω_K is zero at $Z = 0$ and increases in a sigmoid-shaped curve to almost unity at very high Z. In contrast, w_L is zero for all elements with $Z < 20$ and only increases to about 0.5 for elements with $Z = 100$. Since the probability for Auger electron emission is $1 - \omega$, the curves of the Auger electron emission are inverted to the fluorescence yields. Images partially adapted from [Willmott, 2011].

(not shown in graph) which is only greater than zero for high Z elements of $Z > 60$ and only increases slowly. This suggests that the fluorescence emission from the M shell is negligible in comparison to the K- and L-lines [Willmott, 2011; Pogorelsky, 2016].

2.8.2 Quantitative analysis

When a sample is irradiated with X-rays of appropriate energy, fluorescent X-rays are emitted. Thereby the incident X-rays will hit the sample under angle α while the fluorescent X-rays hit the detector under angle β (cf. Fig. 2.7a). When calculating the fluorescence emitted by a layer with thickness dx in a depth x in the sample, it is important to also consider the attenuation of the primary radiation on its way from the surface of the sample to the layer as well as the attenuation of the fluorescent light on its way to the surface. The probability that a primary photon reaches the layer in depth x is $\exp(-\mu_T(E)x/\sin(\alpha))$. With a probability of $\omega\frac{\Delta\Omega}{4\pi}\mu_i(E)/\sin(\alpha)\,\mathrm{d}x$ it is absorbed in layer dx and produces a fluorescent photon in solid angle $\Delta\Omega$. ω hereby describes the probability for fluorescent emission (instead of Auger emission). This fluorescent photon has a probability of $\exp(-\mu_T(E_f)/\sin(\beta)x)$ of being detected in the

detector [Beckhoff, 2006]. This results in

$$\frac{I_f}{I_0} = \omega \frac{\Delta\Omega}{4\pi} \frac{\mu_i(E)}{\sin(\alpha)} \int \exp\left[-\left(\frac{\mu_T(E)}{\sin(\alpha)} + \frac{\mu_T(E_f)}{\sin(\beta)} \right) x \right] \mathrm{d}x, \tag{2.41}$$

where μ_T and μ_i are the total absorption coefficient and the absorption coefficient of the element emitting the fluorescent light depending on the energy of the incident photons E and the fluorescent photons E_f and $\mu_T = \mu_i + \mu_b$ with μ_b being the background of the sample. When integrating over the whole sample thickness d, this results in

$$\frac{I_f}{I_0} = \omega \frac{\Delta\Omega}{4\pi} \frac{\mu_i(E)}{\sin(\alpha)} \frac{1 - \exp\left[-(\frac{\mu_T(E)}{\sin(\alpha)} + \frac{\mu_T(E_f)}{\sin(\beta)}) d \right]}{\frac{\mu_T(E)}{\sin(\alpha)} + \frac{\mu_T(E_f)}{\sin(\beta)}}. \tag{2.42}$$

In this calculation, it is assumed that the radiation is emitted through the same surface as it enters the sample from (cf. Fig. 2.7a) [Jaklevic, 1977; Hippert, 2006; Bunker, 2010]. A setup where the incident radiation enters and the fluorescent radiation exits on opposite sides of the sample is shown in Fig. 2.7b. When the radiation passes through the sample under angle γ and the fluorescent light hits the detector on the backside of the sample under an angle δ, Eq. 2.41 changes to

$$\frac{I_f}{I_0} = \omega \frac{\Delta\Omega}{4\pi} \mu_i(E) \int e^{-\mu_T(E)x} e^{-\mu_T(E_f)x'} \mathrm{d}x, \tag{2.43}$$

where x' is the path on which the fluorescent X-ray leaves the sample with $x' = a(d' - x)$, $a = \frac{\sin(\gamma)}{\sin(\delta)}$ and $d' = d/\sin(\gamma)$. By integrating Eq. 2.43 [Als-Nielsen, 2011], one obtains

$$\frac{I_f}{I_0} = \epsilon \frac{\Delta\Omega}{4\pi} \frac{\mu_i(E)}{\mu_T(E) + \mu_T(E_f)} e^{-a\mu_T(E_f)d'} \left[1 - e^{-(\mu_T(E) - a\mu_T(E_f))d'} \right]. \tag{2.44}$$

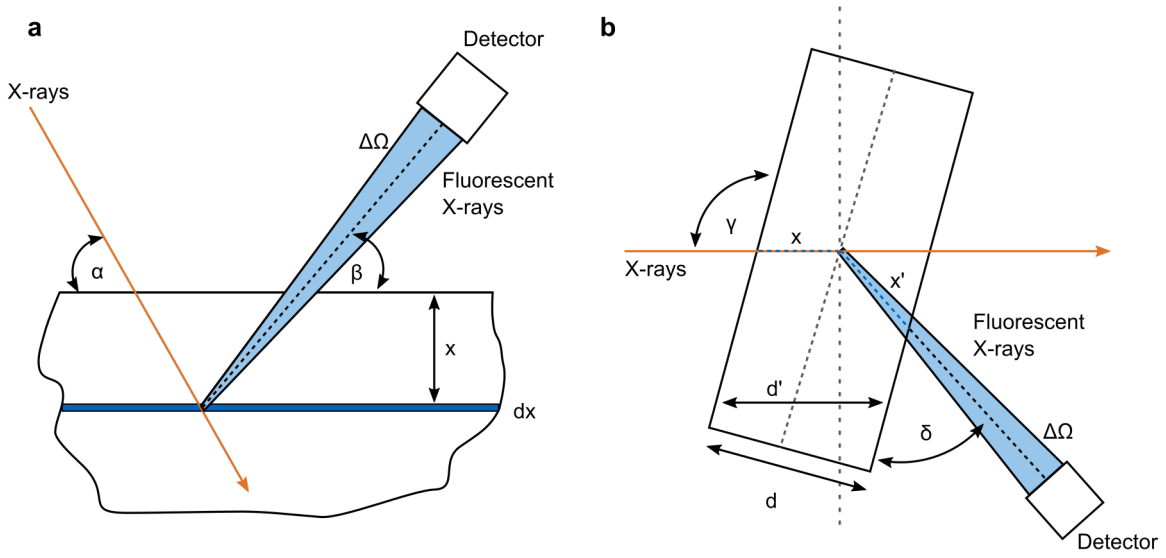

Figure 2.7: Setups for XRF measurements: **a** Setup where incident and fluorescent radiation enter and exit the sample from the same side under angles α and β, respectively. Adapted from [Beckhoff, 2006]; **b** Setup where the incident and fluorescent radiations enter the sample under angle γ and exit the sample under angle δ on opposite sides of the sample.

3 Generation of X-rays

3.1 Figures of merit

When deciding on the use of the X-ray source, several characteristics of the X-ray beam are important, such as the photon energy, flux, brilliance, coherence and emittance. For some applications a high X-ray flux is desired, such as high-speed dynamic imaging, while other applications, e.g., phase contrast imaging, require the coherence of the X-ray beam. Different types of X-ray sources can be distinguished due to their characteristics, some of which will be described in more detail in the following chapter. If not stated elsewise, this chapter is based on chapters 1 and 2 of "Elements of Modern X-ray Physics" by Jens Als-Nielsen and Des McMorrow [Als-Nielsen, 2011].

Brilliance

In order to compare the beams of different X-ray sources, one must consider several aspects of the source that determine the quality of the produced X-ray beam. The first aspect is the spectral distribution of the X-rays. As X-ray sources can produce very different spectra, it is important to determine the range of photon energies contributing to the measured intensity. Usually, one defines the photon energy range $\Delta E/E$ as 0.1 % of the bandwidth (BW). Next, the number of photons emitted per second Φ and the size of the source area A are considered. Finally, there is the collimation of the beam $\Delta\Omega$, meaning how much the beam diverges as it propagates. These aspects can be combined into a single quantity, the brilliance. The brilliance can be defined by

$$\text{Brilliance} = \frac{\text{Photons/second}}{(\text{mrad})^2(\text{source area in mm}^2)(0.1\%\ \text{BW})} = \frac{\Phi}{\Delta\Omega\, A\, \Delta E/E}. \tag{3.1}$$

In X-ray imaging, a highly brilliant beam is desired, as this means that there is a high photon flux allowing measurements with good photon statistics and short measurement times. Standard laboratory X-ray sources provide a broad spectrum of X-rays and therefore have a relatively low brilliance. Synchrotron sources, on the other hand, have a much smaller bandwidth and significantly higher flux than conventional sources. Their brilliance is in the order of ten magnitudes higher than the one of standard sources. Fig. 3.1 shows how the brilliance of X-ray sources have increased over the past 100 years. The compact synchrotron source at the MuCLS, used for this work, provides a brilliance in between that of a rotating anode X-ray tube and a first generation synchrotron.

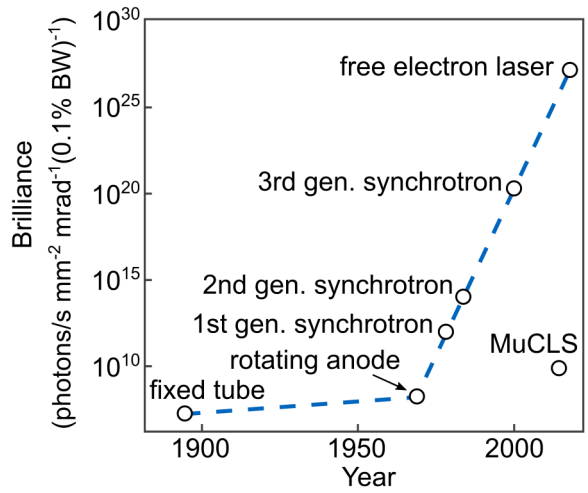

Figure 3.1: Brilliance of different types of X-ray sources. In general, the brilliance of X-ray sources has increased with development over time. The compact synchrotron source at the MuCLS provides a brilliance in between that of a rotating anode source and a first generation synchrotron source.

Emittance

The emittance of an X-ray source is defined as the product of the source size A and the divergence $\Delta\Omega$. Therefore, the emittance has to be small to obtain a high brilliance of the X-ray source. For electron storage ring-based X-ray sources, such as synchrotrons and some compact synchrotron sources, the emittance of the X-ray source is determined by the convolution of the emittance of the electron beam in the storage ring with the emittance of the photon beam. In general, the emittance is limited by Heisenberg's uncertainty relation. Beyond the limit, any reduction in source size will lead to an increase in source divergence, and vice versa.

Coherence

While the brilliance gives a measure for the photon energy of an X-ray source, its source size, the beam divergence and the energy bandwidth, it does not give information about the quality of the beam concerning the coherence. For some applications, however, the coherence of the X-ray beam is crucial. The coherence is used to describe the phase relations of the X-ray waves, both temporally (longitudinal coherence) and spatially (transverse coherence).

While an ideal X-ray beam consists of planar X-ray waves with a single wavelength λ, a realistic X-ray beam will not be perfectly monochromatic and will not propagate in a perfectly well-defined direction. The longitudinal coherence length L_L depicts the distance

$$L_L = \frac{1}{2}\frac{\lambda^2}{\Delta\lambda}, \tag{3.2}$$

which is needed for two waves with slightly different wavelengths λ and $\lambda - \Delta\lambda$ to be completely out of phase.

The transverse coherence length takes into account that there is an angular difference $\Delta\Theta$ in propagation direction of two waves in the X-ray beam. This difference arises from the waves being emitted at two different points of the X-ray source with size D. At a distance R far away from the source ($R \gg D$), this will be seen as a difference in propagation direction $\Delta\Theta$. The transverse coherence length L_T describes the distance perpendicular to the propagation direction when the two waves are completely out of phase:

$$L_T = \frac{\lambda}{2}\frac{R}{D}. \tag{3.3}$$

Note that the transverse coherence length not only depends on the source size but also on the distance from the source.

3.2 Target-based X-ray sources

The first standard X-ray tube was developed by W. D. Coolidge in 1912. The principle of the standard X-ray tube is that electrons interact with a specific anode material. The electrons are emitted from a heating filament and accelerated with a high voltage in vacuum towards a water-cooled metal anode, as shown in Fig. 3.2a. The intensity of the X-ray beam is determined by the high voltage between filament and anode and by the current flowing through the filament. It is limited only by the cooling efficiency as a large part of the electron energy is converted into heat. It is therefore desired to have an anode material with a high melting temperature and good thermal conductivity such as tungsten, copper or molybdenum. The maximum power a cooled metal anode can withstand is around 1 kW [Als-Nielsen, 2011]. This limits the brilliance of these sources to the order of 10^6 photons $\mathrm{s}^{-1}\,\mathrm{mm}^{-2}\,\mathrm{mrad}^{-2}\,(0.1\%\,\mathrm{BW})^{-1}$. To dissipate the heat load over the anode material, rotating anode sources were developed (cf. Fig. 3.2c). Due to the periodic cooling of the non-illuminated part of the anode, the maximum power for these sources is a multiple of those with a fixed metal anode source. Another type of target-based X-ray source is the so-called liquid-metal jet, presented in Fig. 3.2c. In a liquid metal jet source, the target is made of a stream of liquid metal alloy which is shot through a nozzle with high pressure. Since the metal alloy, which is usually a gallium or indium alloy, is liquid at room temperature, melting of the anode material is not an issue of this type of source. Moreover, the anode material is continuously replaced, allowing for higher electron beam power than for a source with a solid anode material [Hemberg, 2003; Excillum AB, 2020].

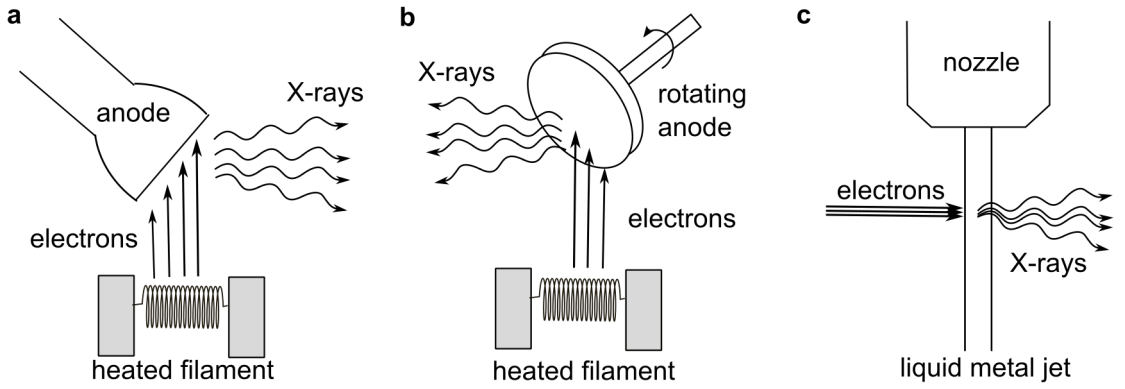

Figure 3.2: Schematics of target-based X-ray sources. **a** The standard X-ray tube is made up of a heating filament emitting electrons that are accelerated by high voltage towards the cooled anode. The electrons interact with the anode material leading to the emission of X-rays; **b** The rotating anode tube has a similar setup as the standard X-ray tube, yet the anode rotates during the illumination with electrons. This distributes the heat-load more homogeneously on the anode material and enables a higher power; **c** In a liquid metal jet source, a liquid metal alloy is shot through a nozzle with high pressure. An electron beam is focused onto the metal stream, leading to the emission of X-rays. Since the anode material is continuously replaced, the electron beam power can be higher than with a solid anode material.

When the electrons hit the metal anode, two interaction processes take place that produce the X-ray spectrum shown in Fig. 3.3a. The first process is the deceleration of the electrons in the anode material causing the decelerating electrons to emit the so-called bremsstrahlung. This gives a continuous spectrum with a maximum energy corresponding to the high voltage applied to the tube. In addition to the deceleration, the electrons collide with the atoms of the anode material. In this collision, the incident electron can remove an electron from one of the inner shells of the atom. The vacancy in the inner shell is filled with an electron from an outer shell, releasing a fluorescent X-ray with an energy corresponding to the difference of the two atomic shells (cf. Fig. 3.3b). These characteristic X-rays produce a sharp line spectrum, which is superimposed onto the continuous spectrum. Often two characteristic X-ray lines can be seen. These are the K_α- and K_β-lines, corresponding to the transition from the L to the K and the M to the K shell, respectively. Although the K-lines are usually several orders of magnitude more intense than the bremsstrahlung spectrum, the lines are dependent on the anode material and cannot be tuned in energy to fit the experimental purpose.

3.3 Synchrotron sources

Synchrotron storage rings are sources of very powerful X-radiation, in which electrons emit radiation similar to the bremsstrahlung produced in X-ray tubes by being forced on a curved trajectory. Since the particles are traveling at relativistic speeds, the

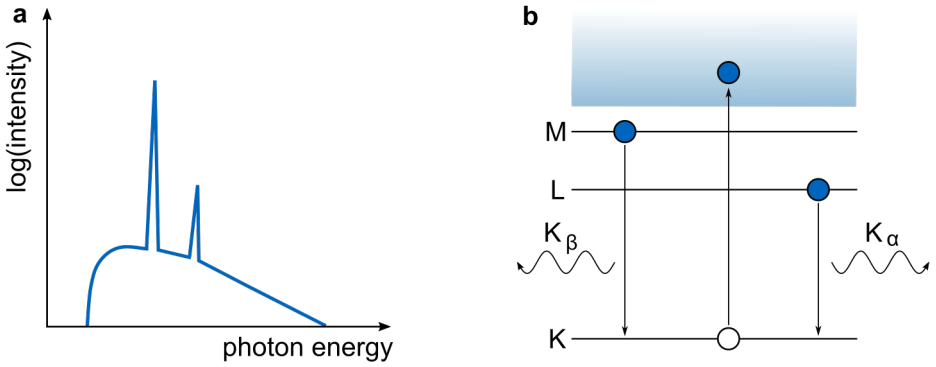

Figure 3.3: **a** The spectrum of a standard X-ray tube is made up of a continuous bremsstrahlung spectrum superimposed with characteristic fluorescent lines; **b** Schematic atomic energy level diagram: The transition from the L to the K shell produces the K_α-line, the one from M to K the K_β-line.

radiation is referred to as synchrotron radiation, which is generally highly collimated, has a high intensity and an energy in the X-ray regime. This chapter will give a brief overview of the production of X-rays at synchrotrons, more detailed calculations can be found in [Als-Nielsen, 2011; Willmott, 2011].

At a synchrotron facility, electrons are accelerated to relativistic energies and then orbit in an evacuated storage ring. In the storage ring, the electrons are forced onto their trajectory by so-called bending magnets, resulting in the emission of a first type of synchrotron radiation. The radius of the storage ring thereby limits the maximum energy of the electrons stored. The synchrotron radiation produced by a bending magnet is polychromatic and depends on the bending radius and the electrons' energy. In order to produce X-ray photons with energies in the keV range, storage ring electrons usually have energies of about 1 to 8 GeV. As the electrons travel with relativistic energies, the emitted radiation does not have a dipole distribution but is emitted in a narrow cone along the trajectory of the electrons. The natural opening angle Θ of this cone is dependent on the Lorentz factor γ with $\Theta \sim 1/\gamma$ and

$$\gamma = \frac{E}{m_e c^2} = 1957 E(\mathrm{GeV}), \tag{3.4}$$

where E is the electron energy and $m_e c^2$ is the electron rest energy. The radiation travelling towards the observer will additionally be Doppler shifted by an additional factor of 2γ [Willmott, 2011].

In third generation synchrotron sources, there are straight sections in between the curved arcs of the storage ring, in which insertion devices are installed. Insertion devices are periodic magnet structures producing an alternating magnetic field that force the electrons onto a sinusoidal trajectory perpendicular to their orbit. Two types of insertion devices will be discussed in the following, the wiggler and the undulator.

The trajectory produced by a wiggler can be viewed as a series of circular arcs, turning the electrons orbit successively to the left and the right. This leads to an enhancement

in the intensity of the emitted radiation by a factor of $2N$ with N being the number of periods. The spectrum emitted from a wiggler is incoherent and is the same as that from a bending magnet with a comparable magnetic field strength.

An insertion device can also be constructed such that the radiation emitted by an electron at one oscillation is in phase with the radiation from the following oscillation. This leads to a summation of the amplitudes of the radiation waves and a significant increase in intensity of the emitted radiation. An undulator is an insertion device that works in this way [Als-Nielsen, 2011].

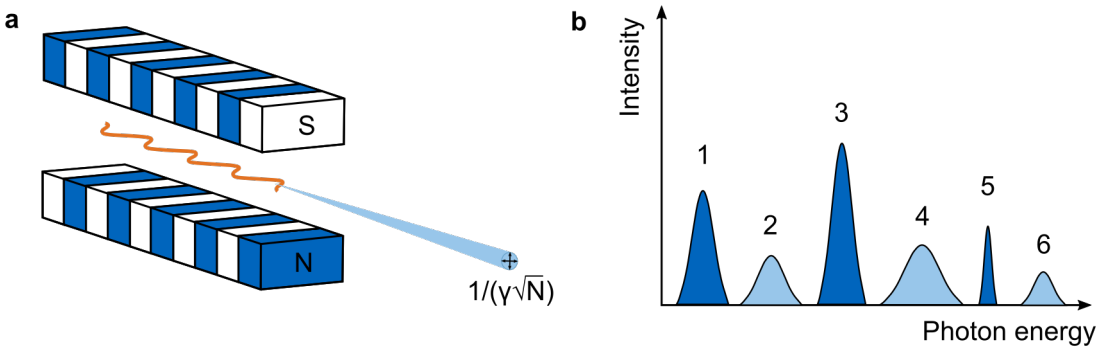

Figure 3.4: X-radiation produced by an undulator. **a** The radiation produced in the undulator is emitted into a cone with a divergence of $1/(\gamma\sqrt{N})$; **b** Several harmonics of radiation are produced in an undulator. The fundamental wavelength ($n = 1$) dominates while higher harmonics vary in intensity. Images adapted from [Als-Nielsen, 2011].

The two insertion devices can be distinguished via the dimensionless parameter K which describes the maximum angular deviation Φ_{max} of the electron oscillation in the insertion device. K can also be defined dependent on the maximum magnetic field strength B_0 with

$$K = \Phi_{\max}\gamma = 0.934\lambda_{in}[\mathrm{cm}]B_0[\mathrm{T}], \tag{3.5}$$

where λ_{in} is the period of oscillation in the insertion device. For a wiggler K is usually $10 - 20$ and about unity in an undulator [Willmott, 2011]. While the oscillation of electrons in a wiggler is so strong that the emitted radiation cones do not overlap, the radiation in an undulator interferes constructively so that the intensity of the radiation amplifies. The fundamental wavelength of the produced radiation is thereby dependent on the undulator period λ_u. When observing the radiation cone at an angle Θ from the axis of the undulator, the wavelength of the radiation is

$$\lambda = \frac{\lambda_u}{2\gamma^2 n}\left(1 + \frac{K^2}{2} + \Theta^2\gamma^2\right), \; n = 1, 2, 3, ... \tag{3.6}$$

For on-axis observation and small values of K, the spectrum is dominated by $n = 1$ and higher harmonics are suppressed [Willmott, 2011]. The wavelength may also be tuned by changing the undulator period λ_u. The angular divergence of the undulator radiation beam is $1/(\sqrt{N}\gamma)$ in both horizontal and vertical direction (cf. Fig.3.4). For a

wiggler the beam divergence varies depending on the direction; in horizontal direction it is K/γ, in vertical direction $1/\gamma$ as it is the case for a bending magnet [Als-Nielsen, 2011]. The produced X-rays at synchrotrons are guided through so-called beamlines to the experimental stations. If necessary, the beam is adjusted by a monochromator, a filter or other optical instrument to fit the experimental purpose.

Free electron laser

Since the electrons travel through the undulator as an electron gas or bunch, there is no positional order between the single electrons. This issue can be overcome by grouping the electrons in micro-bunches with distances equal to an X-ray wavelength, thus spatially organizing them and assuring that the radiation from one micro-bunch is in phase with the radiation from all other micro-bunches. This principle is used in a free-electron laser (FEL), which is in principle a long undulator. In an FEL, relativistic electrons move through an undulator and are influenced not only by the magnetic field of the undulator but also by the transverse electric field of the emitted radiation. This causes some electrons to gain and others to lose energy, thus changing the electron density modulation in the electron bunch. The electrons are separated into micro bunches with a distance equal to the wavelength of the emitted radiation. This effect enhances itself as the electrons move downstream through the undulator. This principle is called self amplified spontaneous emission (SASE). The emitted radiation of an FEL is in-phase and therefore adds up coherently. The produced X-rays thereby have a brilliance which is several magnitudes higher than 3rd generation synchrotrons (cf. Fig. 3.1). The energy of the beam can be tuned by adjusting the magnetic field strength of the undulator or the electron energy.

3.4 Compact synchrotron X-ray sources

While synchrotrons provide highly brilliant monochromatic X-rays, they rely on electron storage rings of several hundred meters in circumference and are expensive in terms of installation as well as operation and maintenance. In contrast, the use of conventional X-ray tubes in laboratories and hospitals is comparably cheap, but they feature low brilliance and polychromatic X-ray spectra. Over the past decades, compact synchrotron sources have been developed as an alternative means to serve the need for high flux monochromatic X-ray beams in a laboratory environment. These sources provide brilliance in between those of a large-scale synchrotron and a conventional X-ray source. Compared to the former, a main advantage of compact synchrotron sources are the reduced spatial and financial requirements for acquisition, operation and maintenance [Huang, 1998; Jacquet, 2014; Eggl, 2016]. These lower investment costs enable the transfer of certain techniques that have been limited to synchrotrons so far, like KES-imaging, into a laboratory or pre-clinical environment.

This chapter gives an introduction to the X-ray production and X-ray flux at an inverse

Compton X-ray source. The first commercially available inverse Compton source is installed at the Munich Compact Light Source and will be presented Ch. 3.4.1. Currently many projects to build inverse Compton sources are ongoing and will be described in more detail in Ch. 3.4.2.

There are two different, but fully equivalent, explanations of the X-ray production at a compact synchrotron X-ray source. The operation can be understood as a collision of two particles resulting in inverse Compton scattering, or as the electron entering an electromagnetic field of a laser which provides an undulator force. Both views will be explained in the following.

Particle picture: Inverse Compton scattering

In the particle view, the X-ray production at a compact synchrotron source can be explained with the process of inverse Compton scattering. A relativistic electron collides with a photon of a high intensity laser pulse, changing the momenta of both electron and laser photon. The photon is backscattered and emerges with a much shorter wavelength (see Fig. 3.5). The resulting energy E_x of the laser photon can be described by [Loewen, 2003]:

$$E_x = \frac{(1 - \beta \cos\theta_i) \cdot E_L}{1 - \beta \cos\theta_f + (E_L/E_e)(1 - \cos(\theta_f - \theta_i))}, \tag{3.7}$$

with E_e being the electron energy, E_L the initial energy of the laser photon, $\beta = v/c$, v being the velocity of the electron and c the speed of light in vacuum, and θ_i and θ_f being the initial and final angle between the trajectories of the electron and the laser. If one only considers head-on collision ($\theta_i = \pi$) [Loewen, 2003; Schleede, 2013], Eq. 3.7 simplifies to:

$$E_x = \frac{E_e(1 + \beta)E_L}{(1 - \beta \cos\theta_f)E_e + (1 + \cos\theta_f)E_L}. \tag{3.8}$$

Further considering on-axis observation with $\theta_f = 0$ and that $\beta \approx 1$ so that $\gamma = 1/\sqrt{1 - \beta^2} \gg 1$ and assuming that $E_L \ll m_0 c^2$, Eq. 3.8 simplifies to: [Loewen, 2003; Jacquet, 2014]

$$E_x \approx \frac{E_e(1 + \beta)^2 E_L}{E_e/\gamma^2} \approx 4\gamma^2 E_L. \tag{3.9}$$

The X-ray energy can be tuned by adjusting the energy of the electrons since the laser energy is usually fixed.

Wave picture: Laser undulator

In the wave picture, the counter propagating laser photons act as a localized electromagnetic field on the electrons, analogously to a permanent magnetic undulator [Schleede, 2013]. For an undulator, the basic parameters are the undulator period λ_u and the Lorentz factor γ, which relates to the electron energy. The undulator period

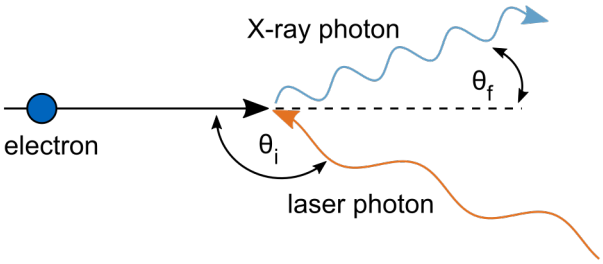

Figure 3.5: Principle of inverse Compton scattering: A laser photon is scattered at a relativistic electron at an angle of θ_i. The scattered photon has a higher energy than the incident photon and propagates under the angle θ_f. The angles are exaggerated for better understanding.

λ_u corresponds to half of the laser wavelength, e.g., about 0.5 µm at the MuCLS. This wavelength is about 10^4 times smaller than at a synchrotron facility ($\lambda_u \sim$ cm), allowing for the electron energy to be reduced by a factor of 100 and thus also for the size of the electron storage ring to be scaled down to a few meters in circumference. This enables the source to fit into a standard laboratory [Eggl, 2016].

The fundamental wavelength λ_u of an undulator can be derived by observing an electron traveling through the undulator and emitting radiation. Considering a point A at $t = 0$ and a point B at $t = T'$, the radiation emitted at point B has to constructively interfere with the radiation emitted at A (having traveled the distance cT' while the electron travels from A to B) [Willmott, 2011]. The difference in the two distances is $cT' - \lambda_u$ so that

$$n\lambda_n = cT' - \lambda_u. \tag{3.10}$$

For small oscillations of the electron beam path, T' is marginally greater than λ_u/v. As the electron velocity v is close to c, this small deviation has a high impact on the condition for constructive interference and the oscillatory path has to be considered. The path $S = vT'$ can be determined according to [Willmott, 2011] to be

$$S = \lambda_u \left[1 + \left(\frac{K}{2\gamma}\right)^2\right]. \tag{3.11}$$

The condition for constructive interference from Eq. 3.10 is therefore

$$n\lambda_n = \frac{\lambda_u}{\beta}\left[1 + \left(\frac{K}{2\gamma}\right)^2\right] - \lambda_u, \tag{3.12}$$

with $K = \frac{eB_0\lambda_u}{2\pi mc}$, where B_0 is the magnetic field of the magnets, e and m are the electron charge and mass, and c is the speed of light. With $\beta \approx 1 - 1/2\gamma^2$ and recognizing that $\gamma^2 \gg 1$, after further calculations Eq. 3.12 reduces to:

$$n\lambda_n = \frac{\lambda_u}{2\gamma^2}\left(1 + \frac{K}{2}\right). \tag{3.13}$$

The resulting on-axis wavelength will therefore be in the order of $\lambda_u/2\gamma^2$. Considering that relativistic effects cancel out and with $\lambda_u = \lambda_L/2$ and $\lambda = hc/E$, the energy of the X-ray photons E_X can be linked to the energy of the laser photons via [Schleede, 2013]:

$$E_X \approx 4\gamma^2 E_L. \tag{3.14}$$

This is the same relation as found above in Eq. 3.8.

X-ray flux

The X-ray flux, thus the number of emitted X-rays per second, for a head-on inverse Compton scattering of electron bunches and laser pulses can be calculated as

$$F_{\text{tot}} = \frac{\sigma_T N_L N_e f_{\text{rep}}}{2\pi(\sigma_e^2 + \sigma_l^2)}, \tag{3.15}$$

where σ_T is the Thomson cross-section, N_e the number of electrons per bunch, N_L the number of photons per laser pulse, f_{rep} the repetition frequency of electron-laser interactions, σ_e the transverse size of the electron bunch and σ_L the size of the laser pulse at the interaction point [Jacquet, 2014; Deitrick, 2018]. The X-ray flux can be increased by decreasing the source size, increasing the number of photons and electrons and achieving a high repetition frequency. Thereby, the repetition frequency f_{rep} mainly depends on the machine design.

However, the angular aperture of the source will limit the number of scattered photons available for the X-ray beam. The photon flux F_{mr} selected by an aperture with a half opening angle of θ_{mr} in the range of milliradians can be approximated as:

$$F_{\text{mr}} = F_{\text{tot}}\gamma^2\theta_{mr}^2\sigma(\omega_{\text{mr}}), \tag{3.16}$$

with $\omega_{\text{mr}} = 1 - (\gamma\theta_{\text{mr}})^2$ [Jacquet, 2015].

Additionally, the angular intensity distribution of the produced X-rays can be derived from the Klein-Nishina formula describing the cross-section for Compton scattering. The cross-section for inverse Compton scattering is

$$\frac{\mathrm{d}\sigma}{\sin\theta_f \mathrm{d}\theta_f} = \pi r_e^2 R^2 \frac{1-\beta^2}{(1-\beta\cos\theta_f)^2}\left[R + \frac{1}{R} - 1 + \cos^2\theta'\right], \tag{3.17}$$

with

$$R = \frac{1}{1 + (1+\beta)\gamma\frac{E_L}{mc^2}(1+\cos\theta')} \text{ and } \cos\theta' = \frac{\cos\theta_f - \beta}{1-\beta\cos\theta_f}, \tag{3.18}$$

where r_0 is the Thomson scattering length, m the electron mass, θ_f is the angle between the trajectories of electron and X-ray photon and $\gamma = \sqrt{1-\beta^2}^{-1}$ with $\beta = v/c$ [Stepanek, 1998].

3.4.1 The Munich Compact Light Source

The Munich Compact Light Source consists of a compact synchrotron source, namely the Compact Light Source (CLS), and an in-house developed dedicated imaging beamline with two endstations (cf. Fig. 3.6a). The CLS was developed and manufactured by Lyncean Technologies Inc., USA. It was the first commercially sold device and installed at the Technical University of Munich (TUM) in April 2015 [Eggl, 2016; Achterhold, 2013]. The source is based on inverse Compton scattering, thereby providing a tunable, quasi-monochromatic X-ray beam [Achterhold, 2013; Eggl, 2016].

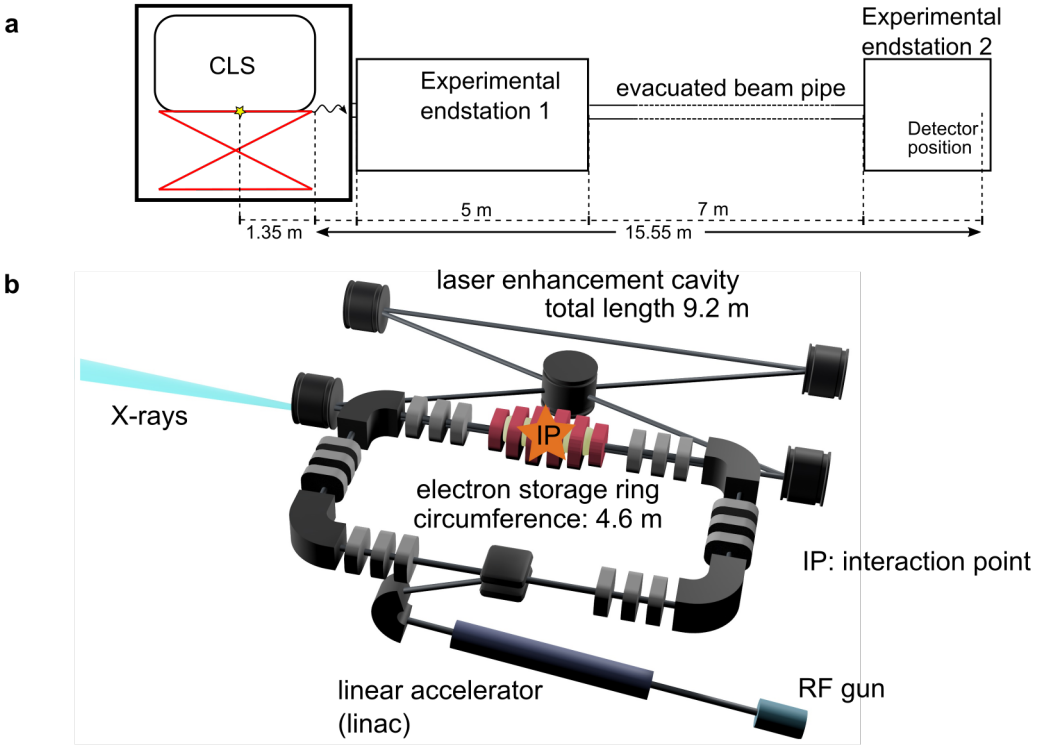

Figure 3.6: Schematic setup of the inverse Compton source at MuCLS. **a** The MuCLS is made up of a CLS, developed and manufactured by Lyncean Technologies Inc., and two experimental endstations, built at TUM; **b** The CLS is made up of a linac accelerating the electrons that are then stored in the electron storage ring (circumference 4.6 m) to relativistic energies. The laser photons are stored and enhanced in the laser cavity (total length 9.2 m) and then focused into the interaction point (IP) where they interact with the electrons in the process of inverse Compton scattering. The produced X-rays exit the source through one of the laser cavity mirrors and are guided to the experiment through an evacuated beam pipe.

A schematic setup of the CLS can be seen in Fig. 3.6b. The electrons are produced by a photo-cathode radio-frequency (RF) gun. They are accelerated in a linear accelerator (linac) to relativistic energies between 29 MeV and 45 MeV and subsequently injected into the electron storage ring with a circumference of 4.6 m. In the storage ring the electron bunch cycles with a repetition rate of about 65 MHz and is replaced with a rate of 25 Hz to ensure high beam quality. The infrared laser (Nd:YAG) has a wavelength

of 1064 nm (corresponding to an energy of 1.17 eV). It is pre-amplified to about 30 W before being injected into the bow-tie shaped laser enhancement cavity (total length: 9.2 m). The high finesse optical resonator stores and enhances the infrared laser pulse, reaching a stored laser power of up to 350 kW. In one point of one of the straight arms of the electron storage ring, which is also used as a part of the laser enhancement cavity, the counter-propagating electron bunches and laser pulses interact as described in the previous chapter. Their revolution frequencies (65 MHz) are matched so that electrons and laser photons collide upon each revolution at the interaction point (IP). Before the interaction, the two are tightly focused to ensure a small source spot size. Finally, the produced X-rays exit the source through a transmissive window in one of the laser cavity mirrors and are guided to the experimental endstations through an evacuated beam pipe. The X-ray exit aperture of the source limits the opening angle X-ray beam to ± 2 mrad. Fig. 3.7a shows the X-ray energy's dependence on the scattering angle θ_f exemplary for an X-ray energy of 33 keV. According to Eq. 3.8, the energy drops by about 2 % with an opening half-angle of 2 mrad. In practice however, the electron beam divergence leads to a mixture of different opening angles so that there is an even smaller energy drop.

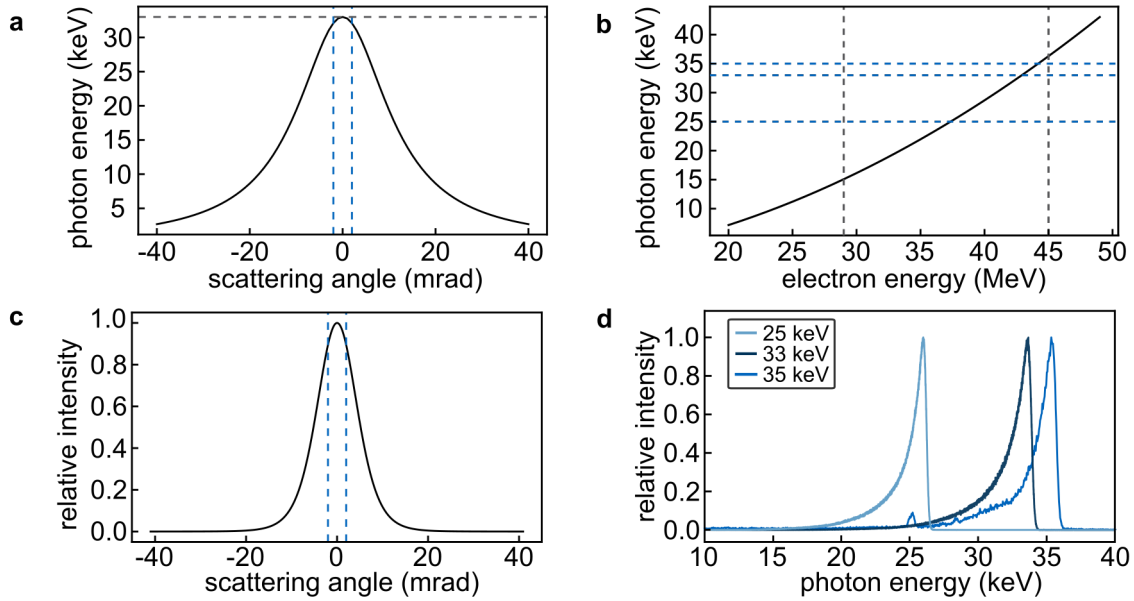

Figure 3.7: X-ray beam parameters at the MuCLS. **a** The X-ray energy is dependent on the scattering angle θ_f. The dashed lines show the 2 mrad half angle chosen at the MuCLS, for which the X-ray energy only slightly decreases; **b** The X-ray energy is dependent on the electron energy. The electron energy can be tuned between 29 MeV and 45 MeV, producing an X-ray beam with an energy between 15 keV and 35 keV. The X-ray energies used for this thesis are marked with horizontal dashed lines; **c** The beam intensity is also dependent on the scattering angle (cf. Eq. 3.17). The dashed lines show the chosen half angle at the MuCLS; **d** shows the X-ray spectra used for this thesis with peak energies at 25 keV, 33 keV and 35 keV.

By changing the electron energy, the X-ray energy at the MuCLS is tunable between

15 and 35 keV. This dependency is shown in Fig. 3.7b, calculated according to Eq. 3.9 with a laser energy of $E_L = 1.17\,\text{eV}$. The horizontal lines indicate the X-ray energies mainly used for this thesis, namely 33 keV for K-edge subtraction experiments and 25 keV and 35 keV for X-ray fluorescence measurements. This corresponds to electron energies of about 42.9 MeV, 37 MeV and 44.2 MeV, respectively. The vertical lines mark the minimum and maximum electron energy of the CLS. Combining the energy spread and the electron beam divergence, the MuCLS provides a quasi-monochromatic X-ray beam with an energy bandwidth of $3 - 5\,\%$ [Günther, 2020]. In Fig. 3.7c the dependency of the beam intensity on the scattering angle is shown, calculated from Eq. 3.17 exemplarily for an X-ray energy of 33 keV. At a half opening angle of 2 mrad, indicated by the dashed lines in the plot, the intensity theoretically decreases by about 7 % of the maximum intensity. Again, the real intensity drop is reduced by the electron beam divergence. Lastly, in Fig. 3.7d the X-ray spectra used for this thesis are presented. The source produces sharp, quasi-monochromatic, partially coherent spectra with a bandwidth below 4.5 % ($\Delta E/E$ at FWHM). The higher energy spectra are more broadened due to the higher spread of electron energies compared to the lower energy spectrum. All peaks are broadened on the lower energy side due to the electron beam divergence which dominates on this side of the peak [Loewen, 2003].

The X-ray flux of the source varies depending on the X-ray energy and reaches a maximum of up to 4.5×10^{10} photons per second [Günther, 2020] at 35 keV with a source size of about $50 \times 50\,\mu\text{m}^2$. In Table 3.1 the source parameters for different X-ray energies are listed. Since the X-rays are emitted into an opening angle of 4 mrad, the beam has an elliptic extent of $62 \times 74\,\text{mm}^2$ at the detector position in the second endstation at a distance of 16.4 m from the source interaction point.

MuCLS parameters	25 keV	33 keV	35 keV
electron energy [MeV]	37	42.9	44.2
rms source size [μm^2]	50×50		
X-ray flux [photons/s]	2.4×10^{10}	3.0×10^{10}	4.5×10^{10}
Brilliance [$\frac{\text{ph}}{(\text{s mm}^2\text{mrad}^2 0.1\%\text{BW})}$]	1.2×10^{10}		

Table 3.1: Source parameters at the MuCLS for X-ray energies of 25 keV, 33 keV and 35 keV. The maximum flux is highly dependent on the X-ray energy. Values taken from [Günther, 2020].

Compared to a conventional laboratory X-ray source, the MuCLS has a narrow energy bandwidth. Together with the determined flux of $\Phi \approx 2.4 \times 10^{10}$ photons/s at 25 keV, the root mean square (rms) source size of $\sigma \approx 50\,\mu\text{m}$, and the angular spread of 4 mrad, the brilliance of the MuCLS can be calculated to:

$$B = 1.2 \times 10^{10}\,\text{photons}\,\text{s}^{-1}\,\text{mm}^{-2}\,\text{mrad}^{-2}\,(0.1\%\,\text{BW})^{-1}. \tag{3.19}$$

In comparison, a rotating anode produces an X-ray beam with a brilliance of $\sim 0.6 \times 10^9\,\text{photons}\,\text{s}^{-1}\,\text{mm}^{-2}\,\text{mrad}^{-2}$ [Skarzynski, 2013] and a third generation synchrotron

a brilliance of $\sim 10^{21}$ photons $\mathrm{s}^{-1}\,\mathrm{mm}^{-2}\,\mathrm{mrad}^{-2}\,(0.1\%\,\mathrm{BW})^{-1}$ [Balewski, 2004; DESY, 2018].

3.4.2 Other inverse Compton sources

In order to give a perspective of the performance at the MuCLS, several other projects with inverse Compton sources are listed in the following. This list is not in the least complete and only means to provide an overview of the projects ongoing worldwide. The projects described in the following are: ThomX in France, BriXs and STAR in Italy, the NESTOR in Ukraine, the LCS at AIST in Japan, the TTX in China and the CXFEL at ASU, the Compton source at BNL ATF, and the Compton project at MIT in the USA.

- **ThomX** The ThomX is an ICS under construction in Orsay, France and is based on a linac and an electron storage ring. It aims to produce monochromatic X-rays in the energy range of $40 - 90\,\mathrm{keV}$ with a photon flux of $10^{11} - 10^{13}$ photons/s, depending on the X-ray energy. Due to the high electron energies of $50 - 70\,\mathrm{MeV}$, the electron storage ring of ThomX is around 18 m in circumference. [Variola, 2011; Jacquet, 2014] ThomX is planning to go into operation in 2020 [Monard, 2018].

- **BriXS and STAR** Two ICSs are being developed in Italy at the moment. One of them is the Bright and Compact X-ray Source (BriXS), which will be installed in Milan and is based on an energy-recovery linac (ERL) using superconducting technology. It is proposed to produce monochromatic X-rays with energies up to 180 keV and a high photon flux of up to 10^{13} photons/s with an expected bandwidth of $1 - 10\%$. The second ICS in Italy is the Southern Europe Thomson back-scattering source for Applied Research (STAR) which is currently being installed at the University of Calabria. The source is based on an S-band linac with a repetition rate of 100 Hz and is designed to produce X-rays in the range of $40 - 140\,\mathrm{keV}$ with a photon flux of up to 10^{10} photons/s and an energy bandwidth of under 10% [Bacci, 2016; Faillace, 2019].

- **LCS at AIST**: The laser Compton scattering (LCS) hard X-ray source at the National Institute of Advanced Industrial Science and Technology (AIST) in Tokyo, Japan, is based on a linac scheme. The main components are a photocathode RF gun followed by two 1.5 m S-band linacs, accelerating the electrons up to an energy of 42 MeV. The electrons collide with laser photons from a Ti:Sapphire laser with a wavelength of 800 nm, producing an X-ray beam with an energy of 10−40 keV. Since the crossing angle of this source can be varied, both X-ray photon yield and pulse width vary. The shortest X-ray pulse width is obtained at a 90° crossing angle with 150 fs providing an X-ray flux of 10^6 photons/s at an energy of $\sim 20\,\mathrm{keV}$. The maximum photon flux is reached at a crossing angle of 15° with 10^7 photons/s with an energy of $\sim 40\,\mathrm{keV}$ and a pulse width of 3 ps [Kuroda, 2011].

- **Compton source at BNL ATF** At the Brookhaven Accelerator Test Facility (ATF) Compton studies are ongoing, using a 10 µm CO_2 laser and a photo-cathode linac. The reported peak brightness is 2.8×10^{18} ph/s/mm^2/mrad^2 for single shot mode [Pogorelsky, 2000]. Ongoing research has the goal to use high-pressure CO_2 lasers to achieve an average brilliance of 3^{10} ph/s/mm^2/mrad^2 at the photon peak energy of 6.4 keV with a 60 MeV linac. After an upgrade of the linac, they expect to achieve a maximum X-ray energy of 600 keV [Pogorelsky, 2016].

- **TTX**: The Tsinghua Thomson Scattering X-ray Source (TTX) in China went into operation in 2012 and is a linac-based source. An electron bunch is generated with a photo-cathode RF and then accelerated to relativistic energies of $30 - 54$ MeV in a 3 m S-band linac. It collides with an infrared laser pulse with a wavelength of 800 nm in a head-on geometry. After a laser upgrade, TTX can now produce X-ray pulses in the energy range $20 - 70$ keV with a maximum photon yield of up to 2×10^7 photons per pulse with a pulse repetition rate of 10 Hz [Chi, 2017; Chi, 2018].

- **NESTOR** In Kharkov, the advanced X-ray source NESTOR (New Electron Storage Ring) is being constructed, which is based on an electron storage ring for electrons with energies from 40 MeV to 225 MeV. By inverse Compton scattering of the electrons with a Nd:YAG laser and variation of the interaction angle, X-rays with an energy of 1 eV to 900 keV are going to be produced. The source is expected to produce an X-ray flux of up to 10^{13} photons/s [Androsov, 2010; Shcherbakov, 2013].

- **ASU CXFEL** At the Arizona State University (ASU) a compact X-ray FEL (CXFEL) is being developed, based on the nanopattering of the electron beam to produce fully coherent X-rays. An RF produces electrons with a few MeV in energy that are then accelerated by a series of linacs to a maximum energy of 35 MeV. By nanobunching of the electron beam and the use of a short pulse laser field as an undulator, the source will work as an XFEL with total length of 10 m [Graves, 2017].

- **Inverse Compton source at MIT** At the Massachusetts Institute of Technology (MIT) a linac-based ICS is under development. Electrons accelerated in a superconducting RF cavity to a maximum of 40 MeV interact with a Yb:YAG laser to produce X-rays in the range of $3 - 30$ keV. The facility can operate in two modes: at high (MHz) repetition rate with flux and brilliance similar to that of a large 2nd generation synchrotron but with short 1 ps pulses, or at 10 Hz with a high flux-per-pulse in single-shot mode. In the former mode, the X-ray flux is expected to be 3×10^{14} photons/s while it is about 1×10^{11} photons/s in the latter [Graves, 2009].

4 Implementation of K-edge subtraction imaging at the MuCLS

While KES is a well-developed technique at synchrotron sources, it has not been routinely applied at laboratory sources. In order to implement KES at the MuCLS, several concepts are imaginable, such as the oscillation of the beam energy and the insertion of an X-ray filter. A quick oscillation of the electron beam energy requires operating the machine in a non-equilibrium state, which makes it non-trivial. Therefore, a filter-based KES approach was implemented at the MuCLS. This approach has been developed at a synchrotron by Umetani et al. [Umetani, 1991; Umetani, 1993] and applied at the MuCLS for first experiments presented in my Master's thesis. This chapter gives in-depth information on the calculation of the KES image and a short introduction to alternative KES approaches. Additionally, the developments of the iodine X-ray filters in the course of this thesis that enabled dynamic KES imaging, and the detectors used for this thesis are described.

4.1 Filter-based K-edge subtraction

While imaging with two completely separately produced monochromatic X-ray beams, one automatically obtains two images with energies bracketing the K-edge of the desired material. When filtering a single spectrum, one obtains two images with different mean energies. These energies are not necessarily above and below the edge. Therefore the necessary post-processing (based on [Kulpe, 2018]) is described in the following.

4.1.1 Calculation of images and noise analysis

The workflow to calculate the two images is shown in Fig. 4.1. By first determining the steps and scaling factors required to obtain a high-energy and a low-energy spectrum without any remaining overlap, the same procedure can then be applied to the filtered and unfiltered image. For this purpose, two spectra have been recorded with a silicon drift-detector (AXAS-D, KETEK GmbH, Munich, Germany) at identical settings, one with the iodine filter and one without the filter. The small peak in the iodine-filtered spectrum is the iodine fluorescence of the filter, which does not influence the image quality of the acquired images due to a larger filter-detector distance in the experimental setup. To obtain two images, respectively containing only the high-energy or the low-energy part of the spectrum, the high-energy part in the iodine-filtered image has to be eliminated as well as the low-energy part in the unfiltered image. Therefore, the iodine-filtered spectrum Fig. 4.1b is weighted such that its intensity corresponds to the one of the low-energy part of the unfiltered spectrum.

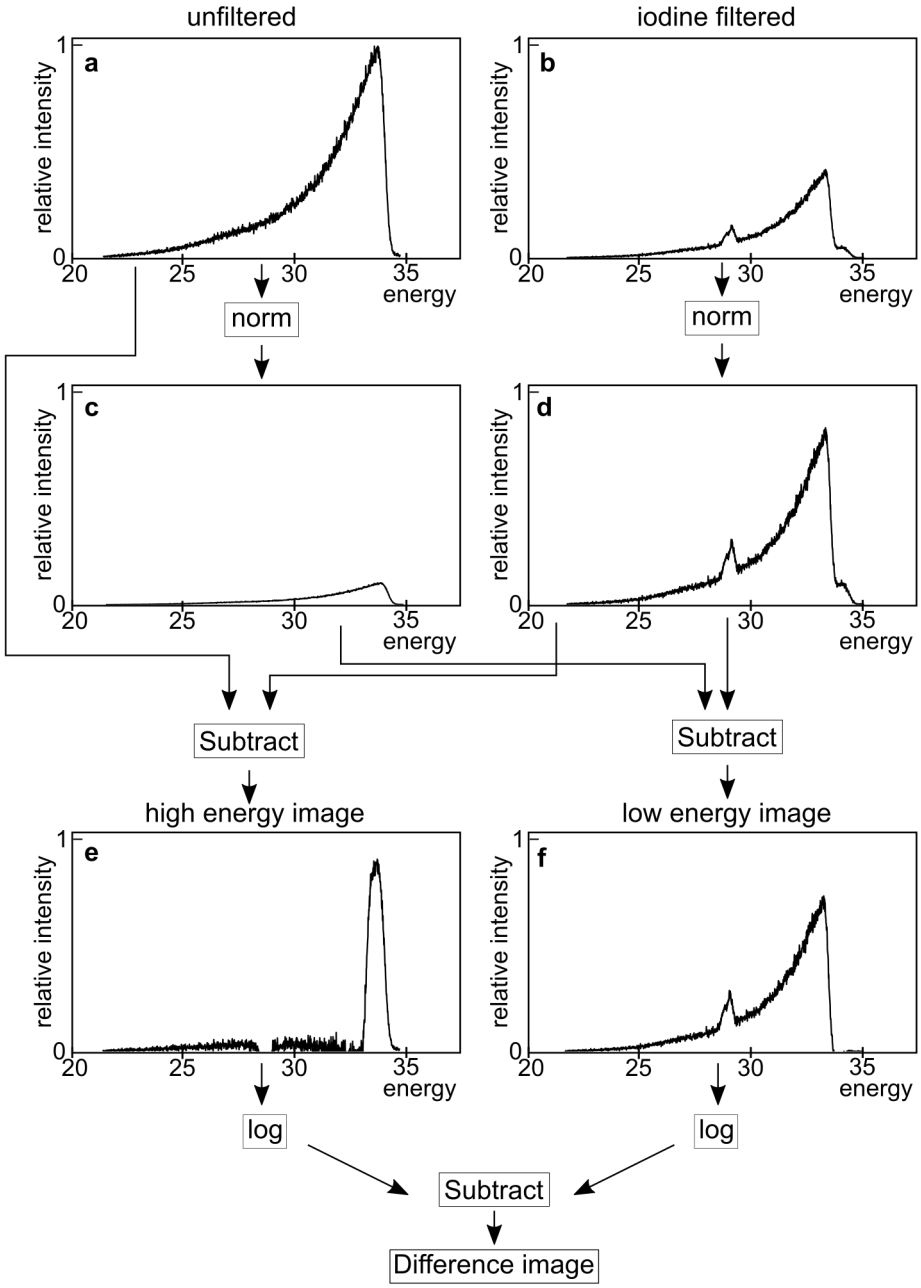

Figure 4.1: Workflow used for calculating a K-edge subtraction image at the MuCLS. First, unfiltered and iodine-filtered images **a** and **b** are recorded and dark current, flatfield and flux corrected. The iodine-filtered image **b** is weighted so that its intensity corresponds to the low energy part of the unfiltered image, which results in the weighted iodine-filtered image **d**. By subtracting image **d** from the unfiltered image **a**, the high-energy image **e** is obtained. To obtain the low-energy image, the high-energy part of the weighted iodine-filtered image has to be eliminated. Therefore, the unfiltered image **a** is weighted so that it corresponds to the remaining high-energy part of the weighted iodine-filtered image. The weighted unfiltered image **c** is then subtracted from the weighted iodine-filtered image **d**, yielding a low-energy image **f**. Finally, the difference image is obtained by logarithmically subtracting the low-energy image from the high-energy image. Adapted from [Kulpe, 2018].

By matching the slope of the filtered spectrum to the unfiltered one, the fraction a of the filtered spectrum contained in the unfiltered one is determined. The reference-corrected iodine-filtered spectrum is multiplied with this factor, resulting in the weighted iodine-filtered spectrum Fig 4.1d. Subtracting Fig. 4.1d from the unfiltered spectrum Fig. 4.1a, the high-energy spectrum Fig. 4.1e is obtained:

$$\text{Image}_{\text{high}} = \text{Image}_{\text{unf}} - a \cdot \text{Image}_{\text{iod}}. \tag{4.1}$$

The same procedure is performed to obtain the low-energy spectrum. This time however, the peak of the unfiltered spectrum is scaled to the remaining high-energy part of the weighted filtered spectrum (visible in Fig. 4.1b and Fig. 4.1d as a little shoulder at bottom of the right slope of the peak) and its ratio b is calculated. The weighted unfiltered spectrum Fig. 4.1c is generated with this ratio. It is subtracted from the weighted iodine-filtered spectrum Fig. 4.1d, producing a low-energy spectrum Fig. 4.1f where the high-energy part of the spectrum is completely canceled out:

$$\text{Image}_{\text{low}} = a \cdot \text{Image}_{\text{iod}} - b \cdot \text{Image}_{\text{unf}}, \tag{4.2}$$

Finally, the desired difference image is obtained by subtracting the logarithmized low-energy from the logarithmized high-energy image:

$$\text{Image}_{\text{KES}} = \log(\text{Image}_{\text{high}}) - \log(\text{Image}_{\text{low}}). \tag{4.3}$$

To eliminate highly absorbing structures, such as aluminum in a phantom or bones, in the subtraction, an empirical energy correction was applied based on the energy dependence of the attenuation coefficient. In the employed energy range, the attenuation is mainly dominated by the photoelectric effect. The resulting E^{-3} dependence away from absorption edges of aluminum and bone is exploited to highlight only regions containing contrast agent. A factor is calculated, which is the quotient of the mean energies of low-energy and high-energy spectra obtained in the aforementioned subtraction to the power of three. It is used to scale the logarithmic low-energy image:

$$\text{Image}_{\text{KES}} = \log(\text{Image}_{\text{high}}) - \left(\frac{E_{\text{mean,low}}}{E_{\text{mean,high}}}\right)^3 \cdot \log(\text{Image}_{\text{low}}), \tag{4.4}$$

with $E_{\text{mean,low}}$ and $E_{\text{mean,high}}$ being the mean energies of the low- and high-energy images, respectively.

Due to the post-processing needed to obtain the KES image, the noise level in the resulting image will be increased in comparison to the noise level of the initial images. The variance (i.e., noise level) of the KES image can be calculated by inserting Eq. 4.1 and 4.2 into Eq. 4.4 and applying the standard propagation of uncertainty, so that it becomes:

$$\sigma^2_{\text{KES}} = \left(\frac{\partial \text{Image}_{\text{KES}}}{\partial \text{Image}_{\text{unf}}}\right)^2_{\overline{I}_{\text{unf}}} \cdot \sigma^2_{\text{unf}} + \left(\frac{\partial \text{Image}_{\text{KES}}}{\partial \text{Image}_{\text{iod}}}\right)^2_{\overline{I}_{\text{iod}}} \cdot \sigma^2_{\text{iod}}, \tag{4.5}$$

with σ^2_{KES}, σ^2_{unf} and σ^2_{iod} being the variances of the KES image, unfiltered image and the iodine filtered images and the derivatives being evaluated for the mean values $\overline{I}_{\text{unf}}$

and $\overline{I}_{\mathrm{iod}}$ of the regions of interest, that is,

$$\left(\frac{\partial \mathrm{Image}_{\mathrm{KES}}}{\partial \mathrm{Image}_{\mathrm{unf}}}\right)^2_{\overline{I}_{\mathrm{unf}}} = \left[\frac{1}{\overline{I}_{\mathrm{unf}} - a \cdot \overline{I}_{\mathrm{iod}}} + \frac{b \cdot c}{a \cdot \overline{I}_{\mathrm{iod}} - b \cdot \overline{I}_{\mathrm{unf}}}\right]^2, \tag{4.6}$$

$$\left(\frac{\partial \mathrm{Image}_{\mathrm{KES}}}{\partial \mathrm{Image}_{\mathrm{iod}}}\right)^2_{\overline{I}_{\mathrm{iod}}} = \left[\frac{a}{\overline{I}_{\mathrm{unf}} - a \cdot \overline{I}_{\mathrm{iod}}} + \frac{a \cdot c}{a \cdot \overline{I}_{\mathrm{iod}} - b \cdot \overline{I}_{\mathrm{unf}}}\right]^2, \tag{4.7}$$

with $c = \left(\frac{E_{\mathrm{mean,low}}}{E_{\mathrm{mean,high}}}\right)^3$.

4.1.2 Alternative approaches to filter-based KES

While the KES approach at the MuCLS uses an X-ray filter to change the X-ray spectrum used for imaging, at synchrotron sources a different instrumentation is usually used. The radiation produced by insertion devices is generally not sufficiently monochromatic to perform imaging directly around the K-edge of a target material. Therefore, the beam is usually made monochromatic by diffraction. The monochromation of radiation with wavelengths shorter than a few nanometers is achieved by using crystal or multilayer monochromators. Thereby the crystalline solids provide a regular array of scattering centers [Willmott, 2011]. For KES imaging at a synchrotron the X-ray beam is usually sent through a crystal monochromator to obtain a fully monochromatic beam [Rubenstein, 1986; Thompson, 1989]. Since the crystal needs to have a high quality, a good ability to dissipate the thermal load, and high resistance to radiation damage, the most commonly used material is silicon. Often a Si crystal with a (111) configuration is used [Umetani, 1991; Elleaume, 2000; Dix, 2003].

While K-edge subtraction works best using a monochromatic X-ray beam, it has also been performed at conventional polychromatic laboratory sources using a Ross filter arrangement [Arhatari, 2017] or a multi-bin photon-counting detector [Roessl, 2007; Schlomka, 2008]. The use of filter pairs provides a well-defined and sharp energy window [Arhatari, 2017]. However, the absorption of a large amount of the X-ray flux in the filters leads to long acquisition times, limiting the applicability for fast X-ray imaging. Detectors with multiple energy bins can also be used to acquire images around the K-edge of a material. However, these detectors usually have an energy threshold resolution of $1 - 2\,\mathrm{keV}$ [Shikhaliev, 2008; Vincenzi, 2015], which limits the ability to acquire images closely around the K-edge. KES imaging can also be performed at conventional polychromatic X-ray sources using 2D pixelated spectroscopic detectors [Pani, 2012; Egan, 2015] with the disadvantage that in some applications the sample is irradiated with a much broader spectrum than needed for the selected energy bins, causing unnecessary radiation dose.

At the MuCLS, a fast energy switching of the compact synchrotron source was also considered before implementing the filter-based KES approach. For this, the electron energy is slightly changed by adjusting the linac settings and the magnet configurations. Since the mirror mountings are very sensitive to changes in the magnetic fields and the

feedback system is very slow, only small jumps in energy of about 1 keV are possible. Larger energy shifts would theoretically be possible. However, these would lead to a larger change in heat load of, e.g., the bending magnets, and thus a less stable X-ray beam. For imaging around a K-edge, only small energy differences are needed so that energy switching of the X-ray source is ideal for this imaging technique. Until now, energy switches between 25 keV and 26 keV and between 26 keV and 27 keV have been performed. Since this process requires a concerted change of a multitude of machine parameters, the switching of the energy takes in the order of seconds. The fastest switch that was achieved in around 1 s. This amount of time is acceptable for KES imaging of a static sample. However, for dynamically changing samples faster energy switches are necessary to record all processes in the sample, e.g., the injection of contrast agent. This can be achieved using a mechanically driven iodine filter. Using a rotational stepping motor with a maximum speed of 2600°/s, 4 images per full rotation and a dead time of 20° between two images, this leads to an acquisition time of 190 ms per image and 60 ms for switching of the filter.

4.2 Development of iodine X-ray filter

After having used a 2 mm water bath filled with iodine contrast agent with a concentration of 400 mg/ml iodine as a filter in previous studies, the goal was to find a solid iodine filter with similar features to enable fast switching of the filter. It was important to find a filter that is stable in air and over time, that does not change after X-ray illumination and gives homogeneous absorption over the whole area of the filter. First approaches for the filter production were presented in my Master's thesis, where sodium iodide was mixed into resin. This did not produce a homogeneous filter due to sedimentation of the sodium iodide powder. Since the effective iodine thickness in the liquid filter was about 180 µm, the solid filter should have a similar iodine thickness. A sodium iodide crystal would have been the most convenient solution. However, sodium iodide is a highly hygroscopic material so that the filter would have had to be sealed air tight and even then a destruction of the filter over time would have been possible. Additionally, the production of such a thin crystal is very challenging and the crystal might break during handling. After several attempts, a solution to produce homogeneous filters in the own laboratory was found. A component containing iodine in a non-ionic form was used so that the final filter would not be hygroscopic or otherwise influenced by components of the air. For the filter production, polyvinylpyrrolidone (PVP) is mixed into commercially available iodine contrast agent (Ultravist 370, Bayer Schering Pharma AG, Germany) until it forms a homogeneous solution. During this process, the transparent Ultravist iodine contrast agent turns into a milky fluid (cf. Fig. 4.2a) and its viscosity increases. The PVP has to be added in portions to avoid clumping and allow for complete dissolution. It usually takes around 24 h before the solution is ready to be poured into a mold. It was tried to use the same protocol for another iodine contrast agent (Imeron 400 MCT, Bracco Imaging, Germany), however this did not lead to the same results. The filtering solution remains clear (cf. Fig. 4.2b)

and there seems to be no reaction between PVP and contrast agent. When solidifying, the filter cracks and cannot be used for X-ray filtering.

Below the exact protocol for the production of the Ultravist filtering solution is listed.

- Take a 100 ml round bottom flask equipped with a magnetic stirrer bar.
- Add 40 ml of Ultravist (iodine content 370 mg/ml).
- Add a total of 4 g PVP in portions of 0.5 g over the course of 8 hours.
- Stir at room temperature. This allows the complete and homogeneous dissolution of PVP in the contrast agent.
- Let the solution stir overnight at room temperature.

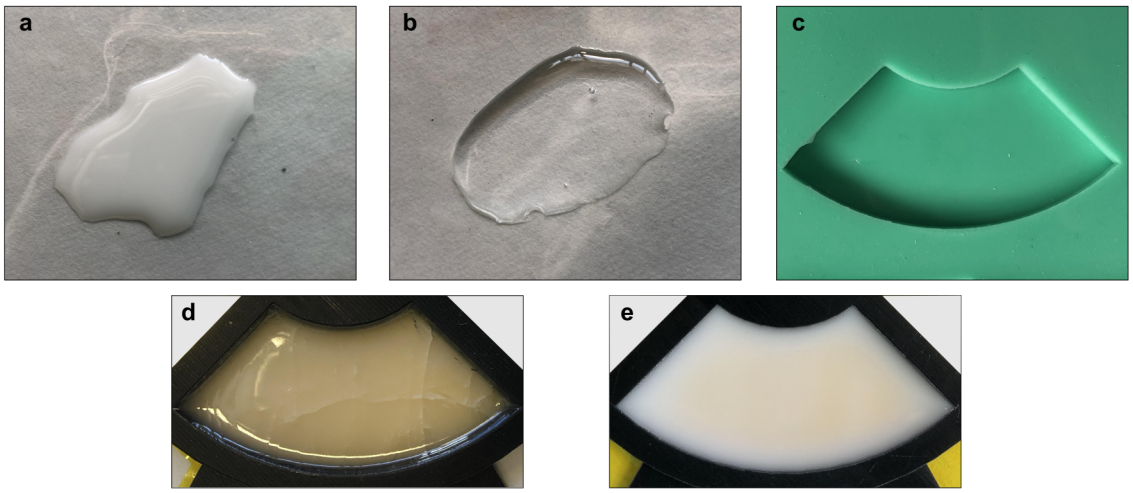

Figure 4.2: Filter solution and silicon mold for iodine filter production: **a** Drop of Ultravist filter solution on clear foil: Final filter solution is a milky white solution that has a high viscosity; **b** Drop of filtering solution produced with Imeron 400 MCT contrast agent: Reaction between PVP and contrast agent does not take place and the filter cracks when solidifying; **c** Silicon molding used for hardening the filter solution. The mold has the final shape of the iodine filter so that no further modification is needed after solidification; **d** Cracked filter that was set into the final container before the filter had completely solidified, **e** Filter that dried completely before being placed into final container and did not develop any cracks.

The prepared filter solution can be then poured into a mold. The filter needs about 1 week to harden such that it can be taken out of the mold. During this time, it is important that there is no air draft at the place where the mold is located or any movement of the mold. This would lead to wrinkles in the surface of the filter. After a week of hardening, the filter seems stable. However, it takes an additional $4-6$ weeks for the filter to solidify completely. During this time, tensions arise inside the filter material so that it might crack if the filter is placed into a container with hard borders. Therefore, the filters used for the experiments presented in this thesis, especially for

those on dynamic KES imaging, presented in Ch. 6, were hardened in a silicon mold (cf. Fig. 4.2c) for a total of 6 weeks before being demolded. Since the molds had the shape needed for the final iodine filter, no further modification of the filters was needed after hardening. Only then were the filters placed into their final container.

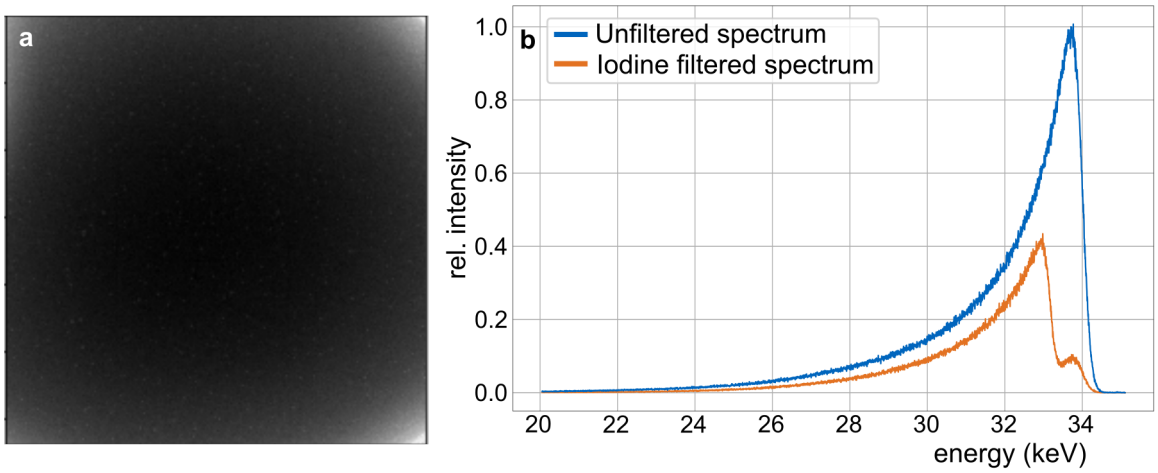

Figure 4.3: X-ray absorption image of iodine filter together with 33 keV MuCLS spectrum with and without filtering: **a** The X-ray image of the iodine filter shows that the absorption of the filter is homogeneous over the whole field of view; **b** The filter not only absorbs the part of the spectrum above the iodine K-edge, but reduces the intensity of the spectrum as a whole. This can be seen when comparing the unfiltered and the filtered spectra. The main part of the absorption, however, takes place above the iodine K-edge, where only 3 % of the initial spectrum remain after filtering.

Fig. 4.3 shows an X-ray image of the iodine filter together with the spectrum of the MuCLS at 33 keV with and without filtering. The filter shows homogeneous absorption properties for the whole field of view. This is important as the homogeneity of the spectral absorption influences the image quality in KES. If there are spacial differences in the X-ray spectrum used to acquire the iodine-filtered image, the subtraction mechanism will not perform evenly well in all regions of the image. The filter shown in Fig. 4.3a has an effective iodine thickness of $\sim 180\,\mu m$. The spectrum in Fig. 4.3b shows that the filter does not only absorb the part of the spectrum above the iodine K-edge, but reduces the intensity of the spectrum as a whole. This can be seen when comparing the unfiltered and the filtered spectra. However, the majority of the absorption takes place above the iodine K-edge, where only a small portion of the spectrum remains. It was calculated that this accounts for 3 % of the initial high energy part of the spectrum. For a MuCLS X-ray spectrum with a peak energy of 33.69 keV (which was, e.g., used for the KES CT experiments in Ch. 5.2), the filtering shifts the mean energy from 33.18 keV to 32.59 keV. This produces two X-ray spectra with mean energies above and below the iodine K-edge and an energy separation of 0.59 keV. Since Sarnelli et al. [Sarnelli, 2006] showed that a smaller energy separation is beneficial for the contrast in the KES image, this energy separation is considered ideal.

4.3 X-ray detectors at the MuCLS

Digital X-ray detectors work with two different concepts, either measuring currents or voltages. As the current produced by a single photon is very small, most detectors work with voltage measurements. One discriminates between integrating, photon-counting and energy-resolving detection.

Detector	Dexela 1512	Pilatus 200k	hamamatsu sCMOS - C12849-101U	Ximea CCD Camera - xiRAY
Position	endstation 2	endstation 2	endstation 1	endstation 1
Scintillator / Sensor	Gd_2O_2S:Tb, 150 µm	Si, 1000 µm	P43, Gd_2O_2S:Tb, 10 µm	P43, Gd_2O_2S:Tb, 22 µm
FOV [pixel] [mm]	1536 × 1944 114.9 × 145.4	487 × 407 83.7 × 70.0	2048 × 2048 13.3 × 13.3	4008 × 2672 37.3 × 25.7
Pixel size	74.8µm	172.0µm	6.5 µm	9.0 µm
PSF (σ)	71µm	172µm(box)	8 µm	12 µm
max. frame rate	26 fps	20 fps	30 fps	2.1 fps
Dynamic range	14 bit	20 bit	16 bit	14 bit

Table 4.1: Detectors available in both endstations at the MuCLS are used for this thesis. The abbreviation FOV stands for field-of-view, PSF for point spread function and fps for frames per second.

In an integrating detector, the voltages produced by the detected photons accumulate until the end of the exposure time. The total charge is read out only at the end of the exposure. This type of detection is used in X-ray films, charge-coupled devices (CCDs) and flat-panel detectors. Both flat-panel detectors and CCDs use scintillators to convert X-rays to visible light with an intensity proportional to the X-ray energy. There are certain characteristics needed for a suitable scintillator material. In order for these detectors to sufficiently detect, i.e., absorb, the incoming X-rays, the material must have a high density and contain elements with a high atomic number (usually $Z > 50$). Additionally, the conversion rate of X-rays to visible light should be high, while the after-glow of the material should be short. To ensure high image resolution, the scattering of the visible photons in the material should be low and the detection at the photodiode high. While a thick scintillator will have a high absorption efficiency and thus allow for short acquisition times, its resolution will be lower than that of a thinner scintillator. In a flat-panel detector, the visible light is then usually detected by an array of photodiodes and converted into a digital signal. In a CCD detector, the visible light is coupled into a fiber optical plate (FOP) before it is collected and

converted into a digital signal. The FOP has the function to protect the CCD from the non-absorbed X-radiation that passes through the scintillator and might damage the CCD due to its high energy. While integrating detectors are relatively easy to produce, they have the disadvantage that they cannot discriminate photons by their energy.

This is different in photon-counting detection, where individual photons are counted. An incoming photon interacting with the sensor material produces a number of electron-hole pairs proportional to its X-ray energy. Therefore, each detected photon is converted to a voltage peak with a height corresponding to the energy of the photon. This allows for the discrimination of photons by their energies, i.e., energy-resolving detection. By setting an energy threshold to exclude low energy photons, noise – especially dark-current noise – is reduced. Additionally, since every photon is counted separately and there is no integration over the exposure time, readout noise is avoided. Therefore, photon-counting detectors have a box-like point spread function (PSF). The counting efficiency is limited by the quantum efficiency and any electronic losses in the system. The advantage of a detector working with this principle is a very short readout time, and thus high imaging frame rates, and a superior signal-to-noise-ratio (SNR) compared to integrating detectors. However, these detectors have rather complex technologies and currently smaller field-of-views.

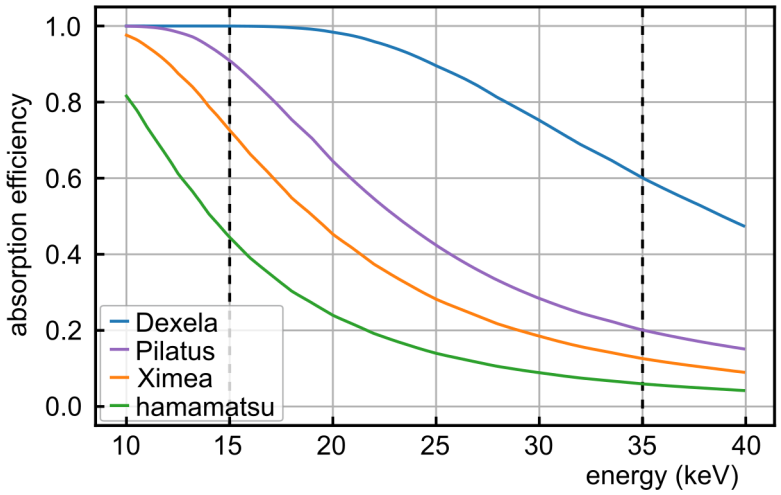

Figure 4.4: Attenuation coefficients of the scintillator or sensor materials of the detectors available in the experimental endstations at the MuCLS.

In both experimental endstations at MuCLS, several detectors for image and spectrum acquisition are available. This chapter focuses on the detectors used for the work presented in this thesis. The detailed information on the detector characteristics is presented in Table 4.1. For the KES experiments, which were performed in the second experimental hutch, two different detectors were used: Dexela 1512 flat-panel detector (PerkinElmer, Inc., USA) and a Pilatus 200k photon-counting detector (Dectris Ltd., Baden, Switzerland). The XRF experiments were performed in the first experimental endstation using the KETEK AXAS-D spectral detector (KETEK GmbH, Munich, Germany), and a hamamatsu sCMOS - C12849-101U (Hamamatsu Photonics,

Hamamatsu, Japan) and a Ximea CCD Camera - xiRAY (XIMEA GmbH, Münster, Germany) flat-panel detector for the optimization of the sample position. The KETEK AXAS-D is a silicon-drift energy dispersive detector used for the measurement of spectra or fluorescence. It has 450 µm of silicon covered by a 8 µm Be window, a chip size of 20 mm^2 and 8192 channels with an energy resolution of < 133 eV at 5.9 keV (FWHM).

The detectors used for this work all have sensor or scintillator materials that have good absorption properties at the energy range of 15 keV to 35 keV. Fig. 4.4 shows the plotted absorption coefficients for the detectors presented in Table 4.1. While the absorption by all materials decreases with increasing X-ray energy, the absorption by Si reduces most. This limits the minimum acquisition time needed for dynamic KES imaging.

5 K-edge subtraction angiography at the MuCLS

According to the World Health Organization (WHO), diseases of the cardiovascular system are responsible for about one third of deaths worldwide and are one of the most probable causes of death [WHO17]. Next to reducing major health risks like obesity, high blood pressure and inadequate physical activity, providing better access to medical care is one of the major measures to reduce deaths from cardiovascular disease.

Atherosclerosis is a common disease and primary cause of cardiovascular disease. It can lead to occlusion of the vessels, causing under-supply of cells with oxygen, and to coronary diseases, such as a myocardial infarction (heart attack). After such an occlusion, it is necessary to find the blocked blood vessel. One of the most commonly used examination methods for this diagnosis is coronary catheter-angiography, which is commonly combined with a temporal subtraction method, namely DSA, to improve the visibility of the blood vessels. DSA is one of the most important examinations in the diagnosis of cardiovascular disease and in the treatment of blood vessels [Meijering, 1999; Reinhold, 2014; Hochmuth, 2002]. It is highly effective in enhancing contrast between vascular structures and surrounding soft tissue as well as bone. However, artifacts caused by patient motion, respiration and cardiac motion limit the application of this method. The resulting artifacts are particularly severe when imaging coronary arteries [Yamamoto, 2009]. Additionally, this technique suffers from complications associated with the high amount of iodine-based contrast media that are injected during the catheterization procedure. Especially for patients with pre-existing renal insufficiency, there is a high risk to suffer from renal failure due to nephrotoxic effects of iodine-based contrast agents, resulting in severe renal dysfunction and a high risk of subsequent dialysis treatment [Adams, 1973; Gruberg, 2000; Tavakol, 2011]. In addition, several patients show allergic reactions following iodine injection, with the risk of a life-threatening anaphylaxis [Tavakol, 2011]. A high amount of iodine can also induce hyperthyroidism by influencing the endocrine function of the thyroid gland [Molen, 2004]. The number of patients harmed by these adverse effects can be lowered if a good diagnostic image quality is achieved with a reduced amount of contrast media being injected.

In contrast to DSA, where two X-ray images are taken before and after the injection of the iodine contrast agent, images in KES imaging are both taken after the injection, but at different X-ray energies. Elleaume et al. [Elleaume, 2002] showed that this makes the method more suitable for imaging moving organs. However, as highly brilliant X-rays are required for this imaging method, it has been limited to synchrotron facilities so far. Rubenstein et al. [Rubenstein, 1981; Rubenstein, 1986] were the first to describe a dual-energy subtraction technique using synchrotron radiation, imaging coronary arteries around the K-edge of iodine. Elleaume et al. [Elleaume, 2000] showed that it is possible to acquire high quality images at a synchrotron for coronary angiography on patients

after intravenous injection of iodine contrast agent. A comparison in [Schültke, 2005] of dual-energy KES imaging with conventional X-ray spectra and KES imaging with monochromatic X-rays demonstrated improved quality for images of the neurovascular system when imaging with monochromatic X-rays. Especially for small vessels that could be blocked by a catheter used for injection, this small-animal study concluded that intravenous injection combined with the KES method at a synchrotron lowers patient risk while achieving higher images quality. In order to enable KES without changing the X-ray energy of the synchrotron source, Umetani et al. [Umetani, 1991; Umetani, 1993] suggested the use of an X-ray filter that partially absorbs the X-ray spectrum and thereby changes its mean energy.

While synchrotrons provide highly brilliant, monochromatic X-rays, they rely on electron storage rings of several hundred meters in circumference and are expensive in terms of installation as well as operation and maintenance. In contrast, the use of conventional X-ray tubes in laboratories and hospitals is comparably cheap, but they exhibit low brilliance and polychromatic X-ray spectra. A conventional X-ray spectrum will be modified as it traverses the patient, which can interfere with the goal to optimize both dose level and image quality. As KES imaging strongly depends on a monochromatic X-ray beam, its feasibility in clinical routine has been limited. Compact synchrotron X-ray sources provide monochromatic X-ray beams with brilliances between those of a large-scale synchrotron and a conventional X-ray source. The development of ICSs enable the transfer of certain techniques that have been limited to synchrotrons so far, like KES imaging, into a laboratory or pre-clinical environment.

Several experiments on angiography exploiting the advantages of monochromatic imaging have been performed at the MuCLS in the past. This chapter gives an overview of this previous work on angiography in projection imaging and presents the developments that were made to enable KES CT at this source.

5.1 Previous work on angiography at the MuCLS

While angiography is a well-established and common procedure in clinical routine, several development steps were necessary to perform this imaging technique at the MuCLS. In the following sub-chapters, the previous achievements in angiography at the MuCLS are described. These showed the major advantage of monochromatic imaging in comparison to conventional polychromatic X-ray imaging and the applicability of a filter-based KES approach to an ICS.

This chapter presents and summarizes previous work that has been published in the following publications: [Eggl, 2017], [Kulpe, 2018] and [Kulpe, 2020b]. Note that part of this chapter draws text and figures directly from the two last publications.

5.1.1 Monoenergetic angiography

While conventional X-ray tubes are well-established in clinical X-ray imaging, their broad bremsstrahlung spectra have a number of drawbacks in terms of image quality. The polychromatic X-ray spectrum can impede the aim to optimize both the dose level and the image quality, as the X-ray energy cannot be tuned directly to the desired range. A monochromatic X-ray beam, however, is able exploit the sudden increase of the absorption coefficient of a contrast medium at its K-edge. Coronary angiography is a clinical application that could benefit significantly from a monochromatic X-ray beam as it relies on the application of contrast media.

In their study, Eggl et al. [Eggl, 2017] analyzed the quantitative effect of quasi-monochromatic X-ray spectra on the CNR of coronary angiographic images. For this purpose, they used projection images calculated from segmented patient data of a human coronary artery and compared a typically used clinical X-ray spectrum with an ICS spectrum. For an iodine-based contrast agent, a conventional X-ray tube spectrum at 60 kVp was compared to a quasi-monochromatic spectrum at 35 keV. Additionally, a 90 kVp conventional X-ray tube spectrum and a 55 keV quasi-monochromatic spectrum were examined for the application of gadolinium-based contrast media.

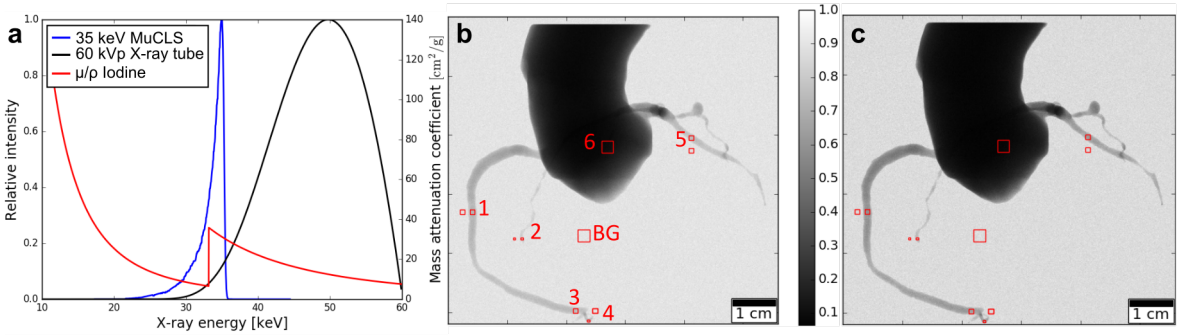

Figure 5.1: **a** Measured MuCLS spectrum at 35 keV peak energy together with an X-ray tube spectrum at 60 kVp and the mass attenuation coefficient of iodine; **b** Simulated iodine-based angiography image for the polychromatic 60 kVp X-ray tube spectrum; **c** Simulated iodine-based angiography image for the 35 keV MuCLS spectrum. Figure adapted from [Eggl, 2017].

As an example, the simulated angiographic images for 60 kVp and 35 keV are shown in Fig. 5.1 together with the used spectra. Comparing the two images, the visibility of small vessels (ROI 1 and 2) is higher for the monoenergetic image. Eggl et al. performed a CNR analysis that supports this impression with CNR values lying $17-22\,\%$ higher in the monoenergetic images than in the case of the conventional spectrum. For lower concentrations of contrast agent, the advantage of monoenergetic imaging increases further. This suggests that the use of a monoenergetic spectrum would allow for a reduction of the iodine concentration by approximately $20-30\,\%$ at almost equal CNR, which can facilitate the administration of the contrast agent for the patients. For the simulations with gadolinium similar results were obtained, with an even

larger improvement in CNR. This proof-of-principle study suggests that the compact synchrotron technology offers great potential in the field of coronary angiography by reducing the amount of required contrast medium concentration.

5.1.2 KES imaging for coronary angiography

To fully exploit the advantages of a quasi-monochromatic X-ray beam, a subtraction imaging technique, namely KES, was implemented at the MuCLS using the filter-based approach described in Ch. 4.1.

A series of experiments was performed to demonstrate the feasibility of a filter-based KES technique. Details on the experimental setup and imaging parameters can be found in [Kulpe, 2018]. First, a phantom was constructed of an empty acrylic glass container with plates of aluminum mounted in front of a tube filled with undiluted iodine-based contrast agent (IMERON 400 MCT, Bracco Imaging, Germany). This phantom mimics a bone in front of an iodine-contrasted blood vessel, as it is commonly the case in clinical applications. A series of experiments with different thicknesses of aluminum was performed to evaluate how the CNR between iodine and aluminum changes with increasing thickness. It was shown that only KES together with an energy correction procedure removes the aluminum while the iodine tube remains visible. Nevertheless, areas where aluminum was located are still visible as the noise in these regions is increased in comparison to the empty background. This is due to the high absorption of the aluminum, which results in a lower photon statistic and thus higher photon noise. As the absorption of the aluminum depends on its thickness, the visibility gain in dependence on the thickness of the aluminum was evaluated. It was found that the CNR is reduced in the KES image when the aluminum thickness is low as the gain in contrast is not higher than the increase of the noise level. Only when the absorption in the aluminum is high, leading to a low contrast between iodine and aluminum in the non-subtraction image, an increase in CNR can be reached by applying KES.

In a second experiment, undiluted iodine-based contrast agent was injected via catheter into the onset of the coronary artery of an excised porcine heart. Fig. 5.2a-c show X-ray images of the left anterior descending artery (LAD) of a porcine heart. In both the unfiltered images and the iodine-filtered ones, the coronary artery with some smaller branching vessels is visible. The visibility of the coronary arteries is limited in both images due to overlying structures of the heart muscle and inhomogeneous absorption in the sample. In contrast, the KES image exhibits only the blood vessels though the noise is increased. Nevertheless, even small vessels are easily recognizable although the image quality is slightly compromised by some contrast agent leaking outside of the vessels.

To simulate ribs of the chest overlying the coronary arteries, a porcine coastal arch was placed in front of the heart in the experimental setup in a final step (Fig. 5.2d-f). Here, the blood vessels are overlaid with bones, further reducing the vessel contrast, especially of the small vessel indicated by the arrows in Fig. 5.2d. After KES with energy correction, only the blood vessels remain visible, reproducing the phantom

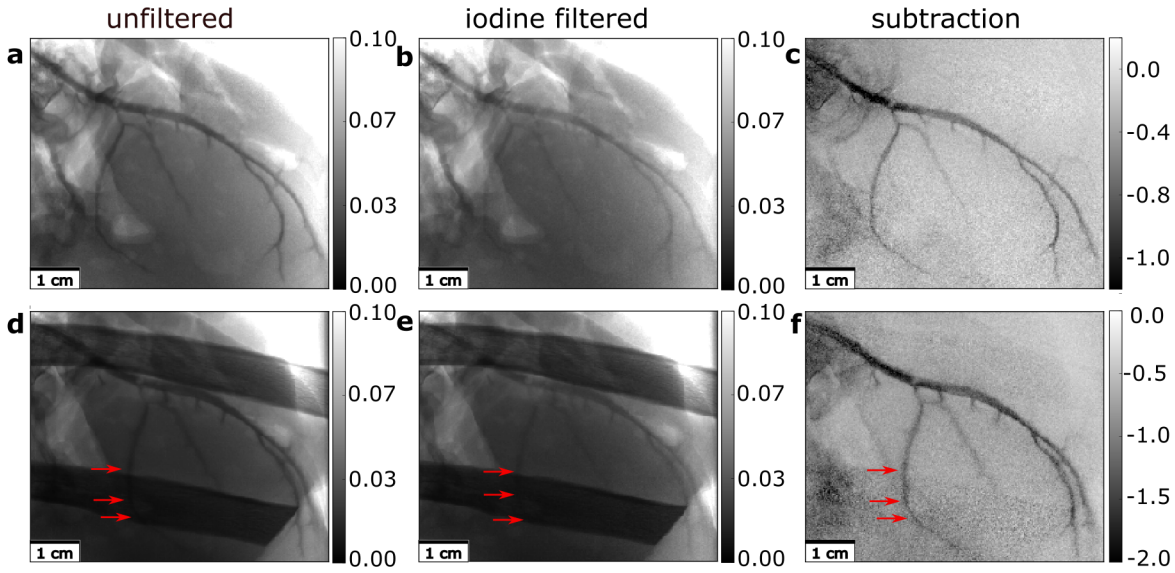

Figure 5.2: K-edge subtraction imaging of the left anterior descending artery of a porcine heart with injected iodine contrast agent and inhomogeneous background structures: First row: In both, the unfiltered **a** and the iodine-filtered **b** image, air artifacts and inhomogeneous absorption make the identification of small blood vessels difficult. In the KES image **c**, only the contrast agent remains visible; Second row: The overlying bone structures make the identification of the small blood vessel (marked by the red arrows) impossible in images **d** and **e**. Only KES imaging combined with an energy correction restores contrast for these blood vessels. Although the image quality is compromised in the KES image **f** in areas of lower counting statistics by noise, the visibility of the small vessels is increased. The gray scales of the images were chosen such that the contrast for the coronary arteries is optimized. The gray scales for the unfiltered and filtered images show the relative intensity of the X-ray beam while the gray values in the KES images show the negative differences in the absorption. Figure from [Kulpe, 2018].

results in a realistic application. KES allows to level out inhomogeneous absorption and to remove uncontrasted tissue structures from the subtraction image. As X-ray transmission through bones is low at an X-ray energy of 33.49 keV, the noise level is significantly higher in regions where the bone is located. The CNR between the blood vessel behind the rib and the rib bone is significantly increased by KES in comparison to the non-subtraction image. This supports the visual impression of better visibility of the small blood vessel hidden behind the rib bone.

The results of these proof-of-principle experiments demonstrate that the quasi-monochromatic spectrum of the MuCLS enables filter-based K-edge subtraction imaging. The proven beneficial characteristics of the compact synchrotron source at the MuCLS were applied to the realistic anatomy of the heart inside the rib cage. While the global noise level is generally compromised by the subtraction of two noise afflicted images, the local CNR of an iodine filled vessel is improved by the subtraction of strong absorber materials like the costal bones. Our experiment with a porcine heart and a costal arch demonstrates that KES strongly improves the visibility of small blood vessels, which

are otherwise undetectable in the conventional image.

5.1.3 KES imaging for iodine and calcium separation

The primary cause for cardiovascular diseases is atherosclerosis [Bentzon, 2014], which causes structural degradation of arterial blood vessels. The accumulation of white blood cells and fat, cell proliferation and inflammatory responses cause stiffening and thickening due to the formation of plaque on the vessel walls [Kuhlmann, 2014]. The plaque can also contain calcifications which build up at the base of older lesions of the vessel [Bentzon, 2014]. The formation of plaque is a process of several years or even decades and can remain asymptomatic [Stary, 2000]. Often, atherosclerosis is only diagnosed after a cardiac infarction or a stroke. It is known that atherosclerosis tends to occur more often at branchings, curvatures and constrictions of arteries [Bentzon, 2014] since the blood flow is not only laminar but turbulence occurs at the outer wall of the vessel. This turbulence leads to a reduction of shear stress acting onto the arterial wall, which further leads to a disorder of the endothelial cells, making the arterial wall more permeable for other cells. Accumulation of cholesterol in the arterial wall and formation of plaque that can eventually rupture and cause a total closure of the vessel are the long term consequence [Kuhlmann, 2014].

To demonstrate the ability of KES to separate iodine and calcium in projection imaging, first a phantom containing the two materials was constructed. The experimental details can be found in [Kulpe, 2020b]. Additionally, a human carotid artery with calcification and a sodium iodide solution with an iodine concentration of 50 mg/ml inside a micro-centrifuge tube, were imaged. The project was approved by the local ethics committee and complies with the Declaration of Helsinki of 1975, as revised in 2008. Written informed consent to provide tissue for research purposes had been obtained from the donor or the donor's relatives.

In Fig. 5.3, the acquired images are shown. In the unfiltered reference image Fig. 5.3a, the calcifications of the carotid can be seen in the right branch and on the left side of the vessel wall at the branching of the two blood vessels. The absorption of the iodine solution is identical to the absorption in the calcification at the branching. Since in a clinical setting the iodine contrast agent would be flowing through the carotid, the two materials would not be easily separable. In the KES image Fig. 5.3b, only the iodine solution remains visible. The calcifications and the iodine can therefore be distinguished through KES imaging. With an additional energy correction, the subtraction can be done in such a way that only the calcifications remain visible in the image Fig. 5.3c. However, their identification is more difficult than in the *ex situ* case here due to the tissue structures and the high noise level. Since KES is a method that separates contrast agent from surrounding materials, the vessel wall and the calcification cannot be separated if both are visible in the conventional unfiltered X-ray image. In other words, KES allows to unambiguously identify which of the highly-absorbing structures in the unfiltered image are due to iodine contrast agent. By elimination, this allows to associate remaining high-contrast features with calcifications.

In its natural state, the vessel would be embedded inside other tissue and filled with blood, so X-ray contrast of the vessel walls would not be as prominent as in the *ex situ* images here and highly absorbing features would either be calcifications or iodine. Therefore, in a more realistic setting, the KES image (Fig. 5.3b) and energy corrected KES image (Fig. 5.3c), would only show iodine and calcifications, respectively.

While the separation of iodine from calcifications in blood vessels is a big issue in clinical diagnostics, it could be shown in a proof-of-principle experiment that the separation in projection images is possible when using an X-ray source with a narrow spectrum, as provided at the MuCLS, and the method of KES. While the attenuation values μd of iodine and calcium solutions were identical in the unfiltered reference image, only the iodine solution remained visible in the KES image. With further correction during the subtraction, it was also possible to highlight the calcium in the image and eliminate the iodine. These experiments show that using KES imaging at a compact synchrotron source enables the differentiation of iodine contrast agent from calcium. This allows for identification of calcifications in blood vessels via radiography.

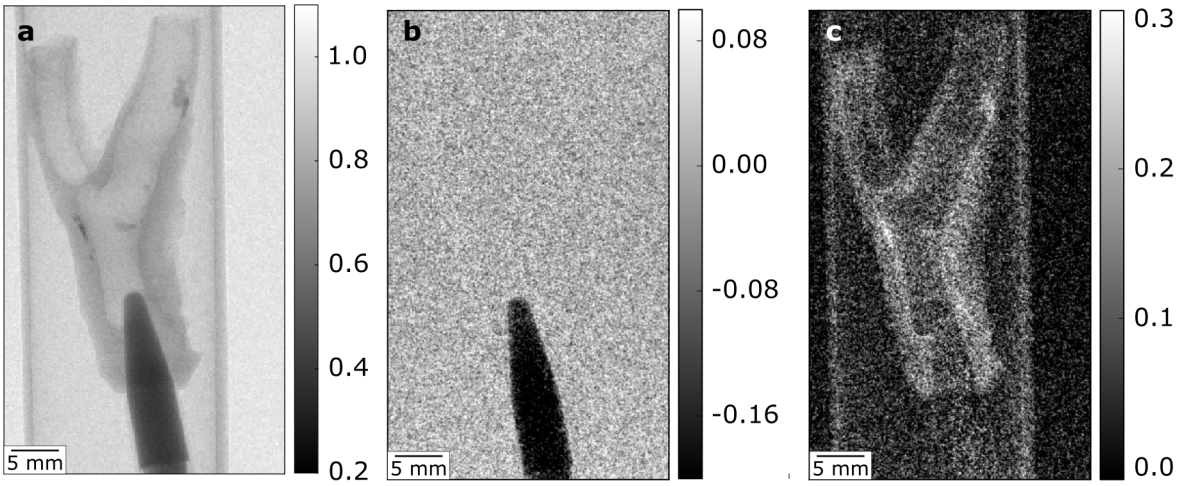

Figure 5.3: Projection images of the human carotid: **a** Reference X-ray image; **b** KES image; **c** KES with an additional energy correction so that the calcifications and not the iodine is visible. The gray scales for the reference X-ray image shows the relative intensity of the X-ray beam, while the gray values in the KES and energy-corrected KES images show the negative differences in the absorption. Figure adapted from [Kulpe, 2020b].

5.2 KES CT of porcine kidney – Separation of iodine and calcium in computed tomography

While KES was successfully performed at the MuCLS in projection imaging, the separation of iodine contrast medium and calcium is also a common topic in clinical CT. Therefore, in this work the technique of KES was applied to three-dimensional imaging. The following chapter describes the successful implementation of KES CT of a porcine kidney.

Note that part of this chapter draws text and figures directly from the publication: Kulpe et al., K-edge Subtraction Computed Tomography with a Compact Light Source. Scientific Reports 9, 13332 (2019) [Kulpe, 2019].

5.2.1 Motivation

CT is one of the most important imaging techniques in clinical diagnostics. Since its development in 1973 by Hounsfield [Hounsfield, 1973], the number of CT procedures performed in the United States alone has reached approximately 74 million in 2017 [IMV, 2017]. Technical advances in the past decades have increased the clinical impact of CT and significantly enhanced its widespread use in diagnostics [Kalender, 2006]. Among these developments is contrast enhanced CT.

Contrast enhance CT is used in a range of applications, e.g., in renal imaging, where iodine contrast agent is commonly applied for examinations of the renal parenchyma (e.g., for detection and characterization of tumors), to illustrate the arterial blood supply of the kidneys (e.g., for detection of artery stenosis or bleeding) and to visualize the urinary tract using delayed phase images, when the contrast agent passed the kidney and is visible within the ureter (e.g., to rule out ureteral obstruction). Fig. 5.4a shows CTs of a patient with a kidney stone in the ureter (indicated by the white arrow), which could block urine flow.

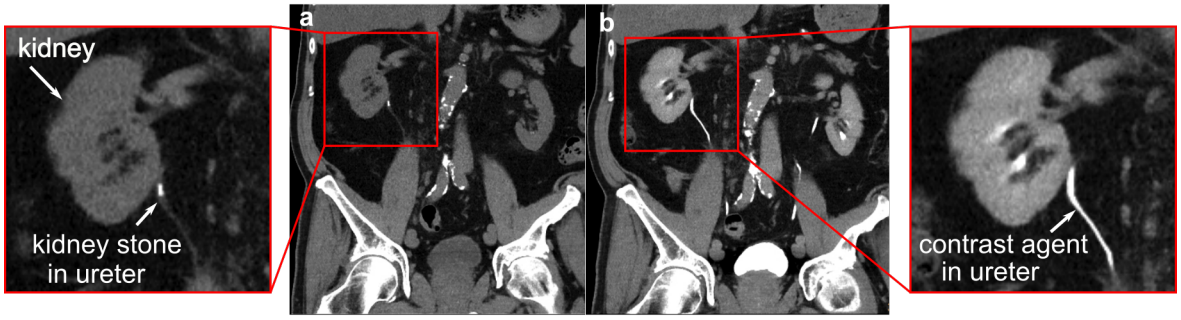

Figure 5.4: Clinical X-ray CT images before (**a**) and after (**b**) administration of iodine contrast agent. In the CT image in **a** the kidney stone is clearly visible in the proximal part of the right ureter. However, after the injection of contrast agent **b** the kidney stone in the ureter cannot be distinguished from the iodine contrast agent and would be missed. Figure from [Kulpe, 2019].

To decide on further treatment, iodine contrast agent is injected into the blood stream to contrast the urine flow through the ureter after the contrast agent has been filtered from the blood. Yet, the contrast agent in the ureter gives a similar absorption signal as the kidney stone (cf. Fig. 5.4b) so that the discrimination of the two can only take place by taking two CT scans, a non-contrast scan before the injection of the contrast agent and one with contrast agent in the excretory phase. These have to be taken with a sufficient time span between them to ensure having contrast agent in the ureter in the contrasted scan.

In conventional X-ray imaging, the image contrast arises from variations in absorption of different materials. However, since the absorption is dependent on the elemental composition and density of the material, the elemental composition of soft tissues is rather similar and the attenuation contrast is weak. In subtraction X-ray imaging, tissue structures or organs are visualized using a contrast medium that changes the attenuation between the contrasted structure and the surrounding tissue [Thomlinson, 2018]. Yet, the iodine in contrast agents absorbs X-ray radiation similarly to calcium, e.g., in calcifications or kidney stones, as their attenuation coefficients are very similar when using the iodine concentrations common for the clinical routine. KES imaging can be used to discriminate the two materials as this method generates an image only displaying the contrasted structure. Other anatomical structures or bones are eliminated as their attenuation stays basically constant. When imaging around the K-edge of iodine, the attenuation coefficient μ/ρ of iodine will change clearly while the attenuation coefficient of calcium will remain almost unchanged. By subtracting the two images, the jump in the attenuation coefficient of iodine will become visible and make the discrimination of iodine and calcium possible. This can solve issues where the attenuation of a tissue is enhanced by a contrast agent such that it becomes indistinguishable from another highly-absorbing structure. Although KES imaging at a polychromatic laboratory source has been demonstrated recently using a Ross filter arrangement [Arhatari, 2017] or a multi-bin photon-counting detector [Roessl, 2007; Schlomka, 2008], there are disadvantages limiting its common application. In the past, KES imaging has usually been performed at synchrotrons.

Synchrotrons providing highly brilliant, monochromatic X-rays, commonly used for KES imaging, offer several advantages for CT compared to conventional broad X-ray spectra. Besides generating a significantly higher photon flux, beam hardening artifacts are absent [Stonestrom, 1981; Dilmanian, 1991]. After some major improvements in image quantification, elemental sensitivity and soft tissue contrast, Dilmanian et al. [Dilmanian, 1997] performed the first temporal K-edge subtraction CT. Since then, KES imaging has been an established technique at synchrotron facilities. Most of the K-edge imaging methods at synchrotrons use a beam that is significantly wider in the horizontal direction so that the sample has to be scanned in vertical direction, allowing for μCT applications [Chappard, 2006]. Others use X-ray optics to expand the beam vertically [Thomlinson, 2018], which enables investigation of larger samples. In several feasibility studies, it has been shown that monochromatic KES CT provides improved image quality and quantitative accuracy compared to conventional polychromatic CT [Nachaliel, 1992; Strengell, 2014; Dix, 2003]. Additionally, the use of special monochromators allows for the simultaneous acquisition of both CT scans below and above the K-edge, providing an advantage for the imaging of living specimens [Suortti, 1993; Schültke, 2011]. Although KES CT has been successfully performed at synchrotrons in the past, the integration of synchrotrons into a clinical setting is difficult. Not only are synchrotrons expensive both in installation and maintenance, but also their size further limits their usage for clinical applications. Additionally, the typical beam size provided by a synchrotron is far below the beam size needed for clinical diagnostics. ICSs provide high monochromatic flux X-ray beams in a laboratory frame and may

have the potential to make KES imaging available in a clinical setting in the future [Strengell, 2014]. Currently, many projects to build inverse Compton sources are ongoing to overcome the limitations of synchrotron sources. At the MuCLS, it has already been shown that a quasi-monochromatic CT performed at an ICS provides improved image quality in comparison to CTs taken at a conventional rotating anode source [Achterhold, 2013].

To further explore the advantages of this new X-ray source, the imaging setup has been further developed to enable KES CT. Here we present a proof-of-principle of KES CT of a porcine kidney at the MuCLS. For this, two CT scans were performed; one with the unfiltered spectrum of the MuCLS and a second with the iodine filtered spectrum. We demonstrate the differentiation of iodine-based contrast agent from a calcium-based kidney stone. It is shown that KES CT solves the clinically faced problem of indistinguishability of iodine and calcium.

5.2.2 Challenges in sample preparation and contrast agent injection

For the measurements, the kidney from a 5-month-old female pig of the race German Landrace was taken. The animal was euthanized in strict accordance to standard guidelines of an animal experiment proposal approved by the Institutional Animal Care and Use Committee of the Technical University of Munich. The organs were removed and further used according to the 3R principle (reduce, refine, replace). The kidney stone was derived from a patient at the university hospital Klinikum rechts der Isar, following the common clinical practice with respect to their individual diagnosis and indication, and after the finalization of the histopathological analysis. Written and informed consent was obtained from the patient. The study was approved by the ethics committee of the Klinikum rechts der Isar, Technical University of Munich.

Iodine contrast agent was injected into the renal artery with a syringe so that it spread into the whole arterial tree of the kidney. The procedure of injection had already been tested in previous experiments on coronary arteries of the porcine heart and also worked well for the renal arteries. However, the renal tissue surrounding the vessels has very different properties than the muscle tissue of the heart. This lead to severe diffusion of the iodine contrast agent out of the vessels and into the surrounding tissue. In Fig. 5.5, two projection images from a CT performed of a porcine kidney are shown. Fig. 5.5a shows the very first projection of the CT scan while Fig. 5.5b shows the projection after a turning of 180°. It is clearly visible that the contrast agent has diffused out of the vessels. The CT scan was aborted after this finding since artifacts in the reconstructed images will arise if the sample does not stay unchanged during the scan. Therefore, a solution for the diffusion of the contrast agent during the CT scan had to be found. After the first CT scan, several attempts were made to reduce the diffusion of the contrast agent into the tissue. A first attempt was to mix the contrast agent with liquid agarose gel and let it harden inside the vessels of the kidney. For this, 0.75 g of agarose gel (Biozym Agarose) were mixed into 50 ml of water and heated until

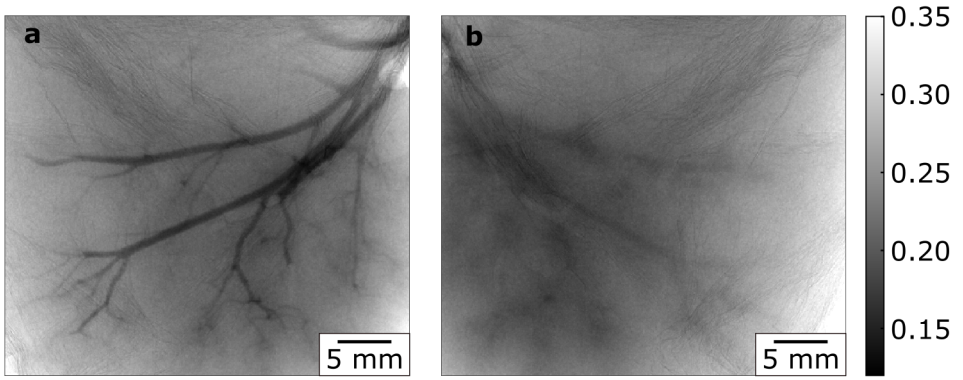

Figure 5.5: Projection images of porcine kidney with contrast agent at 0° and 180°: **a** At the beginning of the CT scan, the contrast agent is only located in the vessels of the kidney, giving a good contrast between vessels and tissue; **b** After half of the CT scan, at an angle of 180°, the contrast agent has diffused from the vessels into the surrounding tissue. The contrast between vessels and surrounding tissue is almost completely lost. The gray scales of the images show the relative intensity of the X-ray beam.

a clear fluid was obtained. 16 ml of iodine contrast agent (Imeron 400) were heated to the same temperature and then mixed into agarose liquid. The mixture was cooled to 45 °C before injecting it into the kidney to prevent denaturation of tissue. A CT scan of this kidney showed that the iodine concentration in the mixture was too low to get good results (iodine concentration in final solution: $\sim 97\,\mathrm{mg/ml}$). A repetition of the experiment with a higher iodine concentration ($\sim 150\,\mathrm{mg/ml}$) showed that the diffusion of the contrast agent was slowed down, but since the gel did not completely harden, there was still some diffusion. A second attempt involved cooling the kidney tissue before the iodine contrast agent injection and during the CT scans to minimize diffusion. Since the viscosity of the contrast agent is highly dependent on temperature, it was expected that it should stay in place when hitting the cool vessel walls. To enable a good injection even into smaller vessels the contrast agent was not cooled before injection but kept at room temperature. This approach gave good results (cf. Fig. 5.6) although there was still some diffusion to the end of the CT scan (cf. Fig. 5.6c).

To additionally minimize image artifacts through the diffusion of the contrast agent, several adaptions were made to reduce the scan time for a CT of the kidney. Usually, when performing a measurement at the MuCLS, a flux threshold is set and the measurement automatically halts if the X-ray flux falls below this threshold. The flux is thereby checked by a scintillation counter located in the front of the first experimental hutch. Yet, the readout of the scintillation counter and comparison with threshold adds overhead to each projection of the CT scan and thus prolongs the scan time. Therefore, the scintillation counter was completely disabled for the CT scans to reduce the overhead time in a first step. Another time limiting factor was the time needed for the detector communication and saving of the acquired images. While the time for detector communication cannot be influenced, the time needed for saving of the images could be reduced. The used Dexela flat-panel detector has a preinstalled setting for

asynchronous saving of the images to the hard drive.

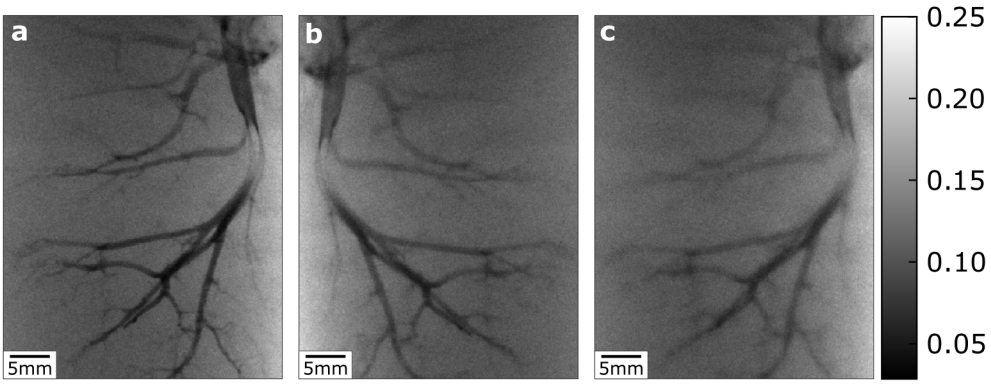

Figure 5.6: Projection images of a cooled porcine kidney with contrast agent at 0°, 180° and 360°: **a** At the beginning of the CT scan, the contrast agent is only located in the vessels of the kidney, giving a good contrast between vessels and tissue; **b** After half of the CT scan, at an angle of 180°, the contrast agent is still mainly in the vessels. Some of the very small vessels have lost contrast agent into the surrounding tissue; **c** Even at the end of the CT scan, after a full turn of 360°, the contrast agent has barely diffused out of the vessels. The contrast between vessels and surrounding tissue is still good enough to be able to fully reconstruct the CT scan. The gray scales of the images show the relative intensity of the X-ray beam.

When using this setting, the detector saves the acquired data in its temporary storage and continues acquiring images while simultaneously saving the previously acquired images. As the acquisition of images only takes place when the kidney does not move, the rotation speed of the sample stage also had an influence on the scan time. To further optimize the scan time, the rotation speed was increased by a factor of five from 2000 steps/s to 10000 steps/s. By implementing the three adaptions described above, the scan time for a CT scan of 1500 projections and 0.2 s per projection was reduced from about 35 min to about 20 min.

In addition to the steps mentioned above, further optimization was made to the macro used to acquire the CT scan. Usually, the X-ray flux of the X-ray source varies over time. To account for this change in flux, flatfield images are acquired at regular intervals during the CT scan. However, since the sample has to be driven out of the beam before and back into the beam after the flatfield acquisition, this prolongs the scan time. In order to reduce the scan time further and to prevent possible shifts of the sample inside the sample container, the macro was changed such that flatfield images were only acquired at the beginning and at the end of the CT scan. This adaption further reduces the scan time to about 15 min for a scan with 1500 projections and an acquisition time of 0.2 s per projection.

Reducing the diffusion of the contrast agent and the scan time was crucial for the success of the KES performed with two CT scans at different mean X-ray energies. In order to eliminate all surrounding tissues and the kidney stone containing calcium in the KES, the scans have to be perfectly aligned. Therefore, the kidney has to stay in

the same position for both subsequent scans, and a second injection of contrast agent between the scans is not possible. Even without any user intervention, there was some movement of the kidney stone relative to its surroundings in the first scans so that the subtraction image contained artifacts as shown in Fig. 5.7a. Since the movement took place inside the sample, this could not be corrected in post-processing. To ensure a stable position of the kidney and the kidney stone inside the sample container, a sample holder was constructed from thermoplastic (Polymorph, Polyshape, UK) to perfectly hold the kidney in place (cf. Fig. 5.7b).

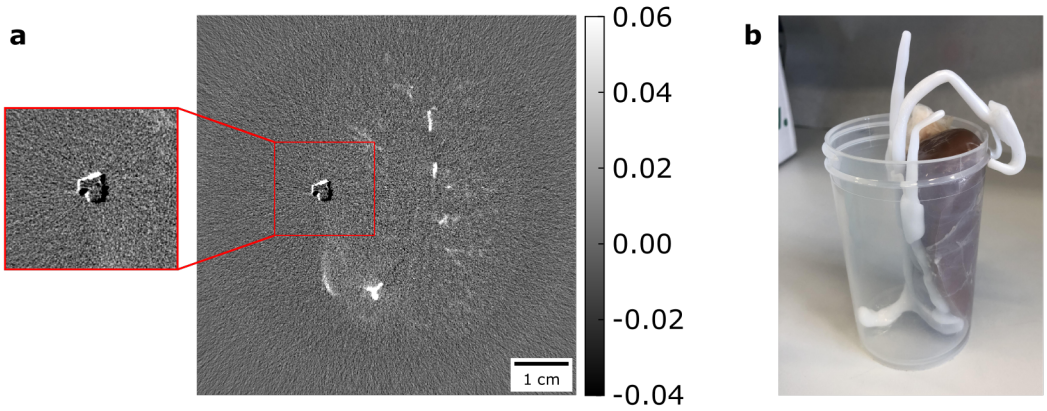

Figure 5.7: **a** KES CT slice with artifacts arising from misalignment of two subtracted scans: the edges of the kidney stone are still visible while the edges of the tissue and of the sample container are not visible. This suggests that the kidney stone moved relatively to its surroundings; **b** Photography of the sample holder built from thermoplastic to hold the kidney and the kidney stone in place during the CT scans and ensure alignment for successful subtraction.

5.2.3 Experimental details

To demonstrate the feasibility of the proposed KES CT technique, two CT scans of an excised porcine kidney together with a kidney stone were performed. One scan was done with the iodine filter in the beam while the other was performed with the full spectrum of the MuCLS. At the time of the measurements, the MuCLS produced a flux of 1.3×10^{10} photons/s. Each scan had 1000 equally-spaced projections over 360 degrees and an exposure time of 44 ms per projection. Each scan therefore had a total exposure time of 44 s. Together with the time needed for the movement of the sample stage and for detector communication, the total scan time added up to 10 min per scan. The kidney was set into a plastic beaker glass and undiluted iodine-based contrast agent (IMERON 400 MCT, Bracco Imaging, Germany) was injected into the renal arteries. The kidney was refrigerated prior to the measurements and placed in cold water during the experiment to slow down the diffusion of the iodine-based contrast agent out of the blood vessels into the surrounding tissue. The human kidney stone, made of calcium oxalate (90% whewellite and 10% weddellite), was placed into the skin surrounding the kidney (cf. Fig. 5.8a). The data was acquired with a flat-panel detector (Dexela 1512,

PerkinElmer, Inc., USA) with a Gd_2O_2S scintillator and a pixel size of $74.8 \times 74.8\,\mu m^2$. Due the ICS's beam divergence, the CT scans have an effective pixel size of $70 \times 70\,\mu m^2$. The tomographic reconstruction was performed with a SIR algorithm [Fessler, 2000]. The CT scans were subtracted slicewise after the reconstruction. For the KES CT volume, the iodine filtered scan was subtracted from the unfiltered scan. To visualize the kidney stone without blood vessels, i.e., to calculate an inverse KES CT volume highlighting calcium, the unfiltered CT scan was subtracted from the iodine filtered scan, which was multiplied with an energy correction coefficient. This coefficient was calculated by the ratio of the mean energies of the scans to the power of three to correct for the energy dependence of the photoelectric effect. The kinetic energy released per unit mass in air (air kerma) was calculated to 0.16 mGy/s for the unfiltered CT scan and 0.07 mGy/s for the filtered scan and hence is 10.12 mGy for the total measurement time of 88 s. Using the conversion coefficients for air kerma and effective dose for kidney tissue [Zankl, 1997], the total effective dose for both scans combined is 2.67 mSv. The

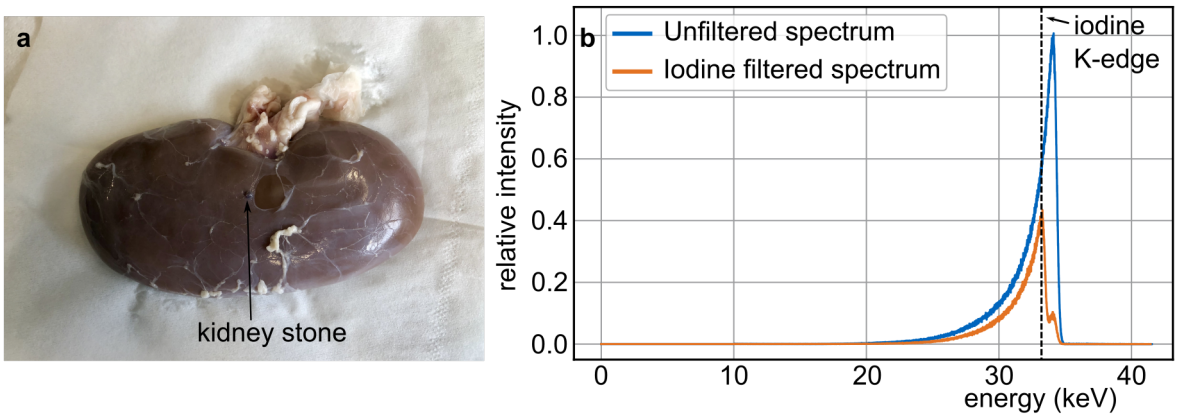

Figure 5.8: **a** Photography of the porcine kidney used in the experiment with a human kidney stone placed on the outside of it; **b** Plot showing the unfiltered and the iodine filtered spectrum of the MuCLS and the iodine K-edge. The unfiltered spectrum has its peak at 33.7 keV. Figure adapted from [Kulpe, 2019].

X-ray spectra used for the experiments are shown in Fig. 5.8b. The MuCLS was tuned to a peak energy of 33.69 keV such that the mean energy of the unfiltered spectrum was 33.18 keV, just above the K-edge of iodine. By filtering the spectrum, the high energy part of the spectrum above the K-edge was absorbed so that only 3% of the intensity of this high energy part of the spectrum remained. The filtered spectrum then had a mean energy of 32.59 keV. The energy separation of the two scans is therefore 0.59 keV. This energy separation is considered ideal for the experiment as Sarnelli et al. [Sarnelli, 2006] showed that a smaller energy separation is beneficial for the contrast in the KES image. For the experiments, a solid iodine filter was used, which was made of an iodine-based contrast agent (Ultravist 370, Bayer Schering Pharma AG, Germany) embedded into a PVP polymer-matrix. The effective iodine thickness of the filter is $\sim 190\,\mu m$. It was mounted on a motorized filter wheel (FRM40, OWIS GmbH, Staufen, Germany), which allows moving the filter in or out of the beam on a sub-second time scale.

5.2.4 Results

In Fig. 5.9, X-ray projection images of both the unfiltered and filtered CT scan of a porcine kidney together with a kidney stone are presented. The kidney can be seen from the front (0°), side (90°) and back view (180°). In the unfiltered images, the renal arteries filled with iodine contrast medium are clearly visible. The kidney stone, indicated by the red arrow, absorbs similarly to the iodine in all projections which makes the differentiation of the two difficult. The absorption of the kidney stone was calculated exemplarily in the projection at 0° to 0.956 ± 0.006, the absorption of the iodine is 0.953 ± 0.004. With a single CT scan, the two materials cannot be separated. Therefore both clinical imaging and the KES CT method require a second scan.

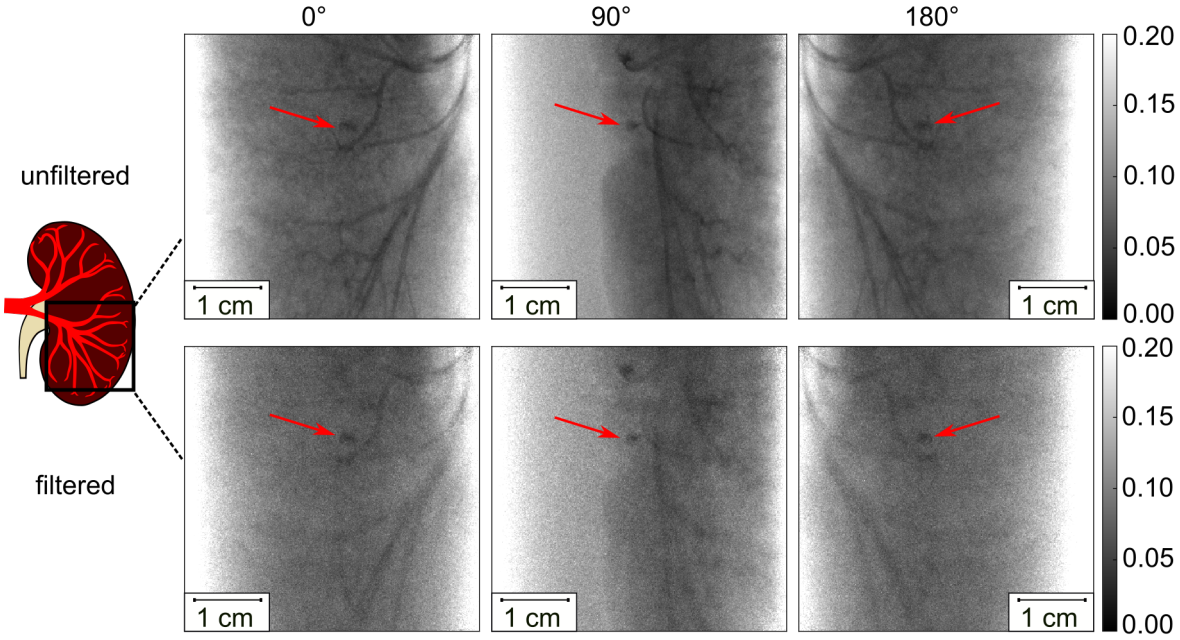

Figure 5.9: X-ray projection images of the filtered and unfiltered CT scans at projection angles 0°, 90° and 180°. The kidney stone is indicated by a red arrow. In the unfiltered projection images, the iodine filled blood vessels are clearly visible together with the kidney stone. In the filtered projection images, the X-ray attenuation of the iodine contrast agent is reduced, yet still the differentiation of iodine and the kidney stone is difficult. The gray scales of the projection images show the relative transmission of the X-ray beam. Figure from [Kulpe, 2019].

In contrast to clinical imaging, where the second scan is time-delayed in order to acquire scans with contrast agent and without it, the X-ray spectrum is filtered in our approach to change the mean energy for the second scan. In the filtered projection images, the X-ray absorption of the iodine contrast agent is reduced to 0.937 ± 0.007 due to the absence of the high energy photons above the K-edge in the spectrum. The absorption of the kidney stone in the filtered projection image is 0.9504 ± 0.007 and barely changes in comparison to the unfiltered images.

In Fig. 5.10, the reconstructed slices through the kidney and the calculated KES iodine and inverse KES calcium slices are presented. In both the unfiltered CT (Fig. 5.10a) and the filtered CT slice (Fig. 5.10b) the iodine filled blood vessels inside the kidney are visible. Additionally, the diffusion of the iodine into the tissue can be seen as slightly contrasted areas. The attenuation coefficient μ of the calcium-based kidney stone ($(0.2105 \pm 0.0151)\,1/\mathrm{mm}$), which is positioned on the surface of the kidney, is very similar to the attenuation of the contrast agent ($(0.2184 \pm 0.0100)\,1/\mathrm{mm}$). As the

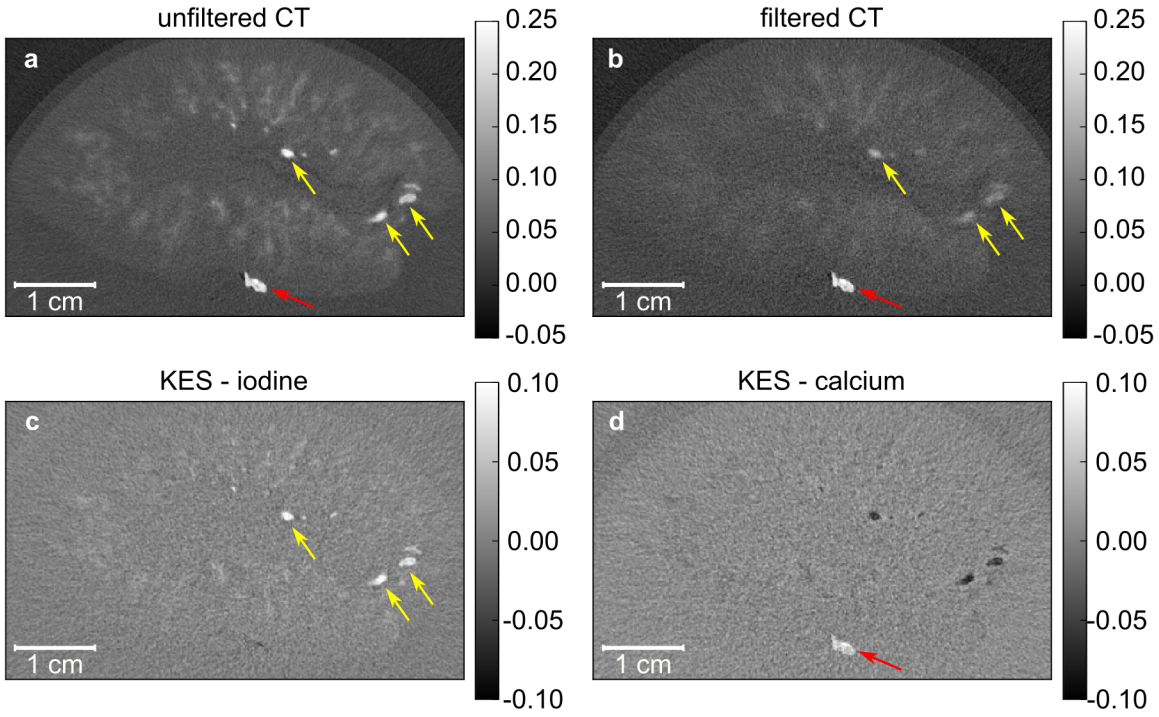

Figure 5.10: Reconstructed CT slices of porcine kidney with kidney stone (indicated by the red arrow) in transverse slice orientation (slice thickness: 70 µm). **a** Unfiltered CT slice, where both the blood vessels (indicated by the yellow arrows) and the kidney stone are visible; **b** Iodine filtered CT slice, where the attenuation of the iodine in the blood vessels is reduced, yet it is not possible to distinguish the two materials; **c** In the KES image only structures containing iodine contrast agent stay visible, the kidney stone is eliminated from the image; **d** When performing inverse KES, the iodine is inverted so that the kidney stone can be clearly identified. The gray scales of the unfiltered and filtered CT slices show the absorption values in 1/mm whilst the KES slices show the differences in absorption. Figure from [Kulpe, 2019].

kidney stone would be located inside the renal pelvis or ureter in a patient setting, the iodine contrast agent and the kidney stone would be expected in the same area. Similar CT values would make it impossible to separate both materials. After K-edge subtraction of the two slices (Fig. 5.10c), every material but iodine is eliminated from the resulting image so that the blood vessels can be clearly identified. In the inverse KES (as described in Ch. 5.2.3), the kidney stone becomes visible whilst the iodine filled blood vessels are inverted (Fig. 5.10d). The use of the KES subtraction method for CT allows for separation of iodine contrast agents and calcifications. This is especially

helpful in clinical diagnostics when looking for kidney stones in contrast enhanced CT.

The CT data can be segmented such that similar absorption values can be separated from the surrounding structures. This was done for the unfiltered CT scan and the calculated KES iodine and inverse KES calcium scans and is presented in Fig. 5.11a–c, respectively. In the unfiltered CT scan in Fig. 5.11a, the attenuation values of iodine and calcium are very similar, so that they cannot be separated by a simple histogram-based segmentation. In the KES iodine image in Fig. 5.11b, the blood vessels can be clearly identified. In Fig. 5.11c, solely the kidney stone is visible. Thus, also in the segmentation of the CT data, the KES method helps to distinguish blood vessels and calcifications, such as kidney stones.

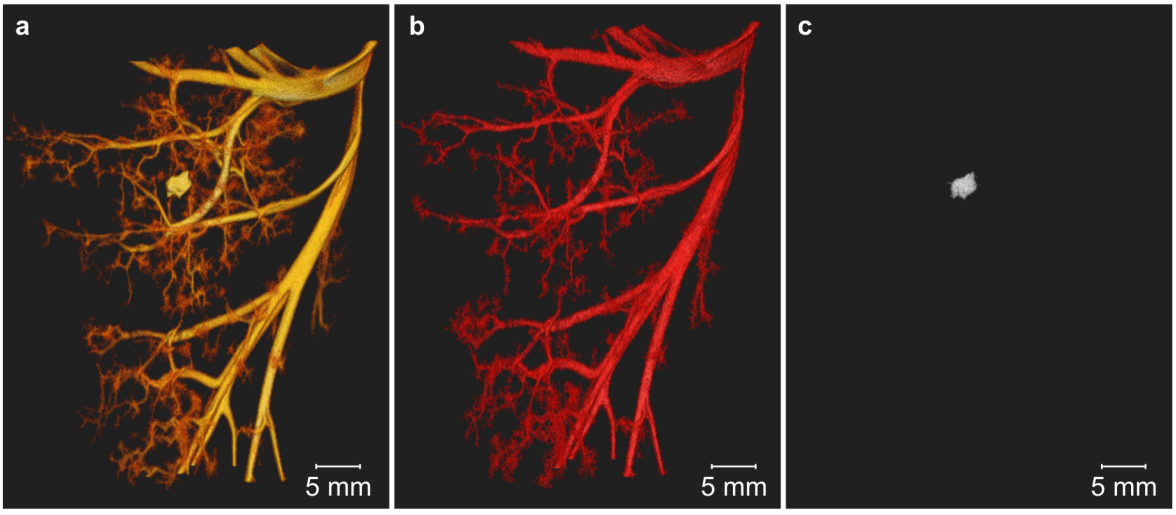

Figure 5.11: 3D visualization of segmented CT data to visualize solely the hyperdense structures. **a** The blood vessels and kidney stone were segmented from the unfiltered CT scan. The differentiation of the two materials is not possible; **b** The blood vessels were segmented from the KES data, in which the kidney stone is not visible; **c** By performing inverse KES, the calcium within the kidney stone becomes visible again whilst the iodine-filled blood vessels are subtracted from the image. Figure from [Kulpe, 2019].

5.2.5 Discussion

The results of this proof-of-principle experiment demonstrate that KES CT is feasible using the quasi-monochromatic spectrum at the MuCLS and a filter-based K-edge subtraction method. Taking two CT scans at different mean energies, it was possible to calculate images that separate iodine contrast agent and calcium, a commonly faced issue in clinical imaging. However, currently the scan time of the CT obtained at MuCLS is not compatible with the needs in a clinical routine. A full body scan can be performed in down to 5 s at a clinical CT device [Kalender, 2006]. At the MuCLS, the scan was performed at a multi-purpose research setup, which is not optimized for one specific application. Therefore, the scan time is currently around 10 min but could be further reduced by optimizing the detector communication, using a larger detector

pixel size and allowing for a continuous movement of the sample stage. This would provide the basis for further experiments, such as *in vivo* small animal KES CT. With additional development of the imaging setup and the image processing algorithms, KES imaging can provide further advantages for CT imaging. Monochromatic imaging allows for material decomposition at a higher accuracy than state-of-the-art clinical imaging [Dilmanian, 1997]. In addition, the absolute concentration of the contrast agent [Le Duc, 2000; Elleaume, 2002; Suhonen, 2008] can be determined in KES CT as well as the electron density of the material after performing a dual-energy approach [Torikoshi, 2001; Torikoshi, 2003; Tsunoo, 2008]. In most KES CT synchrotron studies, the clinical applicability was limited by the dose applied to the specimen, with dose levels between 7 mGy [Tsunoo, 2008] and 9 Gy (skin entry dose) [Schültke, 2011]. Yet, KES imaging at synchrotrons has been demonstrated with clinically acceptable dose levels in transvenous coronary angiography [Elleaume, 2002] and in *in vivo* KES CT [Strengell, 2014]. The effective dose in this experiment of 2.67 mSv was far below the dose applied in clinical dual energy CT, where dose levels of $5 - 12$ mGy (CTDI) per scan are achieved [Qu, 2015; Henzler, 2012; Jepperson, 2014; Chaytor, 2016]. Also, the effective dose level in this experiment was lower than effective doses usually applied in renal angiographic CT being around 5 mSv [Cho, 2012]. Here however, only a single organ was imaged.

In conclusion, it has been shown that KES CT is feasible at a compact synchrotron X-ray source, which is going to provide benefits for contrast enhanced 3D imaging in a pre-clinical setting. KES CT allows for a discrimination of iodine and calcium, which will be of special interest in various clinical situations like kidney stones, atherosclerosis and bone imaging.

6 Dynamic K-edge subtraction imaging

While the static KES experiments showed good results and confirmed the advantages of monochromatic subtraction imaging, the reality is that there is seldom a static situation in clinical imaging. Often the image quality is impaired by motion artifacts arising from patient movement or simply from the movement of the organ of interest. Many efforts are made to reduce motion artifacts in the clinical routine, such as the use of an electrocardiogram or an external ventilator to trigger the image acquisition. Additionally, post-processing algorithms are implemented that correct distortions or that correlate structures of two images used for temporal subtraction to one another. Several KES studies at synchrotrons have shown that this imaging method does not need special image acquisition protocols or post-processing algorithms but provides subtraction images with hardly any or no artifacts. This makes KES more suitable for the imaging of moving organs than conventional temporal subtraction techniques. The experiments performed for this thesis aim at evaluating if dynamic KES imaging at an ICS provides the same benefits as at synchrotrons.

To enable dynamic KES imaging at the MuCLS, several developments were necessary, such as the construction of a mechanically driven iodine filter and the possibility to externally trigger the detector. This chapter gives an overview of the development steps and the final dynamic KES fluoroscopy experiments performed at the MuCLS.

6.1 Triggering of the detector

In order to enable fast KES imaging and thus the observation of dynamically changing samples, a solid iodine filter was developed (as mentioned in Ch. 4.2). It was mounted onto an opto-mechanical component, enabling the movement of the filter in and out of the X-ray beam in a sub-second time range. For this, a custom-designed filter holder, produced in-house by additive manufacturing, was mounted on a stepper motor (FRM40, OWIS GmbH, Staufen, Germany). The filter holder has openings that are alternately empty and filled with an iodine filter that almost completely absorbs the part of the spectrum lying above the iodine K-absorption edge. On the outer edge of the filter holder there are transparent and opaque segments corresponding to the inner openings. These pass through a fork-like light barrier (PM-L45-P-C3, Panasonic Industrial Devices SUNX Co.,Ltd., Aichi, Japan). This way, transistor-transistor logic (TTL) trigger pulses are generated. These match the time period during which the complete beam passes through one of the inner openings unobstructed. By enabling external triggering of the detector, it will only acquire images when the beam is completely inside an opening of the filter holder. This allows to acquire subsequent images with the whole X-ray spectrum and the filtered spectrum with identical acquisition

time. The acquisition time is limited by the time the beam needs to vertically pass through the opening of the filter holder, which is determined by the rotation speed of the filter wheel and the size of the opening. The filter wheel can rotate with up to $2600°/s = 7.22$ rotations/s. Since the filter holder has four openings, thus allowing for four images per rotation, the maximum imaging rate of the filter wheel is $4 \times 7.22\,1/s \approx 29$ Hz.

The experimental setup for dynamic KES can be seen in Fig. 6.1. The filter wheel is placed in the first experimental endstation at a distance of 3.5 m from the source interaction point in order to filter the beam when its diameter is sufficiently small and to minimize the influence of the iodine fluorescence on the images. The quasi-monochromatic X-ray beam produced by the CLS enters the experimental setup in the first experimental endstation and hits the motorized filter wheel. While the X-ray beam passes through the filter opening, the light barrier is interrupted by the outer edge of the filter holder and produces a 4.77 V TTL-high signal which is passed on to the X-ray detector in the second experimental endstation. There the X-ray beam passes through the sample and is detected by the detector with an acquisition time determined by the filter wheel and the light barrier. During the acquisition, contrast agent is injected into the sample with a remotely driven syringe (described in more detail in Ch. 6.6.1).

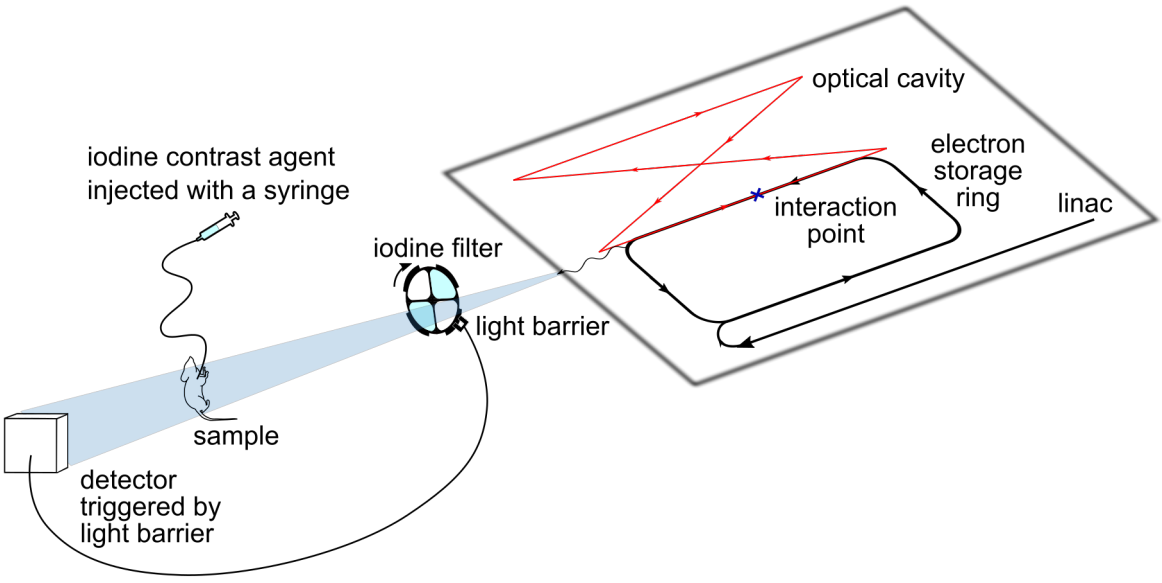

Figure 6.1: Experimental setup for dynamic KES at the MuCLS: The quasi-monochromatic X-ray beam is produced in the compact synchrotron source by inverse Compton scattering of relativistic electrons and laser photons. Travelling to the experiment, the X-ray beam passes through the rotating filter wheel whose ports are alternately equipped with an iodine filter or remain empty. While a port of the filter wheel is in the beam, the outer segment of the filter holder passes through a light barrier, which gates the image acquisition. The (un)filtered beam then penetrates the sample and falls onto the detector. During imaging, iodine contrast agent is injected into a sample with a remotely driven syringe. Figure from [Kulpe, 2020a].

6.2 Design of the filter holder and wheel

At first, the commercially available filter wheel FRM40 by Owis GmbH (Staufen, Germany) was used to trigger the beam. A schematic of this filter wheel and a photography of it mounted in the setup are shown in Fig. 6.2. The filter holder has a diameter of 80 mm with openings with 25 mm in diameter. The filter holder is driven by a stepper motor with a gearwheel drive of 2 : 1, 200 steps per motor rotation and a maximum rotation speed of 2600°/s. The motor has no maximum rotation angle limiting the movement of the filter wheel. The filter wheel is placed in the very front of the first experimental hutch so that the X-ray beam is still sufficiently small, allowing for a larger angle of rotation during which the beam is not obstructed. The size of the openings defines the usable angle to 18° per image. Since the wheel has 4 openings, $90° - 18° = 72°$ of rotation between two images cannot be used. This leads to a significant time lack between two acquired images and can therefore lead to artifacts in the calculated KES image. For the initial goal of acquiring images at a rate of 10 Hz, i.e., with a rotation speed of $2.5 \times 360° = 900°$/s, the acquisition time was limited to 20 ms with a time difference of 80 ms between the images.

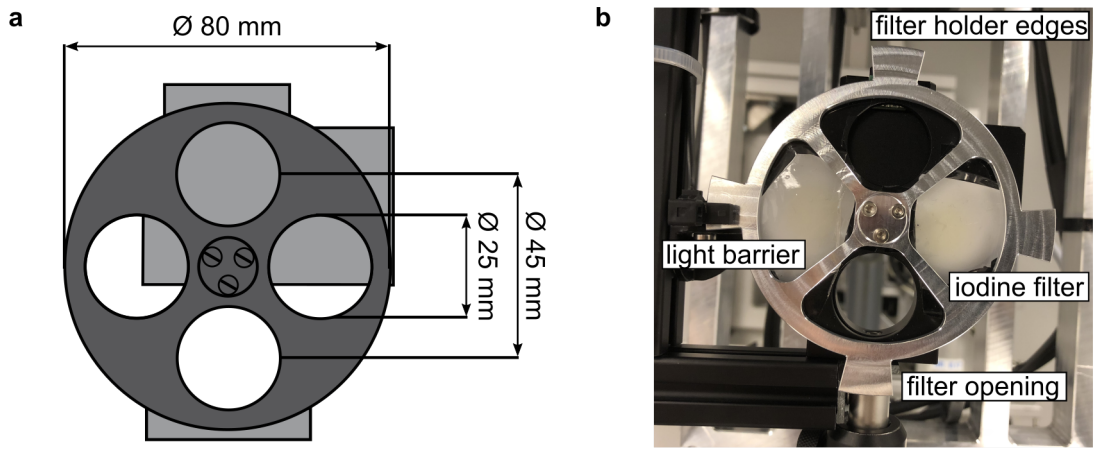

Figure 6.2: First filter wheel used at the MuCLS. **a** Schematic showing the dimensions of the filter wheel; **b** Photograph of the filter wheel with mounted iodine filters and adaptive plate with outer edges structured according to the rotation angle for which the complete beam passes through the opening of the filter wheel.

Therefore a second filter wheel was constructed. It was made of only the stepper motor of the FRM40 filter wheel mentioned above together with a custom-designed filter holder produced in-house at TUM. Fig. 6.3a shows the basis of the filter wheel on which the filter holder was mounted. The basis has a stepper motor with the same characteristics as in the original FRM40 filter wheel by Owis, but the filter holder is cut off, leaving only a small center piece to allow for the mounting and the exchange of a custom filter holder. Fig. 6.3b shows the assembled filter wheel with the filter wheel basis and the custom-built filter holder. In the final setup, two openings of the filter holder are filled with iodine filters specifically made for them according to the protocol

described in Ch. 4.2. The outer edges of the filter holder are constructed such that the X-ray beam is completely inside the opening of the filter wheel when these trigger the image acquisition. Fig. 6.3c shows how the outer edges are designed. First, the filter wheel is set into the beam at the position where it is also going to be placed during the dynamic KES experiment. This is crucial since the X-ray beam's size increases with greater distance from the source interaction point and therefore the angular distance for which the beam is inside the filter opening will decrease. The filter wheel is imaged in the two angular positions where the X-ray beam just hits the edge of the opening on the left and the right, respectively. The angular distance between these two positions is then used for the construction of the triggering mechanism. As the edges of the filter holder pass through the light barrier during the experiment, the light barrier will only give a signal when the beam is in the opening. This new filter holder construction significantly increased the usable angle for image acquisition from 18° to 60°. For an imaging rate of 10 Hz this now leads to an acquisition time of 66.7 ms with a time difference of 33.3 ms between the images.

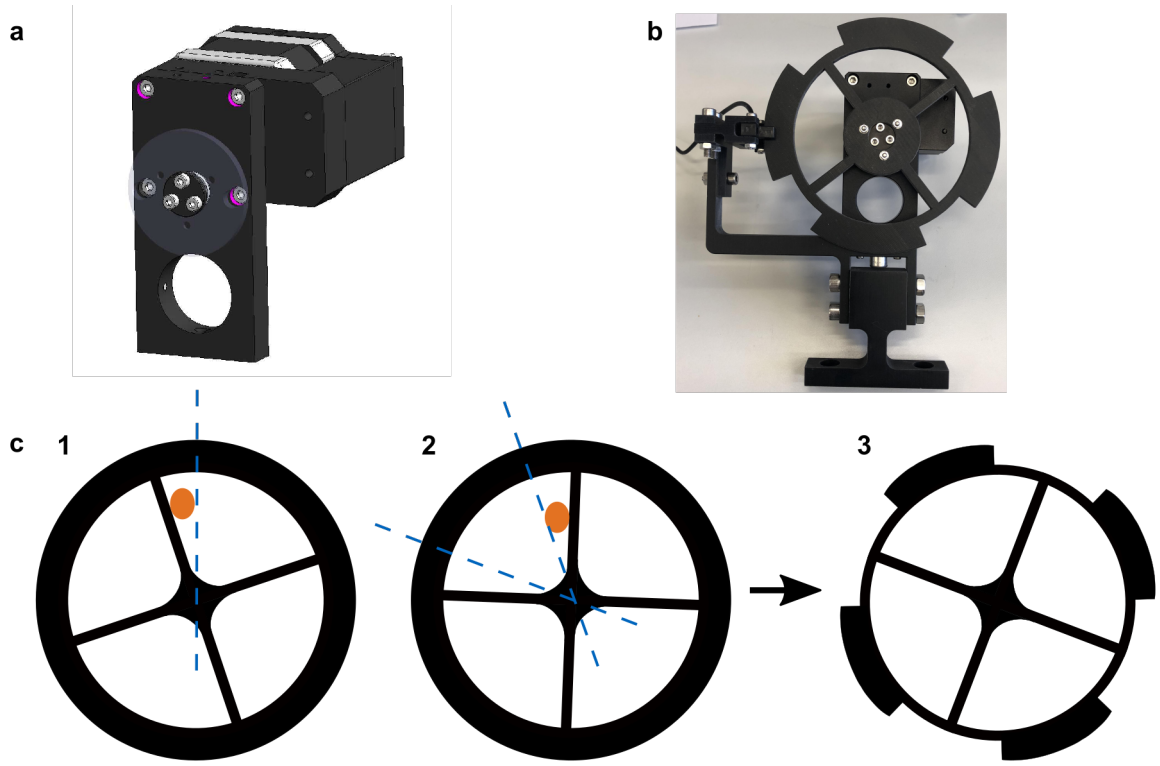

Figure 6.3: Second filter wheel used at the MuCLS. **a** Schematic showing the basis of the second filter wheel; **b** Photograph of the filter wheel with mounted filter holder with outer edges structured according to the rotation angle for which the beam passes through the opening of the filter wheel; **c** Schematic showing the construction of the filter holder and the structured outer edge. The orange spot resembles the X-ray beam while the blue lines indicate the angular positions at which the beam completely passes through the opening of the filter wheel.

6.3 Time limitation of Pilatus detector

The second experimental endstation is equipped with the Pilatus 200k photon-counting detector (Dectris Ltd., Baden, Switzerland). Thanks to the internal electronics it can be easily triggered using an external trigger signal. However, the 1mm thick silicon sensor provides a detection efficiency of below 20% for the 33 keV spectrum. In clinical angiography, images are acquired with an imaging rate of up to 30 Hz. However, the initial goal here was to obtain images with a rate of 10 Hz. Since the detector acquisition time is linked to the rotation speed of the filter wheel, this is equal to a rotation speed of 900°/s. In order to determine the feasibility of dynamic KES at the MuCLS, the first experiments were performed using the first filter wheel and the Pilatus detector.

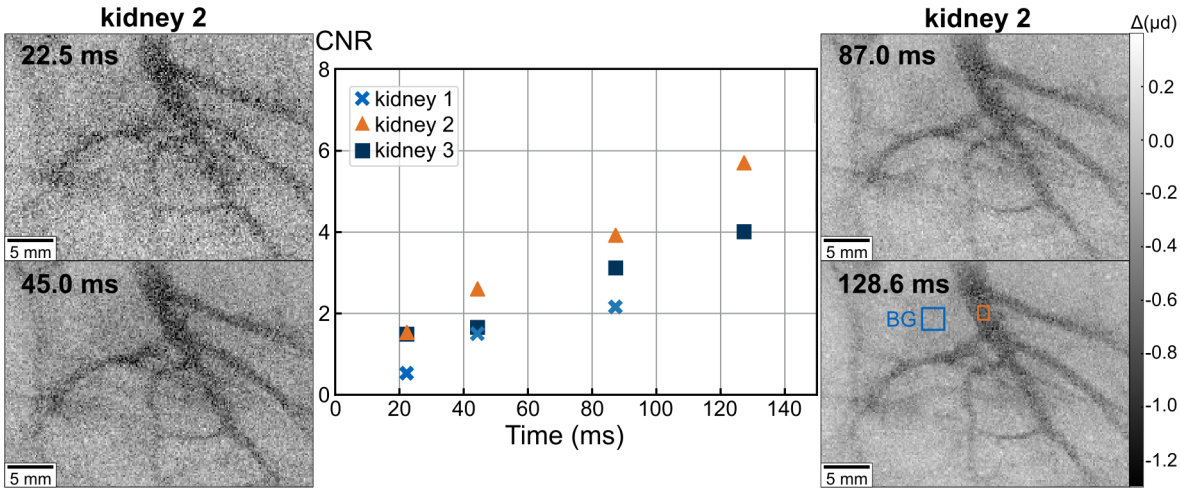

Figure 6.4: Imaging series of iodinated blood vessels with different acquisition times. With decreasing acquisition time, the noise level in the image increases and reduces the visibility of the blood vessels. The CNR values were calculated between the vessels (marked by the orange square) and the background region (marked by the blue square). For all three kidneys the CNR is proportional to the square root of the acquisition time.

To evaluate the development of the image quality and noise in the KES images in dependence of the acquisition time, imaging series of three different kidneys were performed. For this, unfiltered and iodine-filtered X-ray images of blood vessels filled with iodinated contrast agent were acquired with acquisition times between 22.5 ms (i.e., an imaging rate of 800°/s or 8.9 Hz) and 128.6 ms (i.e., an imaging rate of 140°/s or 1.6 Hz). The images were acquired using the first version of the filter wheel to trigger the Pilatus detector and thereby subsequently acquire non-filtered and iodine-filtered images with identical acquisition times. The images were then flatfield corrected and KES images were calculated according to the scheme described in Ch. 4.1. Fig. 6.4 shows the imaging series performed on the vessels of one of the kidneys (kidney 2). While the vessel structure is clearly visible with longer acquisition times, their complex structure is difficult to identify with short acquisition times. To assess the image quality, thus the visibility of the iodinated blood vessels over the background, a CNR

analysis was performed. The CNR values were calculated between the blood vessels and background tissue versus the noise in a larger background region (ROIs are marked with orange and blue squares in the image with 128.6 ms acquisition time of Fig. 6.4). Fig. 6.4 shows the development of the CNR values for different acquisition times for all three kidneys in the experiment. As expected, the CNR increases with increasing acquisition time because of the better photon statistics and thus lower noise levels of the images. However, the CNR values are still relatively low, which makes the identification of the blood vessels, especially for short acquisition times, very difficult. Since the goal is to acquire images with an imaging rate of 10 Hz, leading to an acquisition time of around 20 ms when using the first filter wheel, good image quality must also be obtained for very short measurement times.

6.4 Denoising of KES images

To reduce noise in the KES images, several denoising techniques were tested. These were applied to the calculated KES images presented in Ch. 6.3 in order to improve the visibility of the vessel structures. Again, a CNR analysis of the denoised images was performed in order to evaluate the performance of the different denoising techniques, namely dictionary denoising, bilateral filtering and total-variation (TV) denoising. Dictionary denoising is an algorithm that denoises images with the help of a dictionary of patches that are combined to reconstruct the image with less noise. This dictionary has to be built with the help of low-noise training data that should contain structures similar to the ones present in the noisy image. The algorithm then combines the patches to form the acquired image using a weighting kernel and a cost function to obtain an optimally denoised image [Elad, 2006; Mechlem, 2018]. The bilateral filter is a non-linear filter that preserves edges similar to the TV regulator and removes noise by spatial averaging. It is an effective image denoising technique, however the selection of the filter parameters is critical and affects the results significantly [Zhang, 2008]. The TV denoising evens out the variation between pixels using a kernel of defined size (in this case the kernel had a size of 7×7 pixels). However, it uses a regularizer which has the advantage that it preserves edges while simultaneously smoothing out noise in flat regions [Strong, 2003].

The results of the denoising algorithms are shown exemplarily in Fig. 6.5a for the 45 ms KES image of kidney 2, however the results for all other images are similar. Generally, all three algorithms reduce the noise and increase the visibility of the blood vessels significantly in comparison to the original image (Fig. 6.5a i). The dictionary denoising algorithm provides the best denoising results and clearly visualizes the vessel structures (cf. Fig. 6.5a ii). This algorithm was initially developed for the denoising of CT slices, which have a uniform noise level over the whole image slice. However, the noise level in projection images depends on the sample thickness, which will not be equal for the whole sample. Therefore, the algorithm does not work optimally and "patchy" structures appear in the background of the denoised image. Both the bilateral filtering (Fig. 6.5a iii) and the TV denoising (Fig. 6.5a iv) enhance the visibility of the

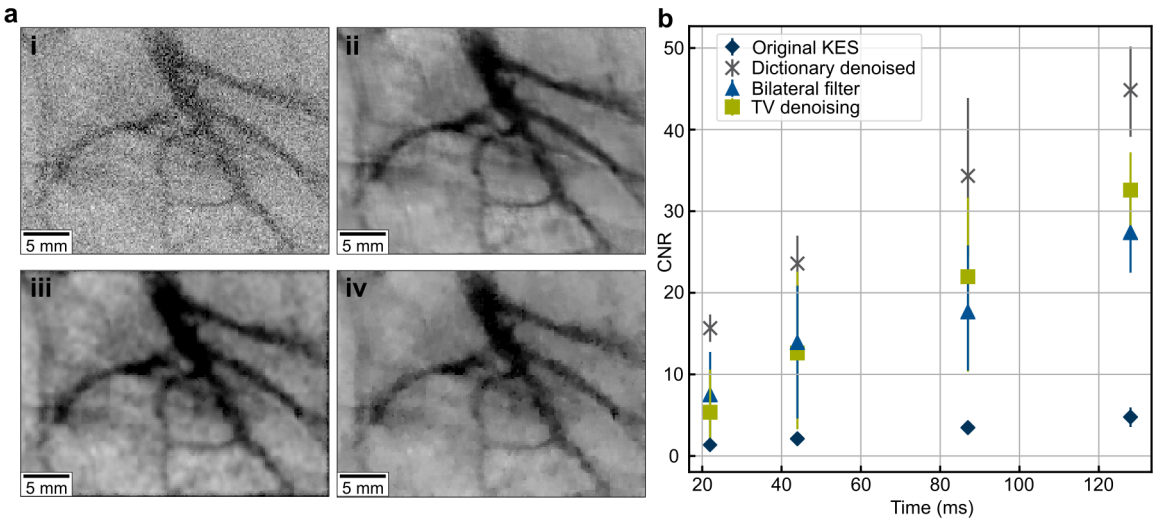

Figure 6.5: KES image denoised with different algorithms and their influence on image CNR. **a** KES images of kidney 2 with 44 ms exposure time: **i** original KES image, **ii** denoised with dictionary denoising algorithm, **iii** denoised with bilateral filtering and **iv** denoised with total variation denoising; **b** Plot showing the influence of the denoising algorithms on the CNR of the images. The CNR values were averaged over all three kidneys.

blood vessels while reducing noise. However, the background of the image is more homogeneous in the TV denoised image than in the image optimized with the bilateral filtering.

In Fig. 6.5b the average CNR values for all measured kidneys for different acquisition times are shown. Generally, the CNR values of the denoised images are significantly higher than the ones from the original data and increase with longer acquisition time. While the dictionary denoising algorithm shows the highest CNR values for all acquisition times, it comes with the disadvantage that it needs far more computation time and also sufficient training data to obtain good results. Finding low noise training data is difficult for imaging of dynamically changing samples and especially when imaging structures that are not as regular as blood vessels, such as the gastrointestinal tract. The bilateral filtering and TV denoising provide similar results for 22.5 ms and 45.0 ms acquisition times. Only when increasing the measurement time further, the TV denoising provides better CNR values than the bilateral filtering. Since the TV denoising produces images with improved visibility of the enhanced structures while smoothing the image background with relatively short computation time, this algorithm was chosen to denoise the KES images presented in Ch. 6.6.

6.5 First time-resolved KES imaging

The first time-resolved KES imaging at MuCLS was performed using the first filter wheel shown in Fig. 6.2. The filter was placed in the first experimental endstation. To simulate the injection of iodinated contrast agent into a blood vessel, contrast agent

was continuously injected into a plastic tube with a diameter of 1 mm. A phantom was constructed to simulate the injection of contrast agent into a blood vessel. It was made of a plastic container in which the plastic tube is fixed such that it builds a loop in the field of view (cf. Fig. 6.6a). A syringe filled with iodine contrast agent (Imeron 400 MCT, Bracco Imaging Deutschland GmbH, Konstanz, Germany) is placed into the plastic container from the top and fixed between the container and an experimental stage. When moving the stage downwards, the syringe is emptied into the plastic tube. A photograph of the sample in the second experimental endstation can be seen in Fig. 6.6b.

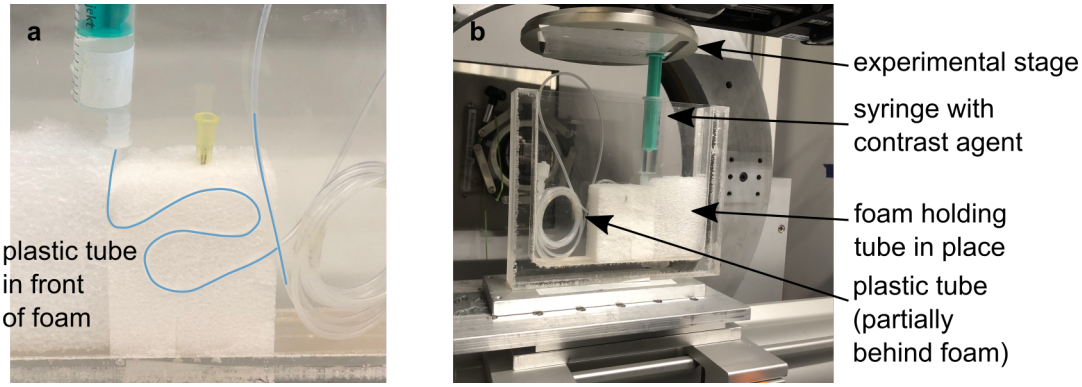

Figure 6.6: Phantom for the proof-of-principle dynamic KES experiments. **a** A tube resembling a blood vessel is fixed into a plastic container using foam. The part of the tube in front of the foam is highlighted in blue for better visibility. It is filled partially by contrast agent in the experiment; **b** The phantom is placed on the setup such that the syringe filled with iodine contrast agent is fixed between the container and the experimental stage. A downward movement of the stage empties the syringe into the plastic tube.

The images were acquired using the external trigger mode of the Pilatus 200k detector while the filter wheel rotated at a constant speed of 400°/s, i.e., an imaging rate of 4.44 Hz, leading to an acquisition time of 45 ms for both unfiltered and filtered images. Due to the limited angle for image acquisition, there was a time lag of 180 ms between two subsequently acquired images. The images were then flatfield corrected and post-processed according to the scheme described in Ch. 4.1.

The resulting KES images are presented in Fig. 6.7. The movement of the contrast agent over time can be clearly seen. However, at the edge of the liquid, bright motion artifacts are visible. They arise from the time difference between the two subtracted images. Since there is non-negligible movement of the contrast agent between two subsequently acquired images, there will be a great difference in position of the contrast agent inside the tube. This difference shows up as a bright area in the tube in the subtraction. The motion artifacts can be reduced by either reducing the injection speed of the contrast agent or increasing the acquisition angle, i.e., by increasing the size of the filter opening and thus reducing the time lag between the images. A medical procedure is usually limited by the radiation dose applied to the patient, which in turn limits the acquisition time. Therefore, the injection speed cannot be arbitrarily low and

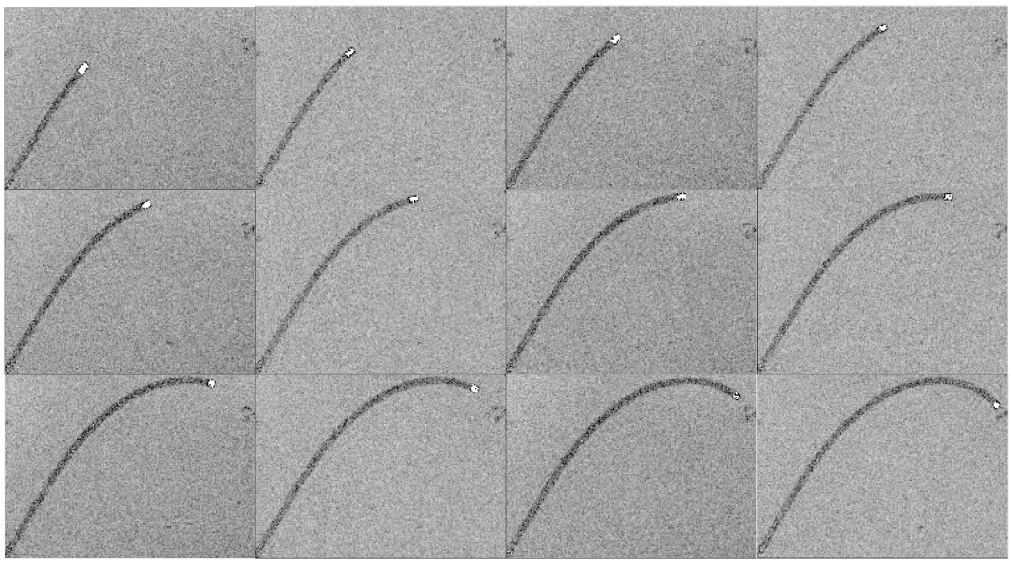

Figure 6.7: First dynamic KES images acquired at MuCLS. With increasing time scale (from left to right), the contrast agent travels through the plastic tube. However, since there is a time lag between the images, there are some artifacts arising at the edge of the liquid.

it is desired to reduce the time lag between the images. This will also reduce artifacts when performing *in vivo* imaging since the motion of the sample between images is small. With development of the second filter wheel, the imaging angle was increased from 18° to 60°, thus reducing the time lag between two acquired images as well as artifacts in the subtraction images as will be seen in the following chapter.

6.6 KES fluoroscopy of the gastrointestinal system

Contrast enhanced fluoroscopy is an X-ray based imaging technique that is commonly used for visualization of the gastrointestinal tract. Repetitive X-ray images are acquired before and after application of orally or rectally introduced contrast medium, and the diagnosis is made by evaluation of the spatial and temporal distribution of the contrast material. Upper gastrointestinal X-ray series illustrate the way of the contrast medium from the mouth down to the stomach. Movement of the larynx as well as the esophagus are an important physiological finding during the process of swallowing and, therefore, are of special interest in clinical fluoroscopy. Fluoroscopy is a study of moving body structures with a focus on physiological or pathological movements of the organs of the gastrointestinal system. However, subtraction imaging techniques cannot be used in clinical fluoroscopy of the gastrointestinal tract because of these physiological movements during the imaging procedure. In contrast, DSA is a clinically well-established fluoroscopy technique in interventional angiography, which allows for improved visualization of the blood vessels by using a temporal subtraction technique [Meijering, 1999]. In this procedure, a mask image without contrast agent is subtracted from all subsequent contrast enhanced images in order to remove background structures and

therefore improve the visibility of contrast enhanced vessels. However, artifacts from patient movement, breathing and cardiac motion may still have a negative impact on image quality [Tobis, 1983; Yamamoto, 2009]. Therefore, when imaging the gastrointestinal tract, conventional temporal subtraction cannot be used because the intestinal peristalsis, in addition to the movement of air in the intestine and the contractions of the esophagus, stomach, small bowel and colon will lead to artifacts that impair image quality and diagnostic accuracy [Winklhofer, 2016].

To improve the image quality in subtraction imaging, KES imaging, first proposed by B. Jacobson in 1953 [Jacobson, 1953], has been developed at synchrotron sources. In clinical temporal digital subtraction, the images are acquired at the same X-ray energy, using a polychromatic X-ray spectrum before and after injection of a contrast agent. In contrast, KES imaging exploits the sharp increase of the photoelectric absorption at the K-edge of the contrast agent to enhance the contrast between contrasted structures and surrounding tissue. Images are thereby acquired directly one after another or, with special setups, simultaneously. By logarithmically subtracting two images taken at X-ray energies bracketing the K-edge of the contrast agent, an image can be calculated that contains only the contrasted structures, without background signal, because the absorption signals of uncontrasted surrounding tissues barely differ in both images and cancel out in the subtraction [Jacobson, 1953; Sarnelli, 2004].

In the past, KES has widely been applied both in radiography [Rubenstein, 1986; Dix, 1995; Elleaume, 2000; Bertrand, 2005] and computed tomography [Dilmanian, 1997; Schültke, 2011; Cooper, 2012]. KES imaging at synchrotrons provides better image quality in comparison to temporal subtraction at conventional sources after intravenous injection of a contrast agent [Schültke, 2005]. Additionally, Elleaume et al. showed that KES is more suitable for moving organs than temporal subtraction [Elleaume, 2002]. KES fluoroscopy can be performed with minimal artifacts [Houk, 1979] and therefore enable subtraction imaging for applications where temporal subtraction is not useful.

Yet, the dependence of KES imaging on monochromatic X-rays, which are mainly provided at large scale synchrotron facilities, inhibits widespread application of this technique in clinical routine. This issue may be overcome with compact synchrotron X-ray sources, which are actively developed by multiple groups worldwide with the goal to provide brilliant X-rays in a laboratory frame [Huang, 1998; Jacquet, 2014; Bacci, 2016].

In past experiments, it has been shown that monochromatic angiography at the MuCLS produces images with improved CNR compared to images produced with a conventional X-ray spectrum [Eggl, 2017]. When expanding the procedure to KES angiography, it has been shown that a filter-based KES method at this laboratory source improves the visibility of small blood vessels that are overlaid by bone structures [Kulpe, 2018] and allows for the separation of calcium in kidney stones and iodine in computed tomography [Kulpe, 2019].

This chapter presents a filter-based KES fluoroscopy application and evaluates its performance compared to temporal subtraction at the MuCLS. For this, iodine contrast agent was injected into an *ex vivo* mouse while acquiring projection images with X-ray

spectra that were subsequently filtered and not filtered with an iodine filter. From the acquired images, KES and temporal subtraction images were calculated. At the same time, movement of the sample was simulated to demonstrate the appearance of motion artifacts commonly observed in *in vivo* temporal subtraction imaging. The results imply that KES allows for imaging with reduced or no artifacts, which would enable subtraction imaging of, e.g., the gastrointestinal tract in future medical applications. Note that part of this chapter draws text and figures directly from the publication: Kulpe et al., Dynamic K-edge Subtraction Fluoroscopy at a Compact Inverse-Compton Synchrotron X-ray Source. Scientific Reports 10, 9612 (2020) [Kulpe, 2020a].

6.6.1 Experimental setup

The sample and the detector are placed in the second experimental endstation to obtain a maximum field of view. The sample, in these experiments an *ex vivo* mouse, is placed at a source-to-sample distance of 15.6 m and a sample-to-detector distance of 0.8 m. During the image acquisition, iodine-based contrast agent (Imeron 400 MCT, Bracco Imaging Deutschland GmbH, Konstanz, Germany) with an iodine concentration of 200 mg/ml is injected through a tube into the abdomen of the mouse. The sample is subsequently imaged with the unfiltered and filtered X-ray beam obtained from the beam passing through the openings of the second filter wheel. Each image is taken with an exposure time of 66 ms. The Pilatus 200k photon-counting detector, with $172 \times 172\,\mu m^2$ pixel size and a 1000 µm thick silicon sensor, is triggered by the light barrier described earlier. It is operated in the "external enable" mode, i.e., the exposure time is as long as the external trigger pulse is active. This way, the exposure time is automatically adjusted to the optimum length for the chosen rotation speed of the filter wheel. Due to the slight cone beam, the effective pixel size in the sample plane is $164 \times 164\,\mu m^2$.

Syringe holder

To enable the injection of contrast agent with a constant flow, a syringe holder was designed that keeps a syringe filled with iodinated contrast agent in place and attaches it to a mechanically driven stage. Fig. 6.8a shows the CAD drawing of the syringe holder, where the inner part holds the syringe in a fixed position while the outer part slides onto the inner part and presses onto the plunger to empty the syringe. The holder is optimized for holding a syringe with 10 ml filling volume, however also smaller syringes can be placed into it. Fig. 6.8b shows the syringe holder fixed onto the linear sample stage. During the measurement, the stage applies pressure onto the outer part of the holder to inject a constant flow of contrast agent into the sample. The motorized linear translation delivers a constant flow of contrast agent of 0.05 ml/s to the sample.

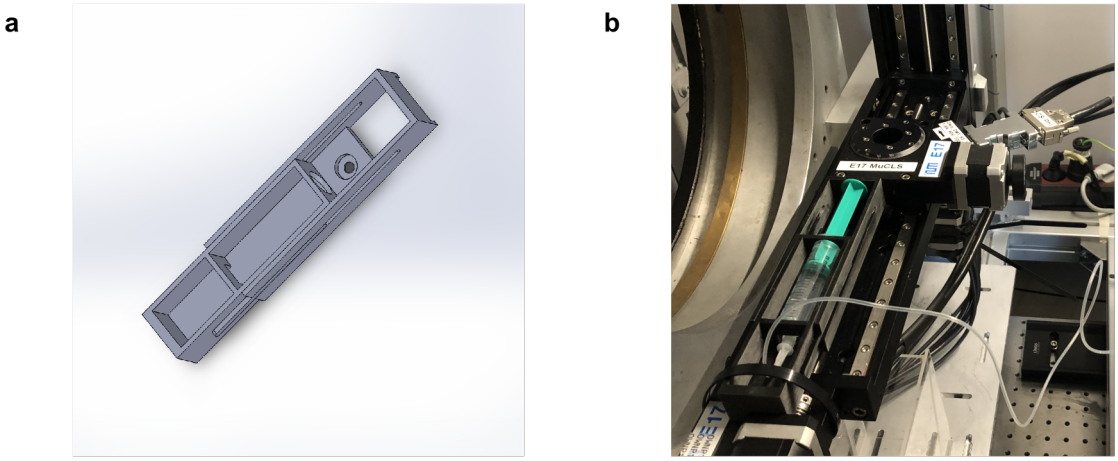

Figure 6.8: Syringe holder designed to ensure a constant injection of contrast agent. **a** CAD drawing of the syringe holder designed to keep the syringe firmly in place during the experiment; **b** Photography of the syringe holder in the experimental setup. The syringe holder is placed onto a linear translation stage that applies pressure to the syringe holder and ensures a constant injection of the contrast agent.

Sample

The dynamic KES experiment was performed on a euthanized mouse provided by the Animal Care Unit of the Klinikum rechts der Isar, TUM. It is euthanized in strict accordance to standard guidelines of an animal experiment proposal approved by the Institutional Animal Care and Use Committee of the Technical University of Munich. After the experiment, the organs are removed and further used according to the 3R principle (reduce, refine, replace).

Calculation of images

Both KES and temporal subtraction images were calculated from the acquired images. First, unfiltered and iodine-filtered images are dark current, flatfield and flux corrected. For the temporal subtraction, only the unfiltered images were used, since temporal subtraction uses images acquired with the same spectrum but before and after injection of contrast agent. Therefore, the first image acquired with the unfiltered spectrum was used as the mask image, logarithmised and then subtracted from all subsequent logarithmized images (compare Fig. 6.9). In contrast, in KES imaging two subsequent images with different mean energies are subtracted. However, since the used filter method does not automatically produce images with a mean energy below and above the iodine K-edge, some additional processing steps are needed as described in Ch. 4.1. With the processing shown in Fig. 6.9, two images can be calculated that have completely separated spectra, one with a spectrum above the K-edge and the other with a spectrum below the K-edge. Afterwards, the temporal subtraction and KES images were spatially denoised by applying a total-variation denoising algorithm using split-Bregman optimization on each image

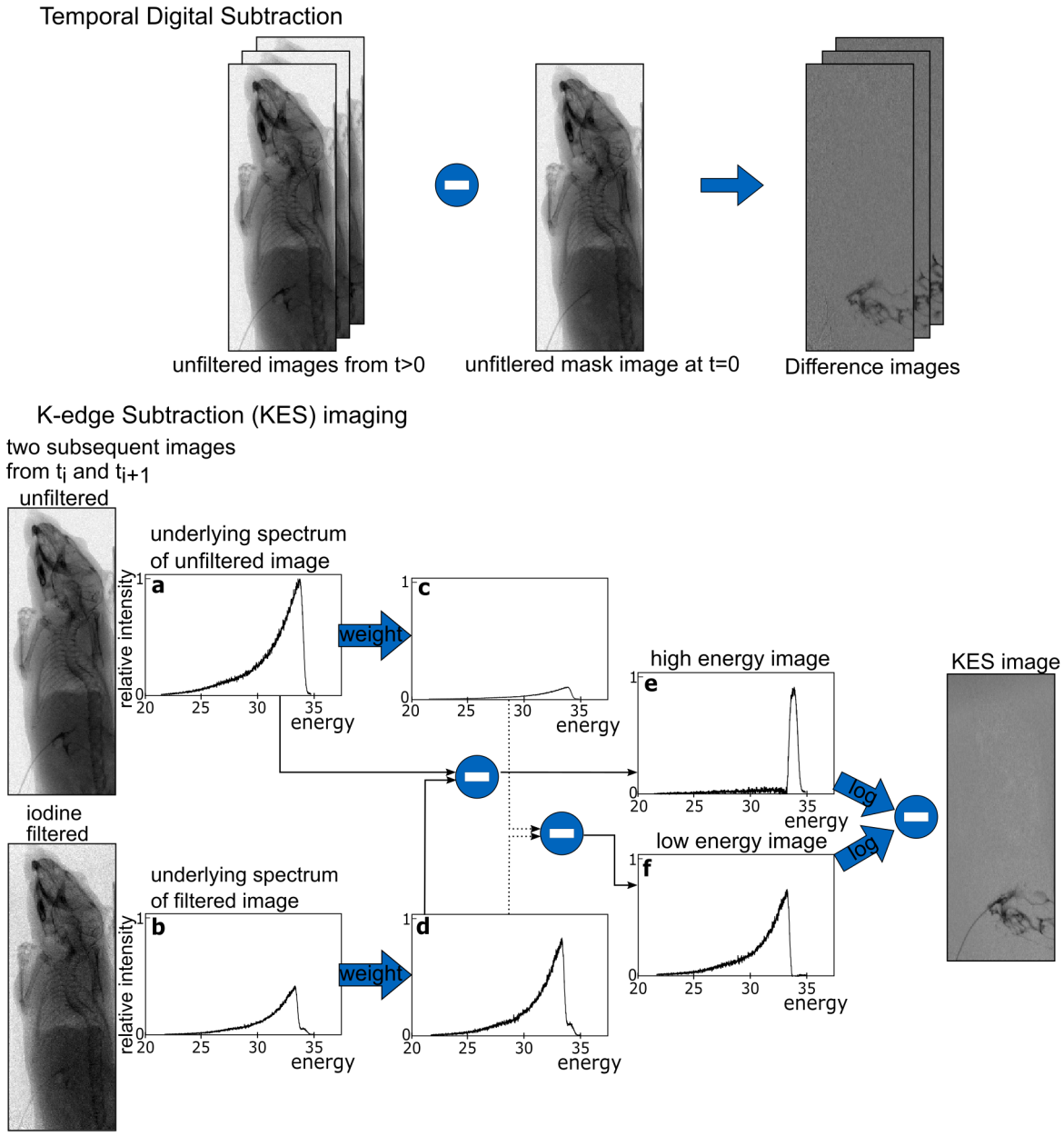

Figure 6.9: Image processing scheme for temporal subtraction and KES imaging. In temporal subtraction, the first unfiltered image is taken as a mask image and logarithmically subtracted from all following unfiltered images to generate the difference images. In KES, two subsequent unfiltered and iodine filtered images are subtracted. For these, two images with energies below and above the iodine K-edge need to be calculated. Subtracting the weighted iodine filtered image **d** from the unfiltered image **a**, produces a high energy image **e**, where only the part of the spectrum above the K-edge contributes to the image. The low energy image is calculated by weighting the unfiltered image **a** such that it fits to the remaining high energy peak in the weighted iodine filtered image **d**. By subtracting the weighted unfiltered image **c** from the weighted iodine filtered image **d**, one obtains the low energy image **f**. The high and low energy images are then logarithmized and subtracted to obtain the KES image. Figure from [Kulpe, 2020a].

and temporally denoised using a Gaussian filter on the temporal axis.

To simulate the movement of the sample through breathing and the movement of the organs inside the body, the images were shifted in horizontal direction. Along the time axis, these offsets followed a sinusoidal function with an amplitude of two pixels. The formula for the offsets Δx between two images was $\Delta x = 2 \cdot \sin(t)$. A breathing rate of 8 breaths/min was simulated. This rate is also used for the mechanical ventilation of *in vivo* imaging of mice [Murrie, 2016; Gradl, 2018], however only for very short periods of time ($< 1\,\text{min}$). Normally, faster breathing rates are used for *in vivo* imaging of small animals, which increases the problem of artifacts in the conventional temporal subtraction even more.

CNR analysis

Four ROIs were selected to evaluate how the CNR changes between the iodine contrast agent and bone structures over time. The used ROIs are highlighted in Fig. 6.11, where regions A1 and A2 are regions containing iodine contrast agent and B1 and B2 are the corresponding bone structures. The ROIs for iodine and bone were chosen to be $5 \times 3\,\text{pixels}$, while the larger background region had a size of $12 \times 8\,\text{pixels}$. The CNR is calculated against the noise in the background region BG according to Eq. 2.19 in Ch. 2.3.2. For each imaging modality, the weighted average $\overline{x}$ of the CNR values over time was calculated with

$$\overline{x} = \frac{\sum_{i=1}^{4} w_i \cdot x_i}{\sum_{i=1}^{4} w_i} \text{ with } w_i = \frac{1}{\Delta x_i^2}, \tag{6.1}$$

where x_i are the CNR values for each point in time and Δx_i are the uncertainties for each CNR value calculated by Gaussian error propagation. The uncertainty of the weighted average is:

$$\Delta\overline{x} = \sqrt{\frac{1}{\sum_{i=1}^{4} w_i}}. \tag{6.2}$$

6.6.2 Results

The unfiltered images are shown in Fig. 6.10 together with the calculated temporal subtraction and KES images at different points in time. The unfiltered images are comparable to clinical fluoroscopy images of the gastrointestinal tract where no subtraction imaging is performed and the contrast between the iodine contrast agent and surrounding bone and tissue structures is limited. For each KES image, two subsequently acquired unfiltered and iodine-filtered images were subtracted according to the scheme presented above in Ch. 6.6.1 so that all regions that contain contrast agent are highlighted. In temporal subtraction, only the unfiltered images are needed for the processing, where the first image at $t = 0\,\text{s}$ is logarithmized and subtracted from all following unfiltered images. To simulate the movement of the body through breathing

and of the organs inside, horizontal offsets were applied to the images before processing, both for KES and temporal subtraction.

Both KES and temporal subtraction are able to enhance the contrast between the iodine contrast agent and uncontrasted structures so that the contrast agent is clearly visible on top of background structures and its temporal dispersion can be observed. Yet, small movements of the specimen can be seen in the temporal subtraction images whereas they do not show up in the KES images. This is a major issue in clinical temporal subtraction imaging and limits the application of this imaging method since artifacts from complex movements of organs such as the intestine and the esophagus cannot be corrected. In KES, motion artifacts do not occur since the time difference between the two subtracted images is very small (33 ms in this case). Since the time difference between the subtracted images increases in temporal subtraction with every further image, motion artifacts usually increase over time. Only at time points where – in this simple case of a perfectly periodic motion – the sample is very near to the initial position, as at $t = t4$, there are less artifacts (cf. Fig. 6.10).

CNR(A1,B1)	16.43 s	32.80 s	49.17 s	65.54 s	weighted average
unfiltered	10.5 ± 1.8	10.8 ± 1.9	14.4 ± 2.2	13.8 ± 2.0	12.1 ± 1.0
K-edge subtraction	36.9 ± 9.4	32.0 ± 8.3	41.4 ± 9.6	37.9 ± 6.8	36.9 ± 4.1
temporal subtraction	27.4 ± 7.9	25.2 ± 9.3	36.4 ± 10.1	33.3 ± 7.9	30.4 ± 4.3

Table 6.1: CNR values for unfiltered, KES and temporal subtraction images between regions A1 (contrast agent) and B1 (rib bone) versus the background region in Fig. 6.11. The weighted average was calculated for the four time points named in the table.

To compare the visibility of the iodine contrast agent, the CNR was calculated between iodine contrast agent and bone structures for two different regions shown in Fig. 6.11. The calculated CNR values for iodine and rib bone can be seen in Table 6.1 (regions A1, B1), the values between contrast agent and backbone in Table 6.2 (regions A2, B2). In general, the CNR for all imaging techniques fluctuates slightly over time due to the changing distribution of the contrast agent in the tissue. Still, it can be observed that KES imaging leads to the largest improvement in CNR, while temporal subtraction only partially improves the CNR compared to the unfiltered images.

For regions (A1, B1), KES gives a mean improvement in CNR of over 200 %, while the mean CNR for temporal subtraction is only about 150 % better than in the unfiltered images due to strong motion artifacts. The CNR in the KES images is on average 21.5 % higher than in the temporal subtraction images.

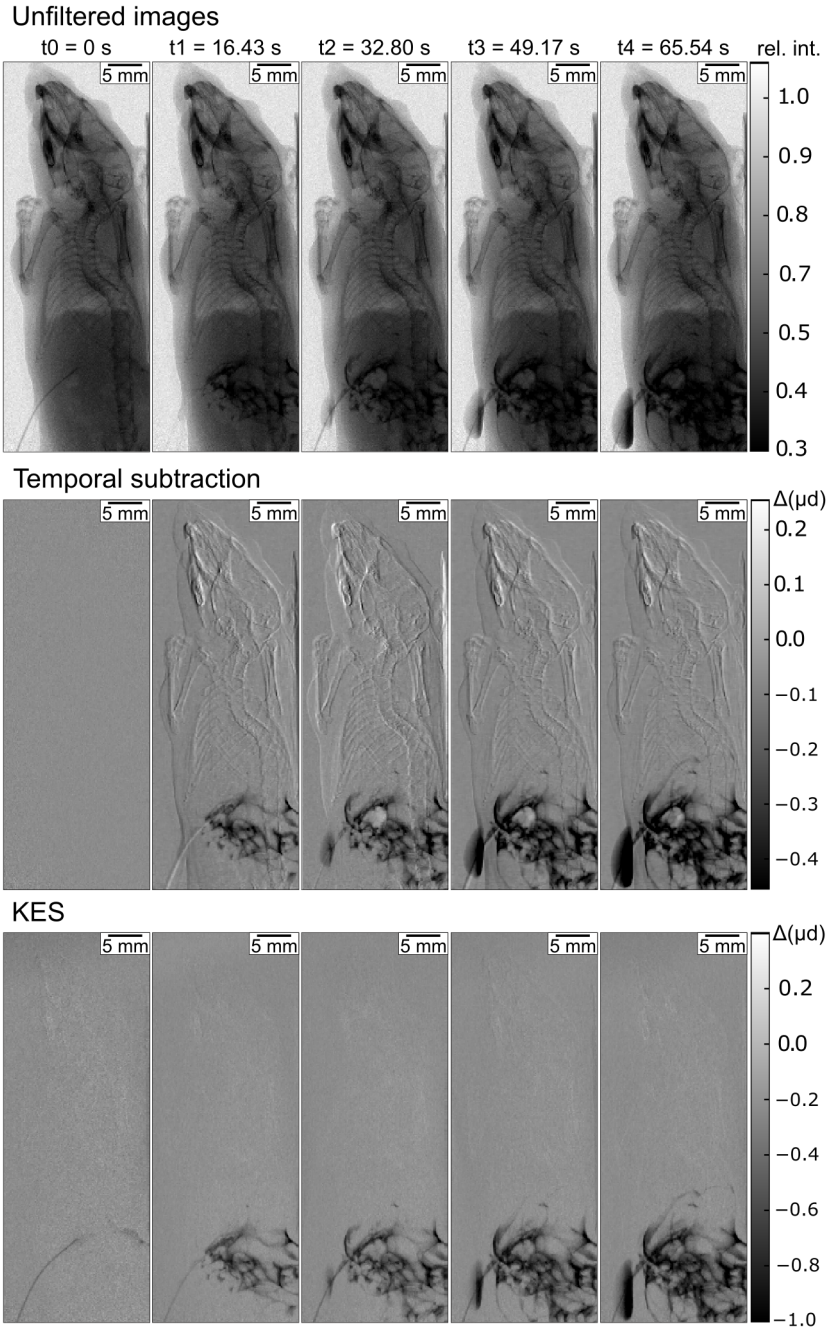

Figure 6.10: Unfiltered, temporal subtraction and KES images of an *ex vivo* mouse, in which iodine contrast agent has been injected at t_0 in the abdominal peritoneal region. In the conventional fluoroscopic X-ray image, the contrast between contrast agent and surrounding bone and tissue is compromised. Both KES and temporal subtraction are able to remove surrounding tissue and bone structures. However, temporal subtraction is prone to artifacts when there is sample movement between the images that are being subtracted. In this case, the movement was simulated by shifting the images with a sinusoidal function continuously to the left and right. The gray scales for the unfiltered images display the relative intensity of the X-ray beam, while the gray values in the KES and temporal subtraction images show the negative differences in absorption. Figure from [Kulpe, 2020a].

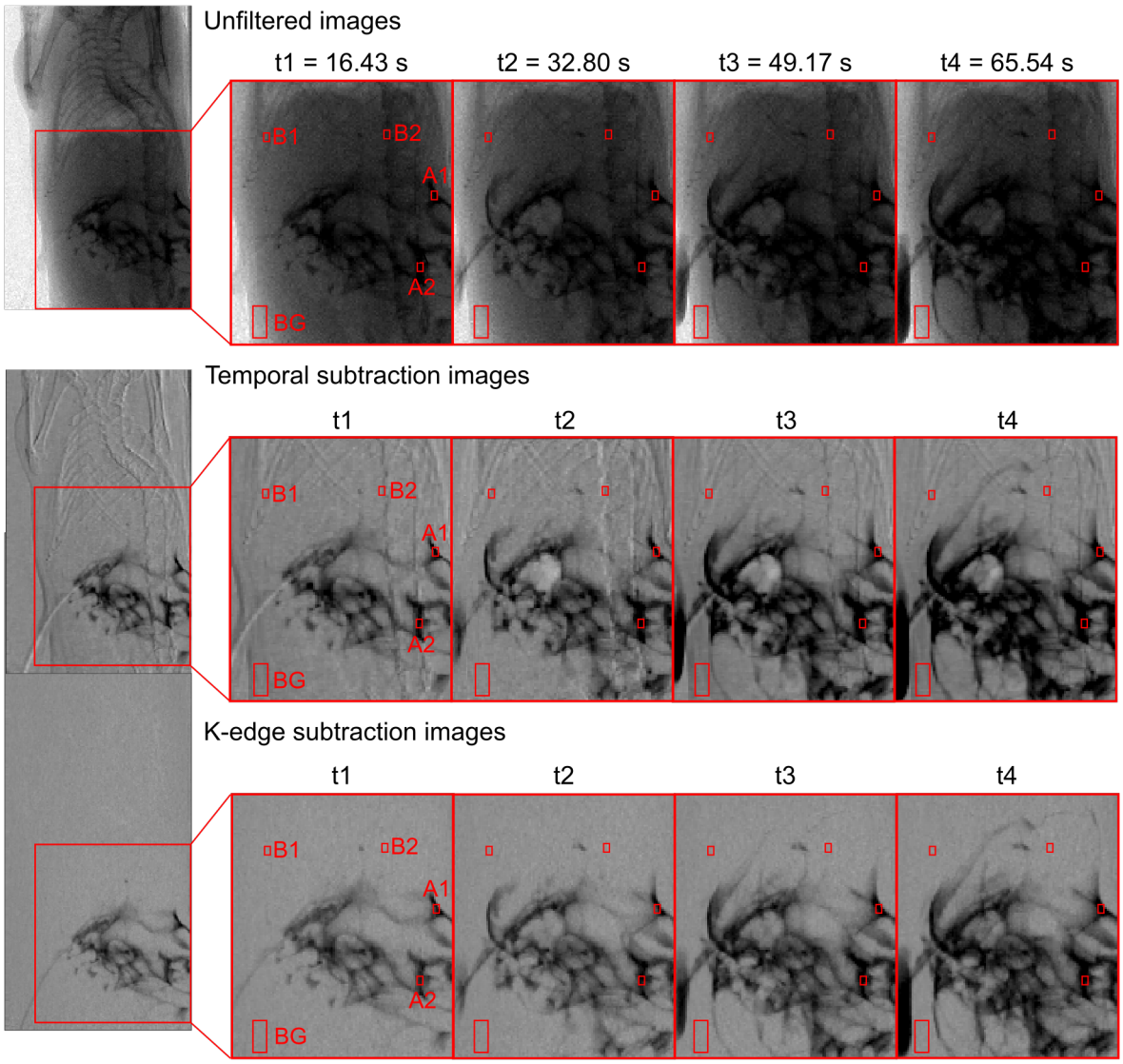

Figure 6.11: Zoom into regions of Fig. 6.10 to show regions of interest (in the abdominal peritoneal region) in unfiltered, temporal subtraction and KES images used to calculate the CNR between iodine contrast agent and bone structures. Regions A1 and A2 contain iodine contrast agent, while B1 and B2 are regions with rib and back bone structures, respectively. The contrast was calculated versus the noise in the larger background region BG. Figure from [Kulpe, 2020a].

For region (A2, B2), the increase in CNR for KES is higher, showing that for contrasted structures that lie in front of strongly absorbing structures, such as the backbone, the visibility will improve substantially by using subtraction imaging. Here, on average, the CNR in the KES images is 7.7 times higher than in the unfiltered images while the CNR in temporal subtraction images is only about 6.8 times larger than in the unfiltered images. Again, the CNR in the KES images is higher than in the temporal subtraction images by about 14.9 %.

CNR(A2,B2)	16.4 s	32.8 s	49.2 s	65.5 s	weighted average
unfiltered	3.7 ± 1.0	4.6 ± 1.2	6.2 ± 1.4	6.0 ± 1.4	4.9 ± 0.6
K-edge subtraction	36.4 ± 4.5	40.3 ± 6.3	42.2 ± 7.9	35.5 ± 6.2	37.8 ± 2.9
temporal subtraction	30.2 ± 6.4	32.3 ± 6.8	38.1 ± 7.6	32.3 ± 6.5	32.9 ± 3.4

Table 6.2: CNR values for unfiltered, KES and temporal subtraction images between the region A2 (iodine contrast agent) and B2 (backbone) versus the background region in Fig. 6.11.

6.6.3 Discussion

The results suggest that K-edge subtraction imaging at a compact synchrotron source, such as the one at the MuCLS, can provide images with improved visibility of contrasted structures in comparison to conventional X-ray images and with reduced artifacts compared to temporal subtraction. The application of KES to the conventional X-ray images improved the visibility of the contrast agent considerably. The CNR in the evaluated regions was significantly higher in the KES images compared to the unfiltered non-subtraction images and between 14.9 % and 21.5 % higher than in the temporal subtraction images. When comparing the CNR for both regions, one can observe that it does not always improve by the same factor compared to non-subtraction images. This cannot only be explained by the emergence of artifacts in the temporal subtraction images, but also with the contrast in the non-subtraction images. If the contrast between contrast agent and bone structures is already very high in non-subtraction images, the improvement in contrast in subtraction imaging does not always exceed the increase in noise and therefore the CNR may not increase [Kulpe, 2018]. This explains why the CNR for the region where the contrast agent is overlaid by the strongly absorbing backbone (A2, B2) is higher than for regions where the contrast agent is compared to rib structures, which absorb the X-rays less.

Especially for clinical settings where subtraction imaging cannot be applied, such as fluoroscopy of the gastrointestinal tract, KES imaging can improve the diagnostics, e.g., when looking for tiny leaks in patients with suspected intestinal perforation. However, the imaging setup was not optimized for high-speed imaging. Since the Pilatus detector has a silicon sensor with a low quantum efficiency at 33 keV, the acquisition time was limited to a minimum of 66 ms to ensure sufficient photon statistics in the images. When using a detector with a more efficient sensor material, such as gadolinium oxysulfide (GadOx), gallium arsenide or cadmium telluride, the acquisition time could be further reduced to allow for even faster time scales. Additionally, the clinical applicability is limited by the achievable X-ray energy of the ICS at the MuCLS. By further developing the source, thus raising the maximum X-ray energy and by using a different contrast material with a higher K-edge energy, e.g., gadolinium, dynamic KES could be applied in a clinical context.

In conclusion, the results show that KES imaging at a compact synchrotron X-ray source can provide X-ray images with higher CNR compared to temporal subtraction. With further development of inverse Compton sources, KES imaging has the potential for advancing existing clinical imaging techniques such as fluoroscopy, where subtraction imaging currently cannot be applied, and may improve diagnostics in the future.

7 X-ray fluorescence imaging

While projection imaging is a common procedure, the analysis of the fluorescent signal of a sample can provide a lot of information about its composition. XRF can be used for non-destructive investigations, thereby ensuring that the sample is conserved in its present state, e.g., when studying cultural heritage objects. In a medical context, XRF allows for further treatments of the sample afterwards, e.g., for histological analysis of tissue samples. Scanning XRF techniques can be used to determine the elemental composition of a sample and provide information that is not accessible in conventional X-ray projection or CT imaging.

This chapter presents the work on XRF performed at the MuCLS. Scanning XRF experiments were conducted to reconstruct the original image of a degraded daguerreotype. For this, the X-ray beam was collimated and focused using polycapillary optics in order to excite fluorescent elements solely in a small area (and thus obtain a high spatial resolution). Additionally, XRF at the MuCLS was used to determine the elemental concentration of several biologically interesting elements in a sample.

7.1 XRF of a daguerreotype

The preservation of cultural heritage objects is of great importance. However, the degeneration over time changes the appearance of these objects such that sometimes the former structure or image cannot be identified. In order to preserve and conserve cultural heritage objects, it is necessary to fully understand their chemical and physical properties [Kozachuk, 2019]. Additionally, the treatments used on the objects should affect neither their present nor future state [AIC, 1994]. In order to assure conservation of these objects, techniques such as Raman spectroscopy [Vandenabeele, 2001] or, most commonly, XRF are used to obtain understanding of the used paints and their former properties such as color, composition and their layering [Klockenkämper, 1993; Klockenkämper, 2000; Camara Neiva, 2014]. By using XRF scanning techniques, elemental maps of paintings can be obtained, allowing for the complete reconstruction of the image and providing information (e.g., underlying brushstrokes) important for the interpretation of a painting [Howard, 2012]. Sometimes, even lost paintings can be discovered underneath others when examining the fluorescent signal of a painting [Dik, 2008].

An image type that is specifically prone to degradation are daguerreotypes. The daguerreotypy was invented by Louis-Jacques-Mandé Daguerre in 1839 [Daguerre, 1839]. It was the first commercially available photography process in the 19th century and was widely used in the 1840s and 1850s [Barger, 1995]. The daguerreotype itself is made of a silver-coated copper plate that is made light sensitive using an iodine vapour,

and is finally developed and preserved using mercury vapour and a gold coating after illumination [Martin, 1851; Barger, 1995]. The image on the daguerreotype is formed by reflection of light from the silver-mercury clusters and gold particles on its surface [Kozachuk, 2018b]. However, over time the reflective surface layer can corrode, forming films of silver or copper alloys that distort the original image [Kozachuk, 2019].

Although the degeneration processes on the daguerreotype surfaces are not fully understood [Centeno, 2011; Kozachuk, 2018a], several treatment methods, such as electroplating, that can be used to remove films impairing the visual impression of a daguerreotype have been developed [Da Silva, 2010]. However, these methods can potentially alter the chemical structure of the image [Barger, 1995; Da Silva, 2010] while XRF scanning can be used to reconstruct the original image without manipulation of the sample. Severely degraded daguerreotypes are usually investigated at dedicated μ-XRF setups at synchrotron sources since portable XRF systems lack the small X-ray beams, typically a few tens of micrometer in diameter, required to resolve the local tonal variations on the sample surface [Kozachuk, 2018b]. Nevertheless, using appropriate post-processing algorithms, the examination of a daguerreotype can also be performed at a tabletop μ-XRF setup [Davis, 2016]. Several studies both at synchrotrons and tabletop systems have shown that the mercury fluorescence signal of a daguerreotype enables the complete reconstruction of the image [Da Silva, 2010; Camara Neiva, 2014; Davis, 2016], even for highly degraded samples [Kozachuk, 2018b].

In this thesis, a degenerated daguerreotype was investigated in the first experimental endstation at the MuCLS. The X-ray beam was focused to ensure excitation of the sample only in a certain area. It is scanned over the daguerreotype and at each position a spectrum is acquired with a silicon-drift detector (AXAS-D, KETEK GmbH, Germany). This procedure generates a fluorescence image, whose resolution is determined by the excited area.

7.1.1 Sample

The daguerreotype that was analyzed is presented in Fig. 7.1a. The photograph displays a sitting young girl wearing a dark dress with white flowers and holding a purse (or similar object) on her lap. As the quality of the image has degraded over time, not all details of the image remain clearly visible. The plate was obtained from the research group of Prof. Tsun-Kong Sham from the Chemistry Department at the University of Western Ontario, London, Ontario, Canada and returned to them after the experiments.

Production of Daguerreotypes

To investigate the XRF signal from this kind of sample, it is necessary to understand how daguerreotypes are produced. The main structure of the plate is a copper substrate covered by a thin, highly polished layer of silver. The daguerreotype image is then formed on the silver surface. In order to make the plate light sensitive, it is fumed

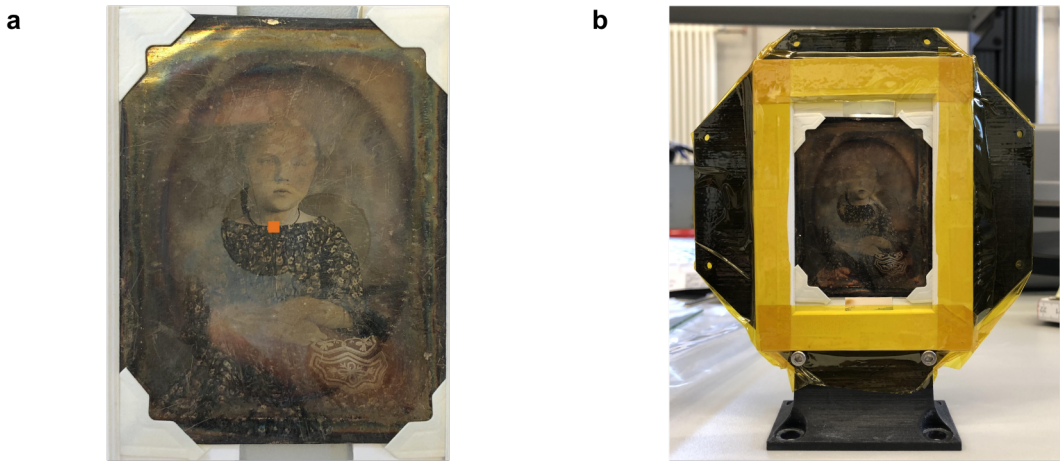

Figure 7.1: **a** Image of daguerreotype of which fluorescent signals were investigated. The image shows a sitting girl in a black dress holding an object on her lap. The orange square marks the region of the sample that was scanned; **b** The same daguerreotype mounted onto a 3D-printed grating holder using Kapton tape. This holder was used in the experiment.

in darkness or under safelight with a halogen, producing a light sensitive layer of silver halide on the surface of the plate. This halogen is either iodine, chlorine or bromine. However a combined, subsequent exposure with iodine and bromine fumes produces the most light-sensitive silver halide layer. This plate has to be kept in a light-tight container until used for image acquisition in a camera. During illumination of the plate, an invisible image is created on the plate. Exposure to light catalyzes a photolytic reduction of the silver halides, creating metallic silver clusters on the plate. The exposure time thereby depends on the brightness of the light, the imaging system of the camera as well as the sensitivity of the photo-active layer on the plate and ranges from a few seconds to several minutes. After the exposure, the plate is developed using mercury fumes. For this purpose, the plate is placed into a box containing heated liquid mercury. The mercury reacts with the silver clusters and forms silver-mercury particles [Martin, 1851]. The density and average size of the particles are directly related to the light exposure with smaller particles and higher densities in strongly illuminated, so called highlight areas. The average diameters of these particles vary from $0.1 - 1\,\mu m$ (highlight areas) to $0.25 - 2.5\,\mu m$ for midtones and approximately $10 - 50\,\mu m$ in the shadow areas [Barger, 1995]. Afterwards, remaining unexposed silver halide is removed using a mild sodium thiosulfate ($Na_2S_2O_3{:}xH_2O$) solution. This terminates the light sensitivity of the plate and fixates the image. Typically, to improve the visual impression of the image and give it a warmer tone, a gold toning was performed by placing the plate into a gold chloride solution and briefly heating it over a flame. This produces a thin gold layer, which additionally extends the lifetime of the image, on the surface [Martin, 1851; Schlather, 2019].

The element of interest for XRF is mercury (Hg) since the image information correlates with the silver-mercury clusters on the plate. Other elements contained in the sample are copper (Cu) and gold (Ag).

Mounting of sample

The mounting of the daguerreotype is displayed in Fig. 7.1b. The daguerreotype was kept in the transport frame and mounted on a 3D printed grating holder using Kapton tape. This mounting prevented damage to the sample surface such as degradation by any tape touching it. It also reduced risk when handling the sample as substances on the surface might cause health risks. The foot of the grating holder has 4 holes for M6 screws, allowing to mount it on the standard sample stage.

7.1.2 Experimental setup

To examine the daguerreotype, an XRF scanning setup was constructed. The initial experimental setup ("Setup 90°") is shown in Fig. 7.2a. The X-ray beam was tuned to a peak energy of 25 keV and undergoes a first weak focusing by a polycapillary optic ("optic 1") before it leaves the radiation shielding enclosure of the ICS. This improves the focusing of the beam in the second optic ("optic 2"). Optic 2 has short working distance of 17 mm and is designed for a parallel beam. It focuses the converged beam down further to a minimum size of $40 \times 40\,\mu m^2$ at the focal distance. Since the tightly focusing optic 2 is a polycapillary, a small inner center of the X-ray beam cannot be focused. Instead of the commonly used central stop, a small tungsten plate suppresses this central beam, which is slightly inclined to the focused one.

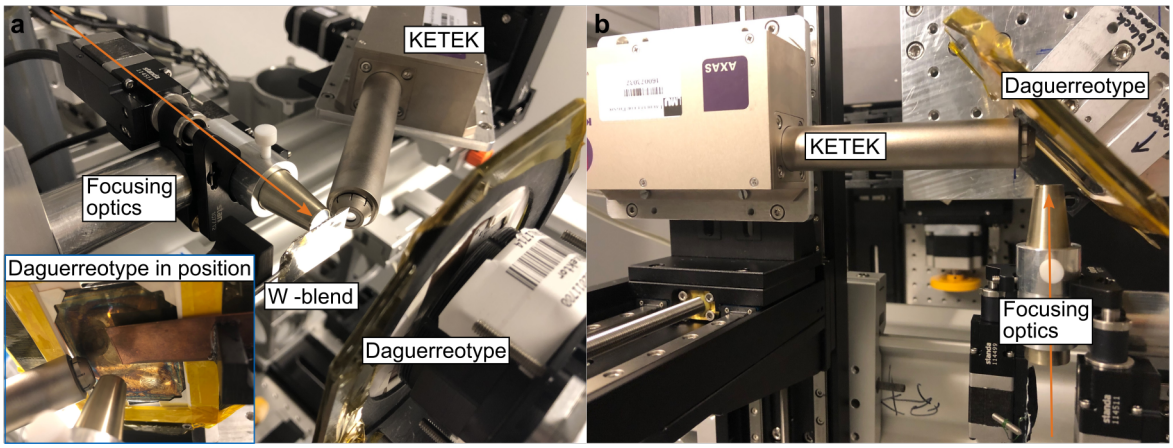

Figure 7.2: **a** Setup 90°: Initial experimental setup for scanning XRF of the daguerreotype. The incident X-ray beam is focused by the focusing optics. The unfocused part of the beam is blocked by the tungsten blend such that only the focus hits the sample (in the large image the daguerreotype is moved to the back to make the setup visible, the daguerreotype is in the correct position in the small image in the blue box). The fluorescent signal is detected by the AXAS-D detector; **b** Setup 45°: Optimized setup enabling a smaller sample-to-detector distance. The daguerreotype is tilted by 45° to the incident beam and the AXAS-D detector by 90°.

The fluorescent signal was collected with an energy-dispersive silicon-drift detector

(AXAS-D, Ketek GmbH, Germany) that was oriented at an angle of 135° to the incident beam. Since the sample is made from a highly absorbing copper-silver plate, there is almost no Compton scattering disturbing the fluorescent signal from the sample in the measured spectra. The sample-to-detector distance is limited by the cone of the X-ray beam emerging from the focusing optics. The minimum distance between sample and detector, in this configuration, is 10 mm, limiting the amount of fluorescent signal that can be collected.

Decreasing the sample-to-detector distance improves the collection of the fluorescent signal. To this end, the sample was rotated by 45° relative to the incident X-ray beam. This setup, shown in Fig. 7.2b, will be called "Setup 45°" in the following. The AXAS-D detector was placed at an angle of 90° to the incident beam. This reduced the sample-to-detector distance to around 6 mm. An area around the neckline of the dress was imaged to observe if a change between an area with high and low silver-mercury concentration can be identified in the intensity of the mercury fluorescence. In this region, the amount of mercury in the photograph should change drastically between the white neck area and the dark skirt. Therefore, the scans were usually performed over an area of $0.05 - 0.10 \times 2.00$ mm (horizontal x vertical direction) to see if these changes can be resolved with a reasonable exposure time before scanning the whole sample. Scans were performed with both setups. The acquired spectra were corrected for background noise by subtracting the mean signal level determined in a region free from fluorescent peaks in the spectrum. The individual fluorescent peaks were fitted with a Gaussian function. A two-dimensional image is generated by translating the sample position into the pixel coordinate like in standard scanning approaches. The pixel value is the height of the Gaussian fitted to the mercury peak at each spatial position.

Installation of focusing optics 2

The focusing optics is mounted onto a motorized one-inch mirror mount in order to enable optimization of the optics' tilt in the horizontal as well as vertical direction. Moreover, it can be moved in both directions transverse to the X-ray beam propagation by motorized stages. Solely the position along the beam axis is fixed. The focus of the X-ray beam can be optimized using these four degrees of freedom. Thereby, the movement in vertical and horizontal direction ensures that the optics is centered in the incident (in this case pre-focused) X-ray beam while the rotational degrees of freedom adjust the optics' orientation in the X-ray beam, thus are used to optimize its focus. To monitor the focus during optimization, a CCD-camera (xiRay, XIMEA GmbH, Germany) is placed at the position of the focus and an image is acquired after every change in one of the four degrees of freedom. This setup is shown in Fig. 7.3a and b. An X-ray image of the optimized focus can be seen in Fig. 7.3c. The focus has a size of 4.45×4.45 pixels which corresponds to a size of $40.1 \times 40.1\,\mu m^2$ (pixel size of Ximea: 9 µm) with a flux of ~ 12000 counts acquired with an exposure time of 0.01 s. After focus optimization, the xiRay detector is removed and the sample is placed at the same position.

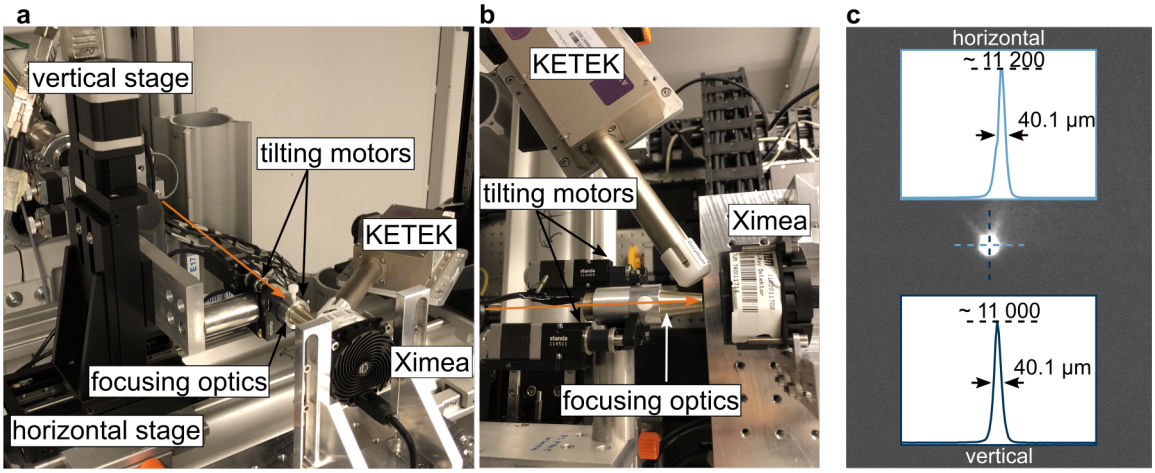

Figure 7.3: Installation of the focusing optics in the first endstation at MuCLS. The orange arrow indicates the X-ray beam direction. **a** Setup of the focusing optics for focus optimization; **b** Top view of the setup; **c** X-ray image of the optimized focus acquired with the Ximea detector.

7.1.3 Results

In preparation for the daguerreotype scan, a phantom containing all elements relevant for the daguerreotype measurement was investigated at 35 keV. The spectrum that was acquired with 60 s exposure time can be seen in Fig. 7.4a. The fluorescent peaks of all elements are clearly visible although the energies of the Au and Hg fluorescence L-lines are very similar ($\sim$ 9.7 keV (Au) vs. $\sim$ 9.9 keV (Hg)). These two peaks clearly overlap in the spectrum and could therefore be more difficult to distinguish for lower intensities. Additionally, the K_β-peak of silver is overlapped with the Compton scattering peak. However, since the intensity of the K_α-peak is around four times higher than the K_β-peak, only the former will be analyzed. Since the focusing optics are optimized for 25 keV, the daguerreotype is measured at this energy. As the K-edge of silver is not excited with this spectrum, the L_α was analyzed instead. In Fig. 7.4b the spectrum acquired with 60 s exposure time at one point on the daguerreotype is shown. The spectrum is dominated by the characteristic copper lines. All other elements have much lower fluorescent signals. The intensities of the characteristic lines of mercury are significantly smaller in the daguerreotype. This is caused by the very low mercury concentration on its surface. Consequently, the minimum acquisition time is determined by the statistics required to distinguish the gold and mercury lines. Although the spectra were measured at different X-ray energies, the incident flux of the exciting X-ray beams were similar. The 25 keV spectrum is enhanced in flux by focusing, leading to a similar X-ray flux as the 35 keV spectrum had during the measurement. In comparison to the spectrum of the phantom, there is almost no Compton scattering peak in the spectrum acquired from the daguerreotype. The reason for this is that the daguerreotype is mainly composed of a highly absorbing copper plate. Additionally, at 25 keV the attenuation in the sample is dominated by the photoelectric effect.

Therefore, there will be hardly any scattering disturbing the fluorescent signal.

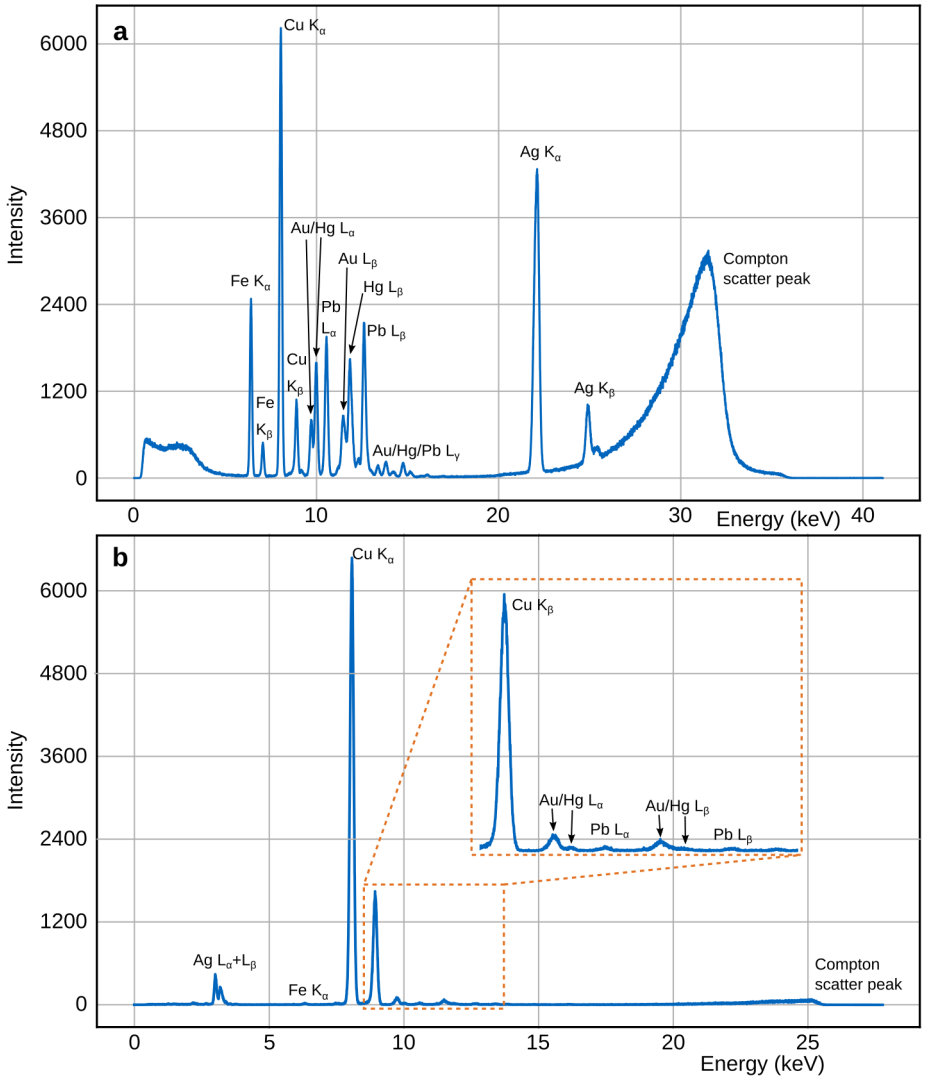

Figure 7.4: Fluorescent spectra obtained from a phantom and the daguerreotype using the 35 keV and 25 keV spectra of the MuCLS, respectively. **a** Spectrum obtained from the measurement of a phantom containing all relevant elements of the daguerreotype. All elements can be clearly identified, including the fluorescent signals of Au and Hg; **b** Spectrum obtained from the surface of the daguerreotype. The fluorescent signals of some elements are significantly weaker than in the measurement of the phantom. The signals from Au and Hg are more difficult to distinguish. This limits the minimum acquisition time.

Fig. 7.5 shows the fluorescent signal of mercury for two scans performed with the two different setup geometries depicted in Fig. 7.2. Fig. 7.5a was acquired with the Setup 90° (Fig. 7.2a) and Fig. 7.5b with the Setup 45° (Fig. 7.2b). Using Setup 90°, spectra with different acquisition times were acquired. The minimum acquisition time to distinguish mercury and gold was found to be 30 s. However, the peak only has a height of $2 - 3$ counts at 30 s exposure time. Therefore, the acquisition time per

point was set to 60 s to obtain better photon statistics. Still, the scan using the setup in Fig. 7.2a (acquisition time per point: 60 s) shows no change in the mercury signal although there should be a change in the amount of mercury on the sample surface when scanning over the neckline of the skirt, i.e., scanning from the bright area to the dark area of the daguerreotype. Since there was also no visible structure in the fluorescent signals of the other elements, only the mercury signal is shown exemplarily. With Setup 45° (acquisition time per point: 60 s), the signal showed a change in the fluorescent signal of mercury while scanning over the neckline of the dress (cf. Fig. 7.5b). All other elements showed no interesting structures in the fluorescent signals. However, due to the tilting of the sample, any movement of the sample stage in horizontal direction would also lead to a change in distance between sample and focusing optics in beam direction, thus moving the sample out of the focus. Therefore, it was not possible to scan in horizontal direction without having to mount it onto an additional set of sample stages, allowing for movement in beam direction and horizontally perpendicular to it. While the scan was successful, it was abstained from performing further scans due to the long measurement time needed to obtain good results. Fig. 7.5c shows a

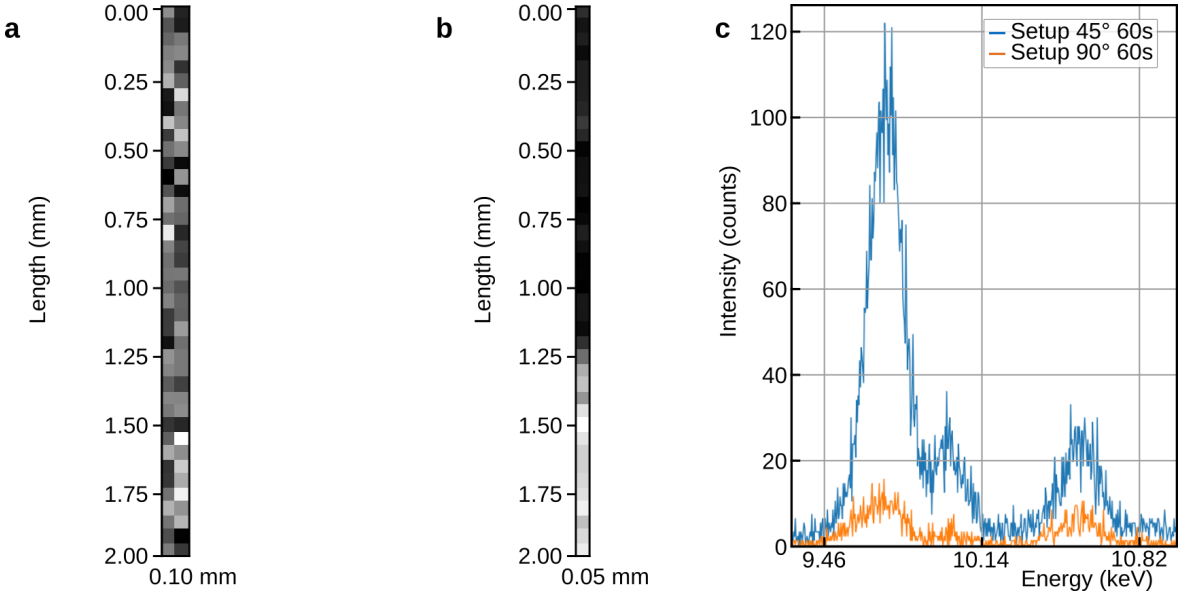

Figure 7.5: Mercury signal for scans over the neckline of dress in daguerreotype. **a** Mercury signal for a scan across an area of $0.1 \times 2.0\,\mathrm{mm}^2$ using the Setup 90° (Fig. 7.2a). No structure in the mercury signal is visible although the amount of mercury on the sample surface changes; **b** The mercury signal for a scan across an area of $0.05 \times 2.00\,\mathrm{mm}^2$ using Setup 45° (Fig. 7.2b). The mercury signal shows a change when scanning over the neckline; **c** Comparison of peak heights of Au and Hg peaks for different setups at 60 s exposure time.

comparison of the fluorescent signal of one point on the daguerreotype acquired with the two different setups and an exposure time of 60 s. It can be clearly seen that the setup with the tilted daguerreotype captures more of the X-ray fluorescence of the sample due to the smaller sample-to-detector distance. The scan presented here had a total measurement time of 41 min and 15 s for 40 measurement points with 60 s

acquisition time. This would lead to a measurement time of around 27 h for a scan of $2 \times 2\,\mathrm{mm}^2$ and would make a scan of the whole sample ($\sim 4 \times 5\,\mathrm{cm}^2$) impossible at the MuCLS. Even when reducing the acquisition time per point to 30 s, which in a first test produced reasonable results, the measurement time would still be significantly higher than at a synchrotron source.

7.1.4 Discussion

The results showed that the XRF analysis of the surface of a daguerreotype at the MuCLS in principle is possible, however only at very long measurement times. The main limitation in the experiments was the large sample-to-detector distance as well as the limited opening angle of the detector that prevented the detection of a large part of the (very weak) fluorescent signal of the sample. Here, the small working distance of the focusing optics and the resulting beam cone in front of the focus hindered the detector from being placed closer to the sample surface. With an improved setup, thereby tilting the daguerreotype in an angle of 45° to the incident beam direction, the distance could be reduced. Still, the measurement time was too long to allow for a scan of the daguerreotype in a reasonable amount of time.

This could probably be resolved by using a different spectral detector. One possible detector would be the Maia-384 element detector (used for the XRF analysis of a daguerreotype at a synchrotron in [Kozachuk, 2018b]). This detector was developed for the X-ray fluorescence microscopy (XFM) beamline at the Australian synchrotron [Ryan, 2014]. It has an opening in the centre of its detector array allowing for the incident X-ray beam to pass through the detector onto the sample. Therefore, the detector can be placed at a very small working distance in front of the sample of interest. Consequently, a large solid angle is covered by the detector which increases the efficiency of the detection of fluorescence and in turn significantly reduces exposure.

For XRF scanning with a small pixel size, the application at a synchrotron is not necessarily beneficial since the X-ray beam has to be focused to obtain the required pixel size and its naturally high flux has to be attenuated to avoid saturating the detector. Although the X-ray beam at the MuCLS is attenuated during focusing due to the absorption inside the focusing optics, the achieved focal spot with small size and high flux density would be optimal for XRF with specialized detectors.

In conclusion, the implementation of a specialized fluorescence detector, such as the Maia, would enable the investigation of degraded daguerreotypes via XRF at the MuCLS and other inverse Compton X-ray sources. This would allow their investigation in a laboratory frame with a high resolution and reduce the need for synchrotron beam time.

7.2 XRF scanning at 35 keV

Although the 25 keV X-ray beam at the MuCLS was successfully focused using a polycapillary optics, the K-edge of many biologically interesting elements cannot be excited at this energy. Therefore, a higher energy configuration for scanning XRF is desirable. Different configurations of the available hardware components for focusing and collimation were tested with the aim to optimize the focal spot size. Fig. 7.6 presents X-ray images of the focuses obtained with different setups acquired with the xiRay detector (pixel size 9 µm, more detector characteristics can be found in Ch. 4.3). In Fig. 7.6a only the focusing optic 2 was used, in Fig. 7.6b both polycapillary optics 1 and 2 were used, in Fig. 7.6c optic 1 was used together with a manually adjustable tungsten blend, in Fig. 7.6d only the blend was placed into the beam and in Fig. 7.6e the preinstalled slit system was used to close down the X-ray beam. As can be seen in Fig. 7.6a and

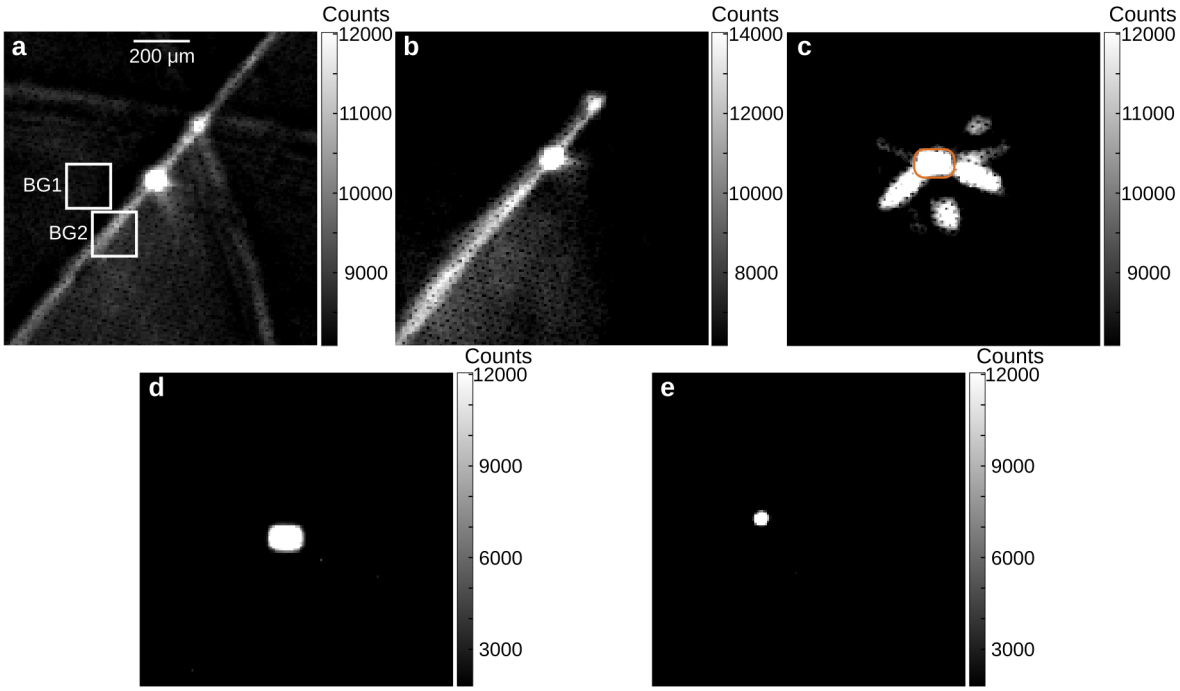

Figure 7.6: Focus of the 35 keV beam achieved with different setups. **a** Beam was focused only by the focusing optic 2; **b** Beam was focused by both polycapillary optics 1 and 2; **c** Focus achieved when using the polycapillary optic 1 in the cave and a blend. The focal spot is marked by the orange outline; **d** The beam collimated by the blend; **e** Size of X-ray beam when using the preinstalled slit system to close it down. All gray scales show the number of counts per pixel.

b, the focusing optic 2 is not optimized for this X-ray energy and bright streaks arise in addition to the focal spot. Although weak streaks also appeared using the optics at 25 keV (cf. Fig. 7.3c), the streaks at 35 keV are significantly stronger and lead to a background signal that will reduce the accuracy of the XRF scanning setup. Also, setup used for Fig. 7.6c is not optimal since streaks arise outside of the blend opening.

The image only shows the most intense streaks since the image was windowed such that the focus is visible. These streaks do not arise from the beam penetrating the closed parts of the blend, but rather arise from parts of the focused X-ray beam that travel diagonally through the blend opening. This was verified by moving the X-ray detector around and analyzing changes in the streak pattern. Fig. 7.6d shows the beam obtained using only the blend to decrease the illuminated area. There are no streaks or other disturbing background signals next to the focus. However, since the blend has to be adjusted manually, it was rather time consuming to optimize the single blend positions, and the obtained spot size is relatively large. Additionally, the manual positioning and adjustment of the blend makes it difficult to obtain reproducible results. Lastly, Fig. 7.6e shows the spot size obtained when collimating the X-ray beam using the preinstalled slit system at the MuCLS. The slits are motorized and both vertical and horizontal gap size as well as the offset of the gap (thus the position of the gap relative to the center of the X-ray beam) can be adjusted. This setup provides a very symmetric and small spot size without any intensity distribution in the background area.

Setup	Focus/spot size (FWHM)	Focus height (counts)	Background region 1	Background region 2
a	17×16 px $153 \times 144\,\mu m^2$	$15\,401 \pm 345$	$4\,149 \pm 499$	$7\,653 \pm 1613$
b	16×13 px $144 \times 117\,\mu m^2$	$15\,354 \pm 338$	$4\,919 \pm 430$	$8\,658 \pm 2141$
c	20×9 px $180 \times 81\,\mu m^2$	$13\,969 \pm 439$	$4\,224 \pm 1\,332$	223 ± 220
d	25×19 px $225 \times 171\,\mu m^2$	$14\,388 \pm 304$	7 ± 47	4 ± 74
e	10×10 px $90 \times 90\,\mu m^2$	$14\,593 \pm 385$	3 ± 47	3 ± 70

Table 7.1: Characteristics of foci achieved with different setups. All images were corrected for dark current before quantitative analysis. The pixel size of the Ximea detector is 9 µm (more detector characteristics can be found in Ch. 4.3).

After visual inspection of the obtained focuses, they were analyzed quantitatively. The results are shown in Table 7.1. The dark current from the detector was subtracted from all images using a dark image before calculating the focus intensities using a Gaussian fit and the mean number of counts in the background regions. It can be seen that setup e gives the smallest and most symmetric spot size with $90 \times 90\,\mu m^2$ at FWHM. Although its peak intensity is around 5 % lower than for setup a (using only the focusing optics), this setup contains barely any X-ray signal outside the desired location. This is different for the setups employing one or both of the focusing optics (setups a-c). In these setups, a significant portion of the beam power is distributed outside of the focus or spot where intensity can reach half of the peaks intensity (setup b background

region 2). The radiation outside of the focus will decrease the spatial resolution in XRF scanning since fluorescence will be excited in areas outside the nominal focus and accordingly will be detected by the spectrometer. This will disturb the measurement accuracy of the XRF setup. Setup d does not have this disadvantage, however the spot size is more than twice as large as in setup e and less symmetric. The slight change in X-ray flux between these two setups may arise from fluctuations of the X-ray beam. Nonetheless, setup e provides the most suitable spot size for XRF scanning. Therefore, it was used for the experiments presented subsequently.

7.2.1 First XRF scanning results using 35 keV spectrum

A 300 µm thick wire was investigated in a first scanning XRF experiment at 35 keV at the MuCLS. A similar setup was used as for the scanning of the daguerreotype in the previous chapter (cf. Fig. 7.2a). Both setups differ only in the generation of the small beam illuminating the sample. While in the former experiment the beam was focused with polycapillary optics, here a slit-system produces a small pencil beam (setup e described above). The KETEK AXAS-D detector was placed as closely to the sample as possible without blocking the incident X-ray beam. This results in an approximate sample-to-detector distance of 10 mm measured from the point of excitation to the center of the detector surface. In a first measurement, the fluorescent signal of the wire contained peaks that are associated with iron and zinc. Therefore, these two elements were analyzed in the following XRF scanning. The sample (cf. Fig. 7.7a) was raster-scanned with a pixel size of $50 \times 50\mu m^2$ across an area of 2 mm × 100µm (horizontal x vertical direction). The acquisition per spectrum took 10 s at each position. The fluorescent signals were analyzed according to the procedure described in Ch. 7.1.2. Fig. 7.7b and c show the results obtained for zinc and iron, respectively. Generally, a

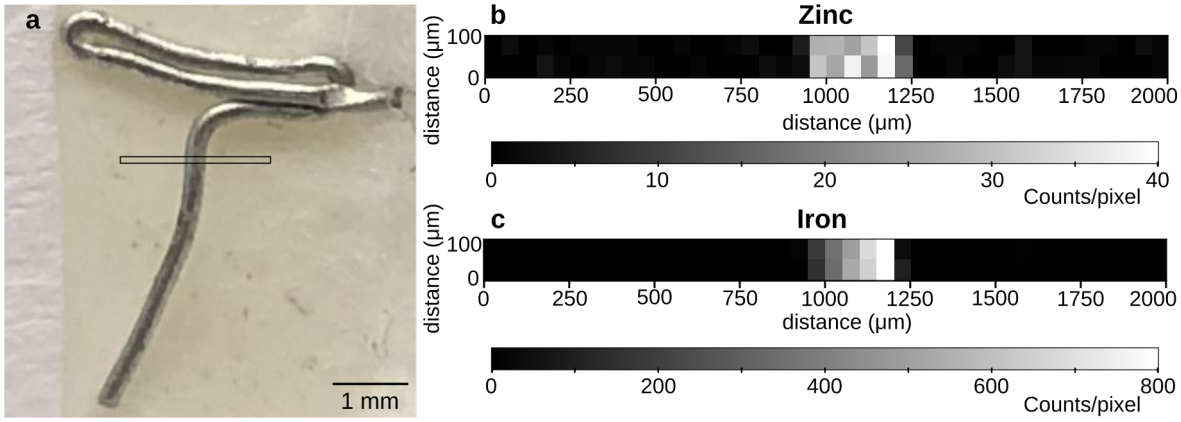

Figure 7.7: Results of a first XRF scanning experiment at 35 keV. **a** A wire with a diameter of 300 µm was glued onto a flat surface and scanned. The scanned region is indicated by the black rectangle; **b** Scanning XRF image showing zinc fluorescence. There is a clear increase in the fluorescent signal in the area of the wire; **c** Scanning XRF image of iron. Again, the detector only measures a signal when the wire is in the beam. The grayscales show the number of counts per pixel.

signal from the two elements can be detected only when the X-ray beam hits the wire. Therefore it can be clearly identified in both scanning XRF images. The fluorescent signal of iron is significantly higher than the one of zinc. Since the atomic numbers from both elements are very similar (26 (Fe) vs. 30 (Zn)), their fluorescent yield is almost identical (cf. Fig. 2.6 in Ch. 2.8). Thus, it can be assumed that the wire is mainly made of iron and is probably only coated with zinc to avoid corrosion.

The first scanning XRF experiment at 35 keV demonstrated very promising results. Further experiments should be performed to evaluate the sensitivity of the setup and its ability to detect very low elemental concentrations. In the future, this setup could be used to measure biopsy samples to determine the distribution of biologically relevant elements inside the sample. If one is only interested in the overall concentration of an element inside a sample, XRF scanning is not necessary as can be seen in the next chapter.

7.3 XRF to determine the concentration of elements in a sample

While XRF can be used for the investigation of cultural heritage objects, it also has a long history in elemental trace and concentration detection. In combination with an appropriate calibration and analysis, XRF can estimate the relative or absolute concentration of elements in a sample. In the past, XRF has been used for rock analysis and for the determination of elemental concentrations in soils, cells and tissues. Hereby, the information about metal traces in soil or rain water can provide information about potential health risks or environmental pollution. Furthermore, the concentration of certain elements indicates if a tissue is healthy or, for example, cancerous. Another important application of XRF is human nutrition and toxicology, where accurate and simple estimation of essential and toxic trace elements is needed [Iyengar, 1981].

XRF has been extensively used to determine the spatial distribution of trace elements in animal and human tissue. It was found that various tissue types show significant differences in the concentration of trace metal elements such as iron, zinc, copper and lead between healthy and pathological findings [Gherase, 2020]. Some metals, such as cadmium, chromium and nickel, are well-known and well-studied carcinogens [Durham, 2006]. Zinc levels are an important indicator for prostate cancer (adenocarcinoma) [Ide-Ektessabi, 2002] and for ductal carcinoma in breast tissue since zinc is known to be a co-factor for more than 300 enzymes. Other studies showed that potassium, calcium, iron and copper are biologically important elements for cancer lesions [Geraki, 2008; Silva, 2009; Al-Ebraheem, 2009]. In addition to indicating cancerous lesions, Pascolo et al. demonstrated that iron levels are highly elevated for patients having had contact with asbestos [Pascolo, 2013]. Also, neurodegenerative conditions such as Parkinson's and Alzheimer's disease exhibit abnormalities in the trace element concentrations of iron, zinc and copper [Miller, 2006; Popescu, 2009].

Elemental deposits in tissues can also provide information about environmental expo-

sures or air pollution a subject experienced [Gianoncelli, 2018]. Three to nine times higher lead concentrations are present in the skeleton of workers from the metal industry compared to average ones [Ahlgren, 1976]. Silver, a metal that is commonly used in industrial processes, e.g., in electronics, electrical equipment as well as photographic and imaging industries, also has the tendency to accumulate in tissues such as the skin [Graham, 2004]. Additionally, it has been found in the liver of marine mammals that consumed contaminated foods [Nakazawa, 2011].

XRF has not only been used to evaluate tissue samples, but also to track the environmental condition and air pollution. Already in 1985, trace element detection in rainwater was used to determine the environmental hazards arising from heavy metals in the atmosphere [Stössel, 1985]. Another powerful application of XRF is honey "fingerprinting". The elemental content of honey provides information about the status of the environment since its fluorescence signature originates from the composition of plant juices [Kump, 1996]. In areas close to industrial sites or in agriculture, the pollution of soil with heavy metals [Ene, 2010] or pesticides containing bromine has been investigated [Gallardo, 2016]. Although iodine and bromine are essential trace elements for many organisms, high concentrations of these elements can be toxic. Therefore their concentration in soils are of interest [Takeda, 2011]. Especially vegetables that were treated with the pesticide methyl bromide and are taken up by humans and animals can be a potential health risk [Mino, 2005].

This chapter presents the XRF experiments that were conducted to determine the elemental concentrations of iron, zinc, bromine, silver and iodine in different samples.

7.3.1 Samples

Elements of interest

In this work, several elements were under investigation, namely iron, zinc, bromine, silver and iodine. In order to determine the detection limit of these elements, concentration rows with elemental concentrations ranging from 0.25 µg/ml up to 600 mg/ml were measured. The concentrations for each element are presented in Table 7.2. In order to obtain samples with a homogeneous distribution of the desired element, soluble salts containing the element were dissolved in water. Hereby, the maximum concentration of the element (the concentration of the salt was higher depending on the proportion of element weight to molar mass of the salt) was 600 mg/ml for bromine and 1000 µg/ml for all other elements. This solution was further diluted with water to obtain the other, less concentrated, solutions.

The solutions were filled into cylindrical sample containers, which were illuminated with a small square X-ray beam equal to the diameter of the sample container. The elements with K-edge energies below 25 keV, namely iron, zinc and bromine, are excited with the 25 keV spectrum provided at the MuCLS while silver and iodine are excited with the 35 keV spectrum in these experiments.

Element	K-edge energy	K_α-line	Sample composition	Elemental concentration
Iron (Fe)	7.11 keV	6.4 keV	$FeCl_3 + H_2O$	0.25 µg/ml – 1000 µg/ml
Zinc (Zn)	9.66 keV	8.6 keV	$ZnCl_2 + H_2O$	0.25 µg/ml – 1000 µg/ml
Bromine (Br)	13.47 keV	11.9 keV	$NaBr + H_2O$	0.5 mg/ml – 600 mg/ml
Silver (Ag)	25.51 keV	22.0 keV	$AgNO_3 + H_2O$	0.25 µg/ml – 1000 µg/ml
Iodine (I)	33.17 keV	28.5 keV	$NaI + H_2O$	0.25 µg/ml – 1000 µg/ml

Table 7.2: Elements and concentration rows used for XRF in combination with the K-absorption edge energy and the energy of the K_α fluorescent line. The concentrations refer to the pure elements, not to the salt.

Problems with sample containers

The first sample containers used were Eppendorf tubes with a filling volume of 0.3 ml, a diameter of 5 mm and a wall thickness of 0.2 mm. These tubes were made from polypropylene (PP). While the tube's dimensions are very exact, the material contains traces of zinc, which prevents quantitative analysis of the fluorescence signal for the zinc solutions. Moreover, the zinc concentration in each tube is not identical. Accordingly, it cannot be subtracted properly in post-processing of the recorded data. The zinc in the PP could be part of an additive used to stabilize the plastic against UV light, however the manufacturer did not reply to this question. Nonetheless, the iron solutions were measured in these containers since the fluorescent line of this element is strongly absorbed by the glass of the NMR tubes employed in the other experiments.

Filling solutions into NMR tubes

In order to ensure that there are no disturbing signals in the sample containers, NMR tubes made from glass were used in the majority of cases (cf. Fig. 7.8a). These had an outer diameter of 3 mm, a wall thickness of 0.25 mm and a length of 178 mm. Due to the small diameter of the tubes, they could not be filled easily. When filling the solution using a pipette, larger drops of liquid would easily clog the tube (cf. Fig. 7.8b). Therefore, it was necessary to first let a single small drop glide along the inner wall of the tube all the way to its bottom. This allowed for a fluid film to build up on the inner wall of the tube. Subsequently injected liquid then glides along this fluid film without clogging the tube. This procedure is shown in Fig. 7.8c.

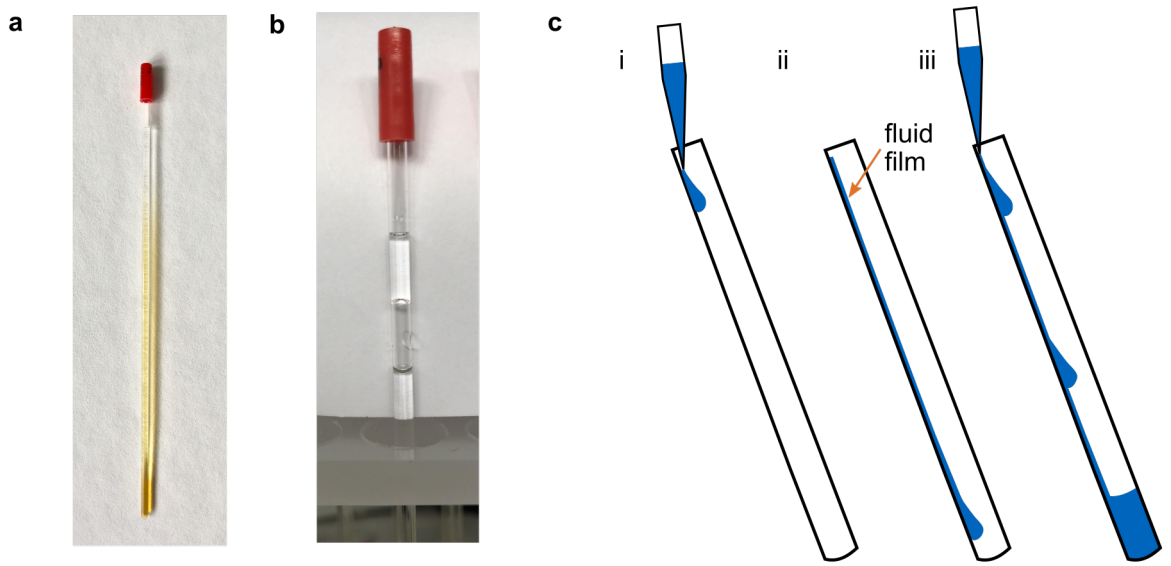

Figure 7.8: **a** NMR tubes with a diameter of 3 mm used for XRF experiments at the MuCLS; **b** NMR tube clogged with liquid; **c** Scheme for proper filling of NMR tubes: (i) First a single drop is injected into the tube. (ii) This drop glides to the bottom of the tube, leaving a fluid film on it (see orange arrow). (iii) Only after a fluid film has formed along the whole length of the tube, more liquid can be injected.

7.3.2 Experimental setup

The experimental setup for XRF, located in the first experimental endstation, is shown in Fig. 7.9. The sample tube is fastened onto a 3D-printed custom-designed sample holder mounted to a motorized linear stage. As mentioned earlier, the X-ray beam is adjusted to match the diameter of the sample, i.e., $3 \times 3\,\mathrm{mm}^2$ in size. The fluorescent signal of the sample is recorded with an energy-dispersive silicon drift detector (AXAS-D, Ketek GmbH, Germany) oriented at an angle of 90° to the incident X-ray beam. This geometry was chosen in order to minimize the Compton scattering signal reaching the detector (cf. Fig. 7.9b). The width of the Compton scattering peak was further reduced by filtering the initial spectrum with an aluminum plate, which absorbs part of the low energy tail of the spectrum before it reaches the sample. Additionally, a blend was placed in front of the detector with the aim to reduce the amount of Compton scatter from air that reaches the detector. However, this had no influence on the measured Compton scattering as it mainly arises from scattering within the sample. Therefore it travels through the blend on the same trajectory as the fluorescent X-rays.

Since the fluorescent signal of the samples, especially of those with very low concentrations, is relatively weak, the exposure time for each sample was 60 s. The acquired spectra were corrected for the absorption in air between sample and detector and for the transmission in the detector itself. Additionally, the background noise was subtracted from the spectrum. Afterwards, a Gaussian function was fitted to the K_α fluorescence peak of the element under investigation, taking into account the measurement uncertainties arising from Poisson noise. Next, the fitted curve was integrated to obtain the

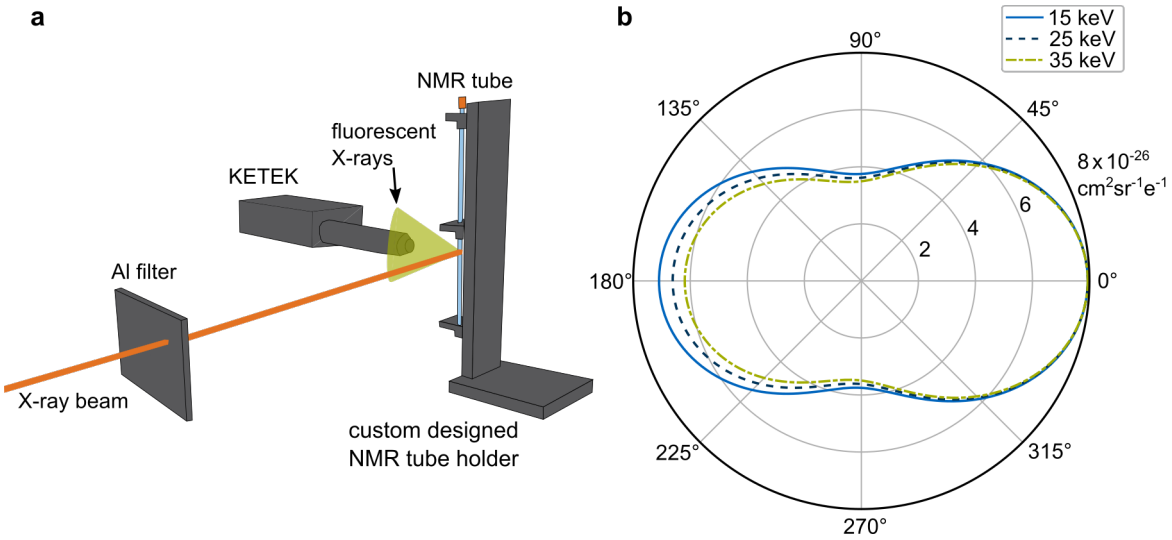

Figure 7.9: **a** Schematic of the XRF setup for element concentration determination in solutions; **b** Angular distribution of Compton scatter for X-radiation of 15 keV, 25 keV and 35 keV.

total intensity of the fluorescent peak. The uncertainty of the total intensity is considered to be the change in intensity arising from the uncertainty of the fit. To improve statistics, each spectrum was measured 5 times and an average of the 5 peak intensities was calculated. In order to level out changes in the X-ray flux, all spectra were flux corrected using the data from the scintillation counting device located upstream of the experimental setup. In the case of iodine, the fluorescent peak was overlaid with the Compton-scattered MuCLS spectrum. In order to extract the peak height of the fluorescent peak, Compton scattering by the sample was estimated using a measurement of an NMR-tube filled with pure water. This spectrum was subtracted from the measured XRF spectra of the iodine samples. For all other samples, the fluorescent peak was clearly separated from the Compton-scattered MuCLS spectrum.

Additionally, the absorption of the incident X-ray beam in the sample is estimated by acquiring X-ray images of the samples using the Hamamatsu sCMOS detector (type: C12849-101U). This enables estimation of the mean absorption coefficient μ and thus the self-absorption properties of the sample.

Correlation of fluorescence intensity and element concentration

The fluorescence intensity of an element in a sample in the experimental setup described above is given by Eq. 2.44 in Ch. 2.8.2. Depending on the element concentration, the formula can be simplified since the absorption properties of the element can be small or large in comparison to those of their solvent water. Since the bromine concentrations in the solutions are very high with concentrations between 0.5 mg/ml and 600 mg/ml ($500 - 600000$ ppm), the obtained fluorescent intensities were fitted with the whole formula that takes into account self-absorption of the fluorescent light by the sample

itself:

$$\frac{I_f}{I_0} = \omega \frac{\Delta\Omega}{4\pi} \frac{\mu_i(E)}{\mu_T(E) + \mu_T(E_f)} e^{-a\mu_T(E_f)d'} \left[1 - e^{-(\mu_T(E) - a\mu_T(E_f))d'}\right], \tag{7.1}$$

where $\mu_T(E/E_f) = \mu_w + \mu_i$, μ_w and μ_i being the absorption coefficient of water and the element of interest, respectively, at the X-ray energies of the exciting X-ray beam (E) and of the fluorescent X-rays (E_f), $a = \frac{\sin(\gamma)}{\sin(\delta)}$ and $d' = d/\sin(\gamma)$.

For all other elements, the elemental concentrations were significantly lower, ranging from 0.25µg/ml to 1000 µg/ml (or equivalently 0.5 to 1000 ppm). Accordingly, self-absorption of the fluorescent light by the element of interest is negligible. Therefore, $\mu_T \approx \mu_w$ and the fluorescent signal becomes linearly dependent on μ_i with

$$\begin{aligned} \frac{I_f}{I_0} &= \omega \frac{\Delta\Omega}{4\pi} \frac{1}{\mu_w(E) + \mu_w(E_f)} e^{-a\mu_w(E_f)d'} \left[1 - e^{-(\mu_w(E) - a\mu_w(E_f))d'}\right] \mu_i(E) \\ &= \text{const.} \cdot \mu_i(E). \end{aligned} \tag{7.2}$$

All measured concentration rows were fitted with one of the two equations. For the lower part of the concentration row of bromine, Eq. 7.2 could have also been used, but for simplicity only the equation that describes the total concentration row was used. To determine the elemental concentration in an unknown sample, the intensity of the fluorescent signal was calculated as described above. Then the intensity was inserted into the fitting curve to obtain the corresponding concentration. The uncertainty of the concentration was determined by error propagation, taking the same uncertainties into account as for the measured concentration rows.

7.3.3 Uncertainty of concentration of mixed solutions

The uncertainty in the concentration of the measured elemental solutions was estimated from two measurement series. In the first one, five sample tubes filled with the identical solution containing 150 µg/ml of silver were measured (P series). In the second series, five sample tubes containing solutions with a silver concentration of 150 µg/ml that were mixed separately were compared (M series). All samples were placed in the experimental setup described above and their fluorescent signals were evaluated according to the procedure described in the preceding paragraph. The concentrations of the samples were obtained by determining the position of the fluorescent intensity on the calibration curve determined using the silver concentration row. Fig. 7.10 shows the measured fluorescent signals against the associated concentrations. For both measurement series, the determined concentrations coincide with the actual concentration of the solutions. There is no significant difference between the two series.

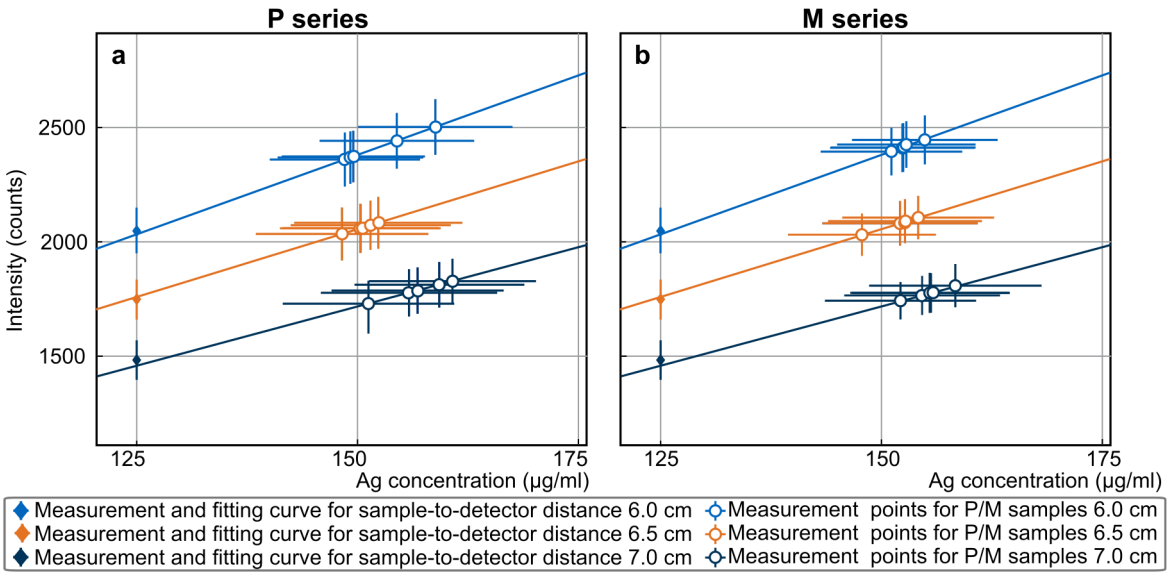

Figure 7.10: Uncertainty of the XRF signal for samples with the same concentrations of 150 µg/ml. **a** Fluorescent signals for samples filled with identical solution (P series); **b** Fluorescent signals for samples with same concentration but mixed separately.

For each measurement series, a weighted average of the concentration was calculated according to Eq. 6.1 and 6.2 in Ch. 6.6.1. It can be seen that the average concentrations for both series are identical and the uncertainties are very similar (cf. Table 7.3). The weighted average concentration for all distances was calculated to be (152.8±0.3) µg/ml for the P series and (152.3 ± 0.3) µg/ml for the M series. This indicates that the accuracy of the concentration is independent of the mixing procedure or that this error is significantly smaller than the measurement uncertainty of the setup.

series	distance	weighted average of concentration	uncertainty
P	6.0 cm	151.81 µg/ml	3.77 µg/ml
	6.5 cm	150.47 µg/ml	4.12 µg/ml
	7.0 cm	156.72 µg/ml	4.33 µg/ml
M	6.0 cm	151.94 µg/ml	3.72 µg/ml
	6.5 cm	150.87 µg/ml	3.97 µg/ml
	7.0 cm	154.32 µg/ml	4.12 µg/ml

Table 7.3: Weighted averages of the silver concentration from XRF-measurements in the uncertainty estimation series. The formulas for the calculation of the weighted average and its uncertainty can be found in Ch. 6.6.1 (Eq. 6.1 and 6.2).

7.3.4 XRF results of concentration rows

Iodine

When performing XRF measurements of the iodine samples, they are illuminated with the highest energy spectrum available at the MuCLS, i.e., one with a peak energy of 35 keV. Since the iodine concentrations in the samples are relatively low, the contribution from Compton scattering to the fluorescent signal, which overlaps with the K_α fluorescence peak of iodine at around 28.5 keV, is non-negligible. This can be seen in Fig. 7.11a. Nonetheless, it was possible to extract the fluorescent peak intensities for almost all iodine concentrations (cf. Fig. 7.11b). However, for concentrations of below 150 µg/ml, i.e., 150 ppm, the fitting of the fluorescent peak and thus the calculation of the peak intensity becomes inaccurate due to the high noise level in the data.

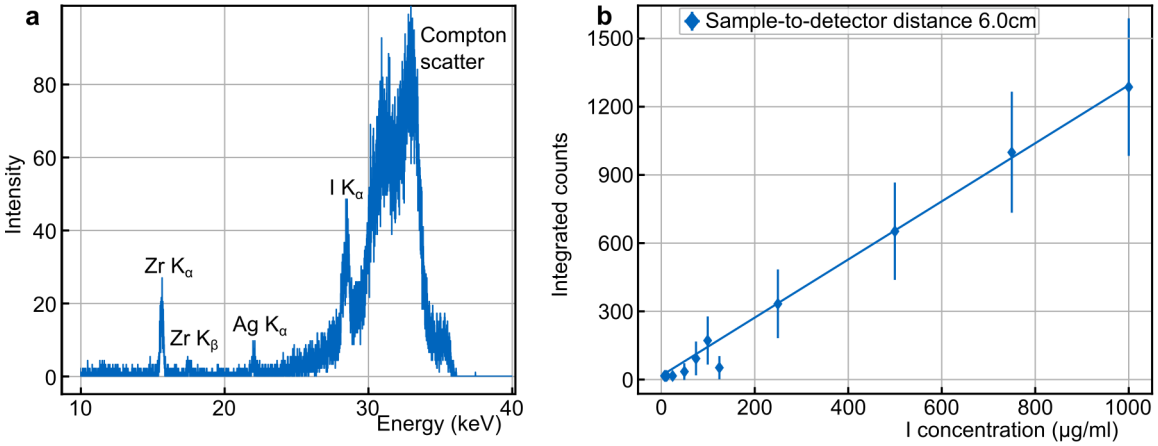

Figure 7.11: **a** Zoom into the XRF spectrum obtained from a sample containing 1 000 µg/ml iodine. The fluorescent peak is overlaid by Compton scattered X-ray photons; **b** Integrated peak heights plotted for different concentrations of iodine in the sample.

Silver

When illuminating the silver samples with an X-ray energy of 35 keV, the peak of the Compton scattered MuCLS spectrum is clearly separated from the silver K_α-line at around 22 keV. However, silver is a material that is often used in the electronics of detectors. Thus, the acquired spectra also exhibit a small silver peak when there is no silver in the sample. Therefore, the silver peak of the detector itself has to be subtracted from the fluorescent peak of the samples. To this end, several samples only containing water were measured and an average silver peak intensity was calculated based on them. Subtracting it from the fluorescent peaks in the sample measurements yields the fluorescent signal solely arising from the sample. Generally, the silver peak height in measurements without silver samples was constant. Consequently, a simple subtraction allows for accurate evaluation of the fluorescence signal of the silver samples. Fig. 7.12a shows the silver peak of the XRF measurement of the 1000 µg/ml sample including

the silver peak from the detector and the sample. The silver fluorescence corrected for detector contributions was evaluated for all silver concentrations, and the integral intensity of the peak was plotted in Fig. 7.12b. Since the silver peaks had very high intensities, the error bars in the plot are so small that their extend is approximately the size of the symbol in the plot. The intensity of the peak depends linearly on the silver concentration in the sample. Even for low sample concentrations the fit is still very accurate, but the actual peak intensity for concentrations below 10 µg/ml, i.e., 10 ppm, is lower than the fit suggests.

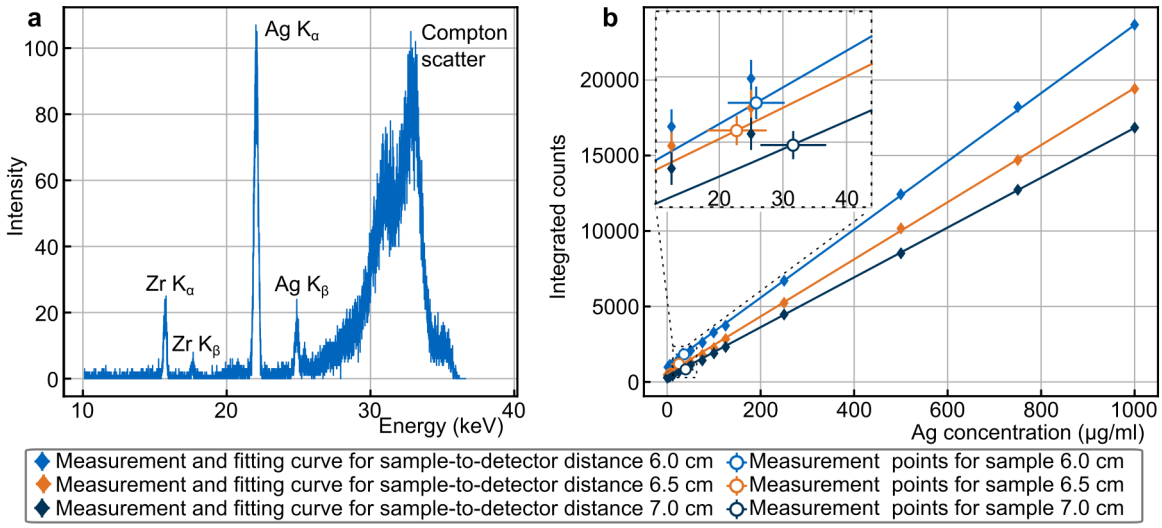

Figure 7.12: **a** Zoom into the XRF spectrum obtained from a sample containing 1 000 µg/ml of silver. The fluorescent peak is clearly separated from the one of Compton scattered X-ray photons. However, silver in the electronics of the detector contributes to the silver peak by a small amount. This peak was subtracted before determining the peak intensity for every sample concentration; **b** Fluorescent peak intensities plotted against the concentration of silver in the sample. Even for small silver concentrations the fit agrees well with the acquired data. In the inset, the calculated concentration for the measured intensities of the unknown sample can be seen.

To simulate the measurement of an unknown wet tissue sample, an additional tube was filled with a silver solution containing a concentration (30 µg/ml) different from the ones used for the calibration curve. The measured concentration of the sample was determined by extracting the concentration from the calibration curve for the measured fluorescence intensity. The results are depicted in the inset in Fig. 7.12b. For sample-to-detector distances of 6 cm and 7 cm, the measured concentration agrees with the actual concentration of the sample. However, for the third distance, the concentration was underestimated. The weighted average was calculated to be 26.4 ± 2.7 µg/ml, which is slightly below the actual concentration of the sample. For such small concentrations, the uncertainty of the measured intensity is relatively high. Therefore, it is not very surprising that the concentration could not be determined exactly.

Bromine

The incident X-ray beam illuminating the bromine solutions is almost completely absorbed by the sample. As a consequence, no Compton scattered radiation is present in the measured spectra. In Fig. 7.13a, the bromine K_α- and K_β-peaks can clearly be identified and their intensities are much higher compared to the fluorescent peaks of all the other measured elements. However, the intensities of the fluorescent peaks are not proportional to the elemental concentration (cf. Fig. 7.13b). Especially for concentrations higher than 400 mg/ml, the peak intensity drops compared to the lower concentrations. This can be explained by the self-absorption of the fluorescent signal by bromine particles in the sample. This process becomes more probable when the concentration of the particles in the sample increases.

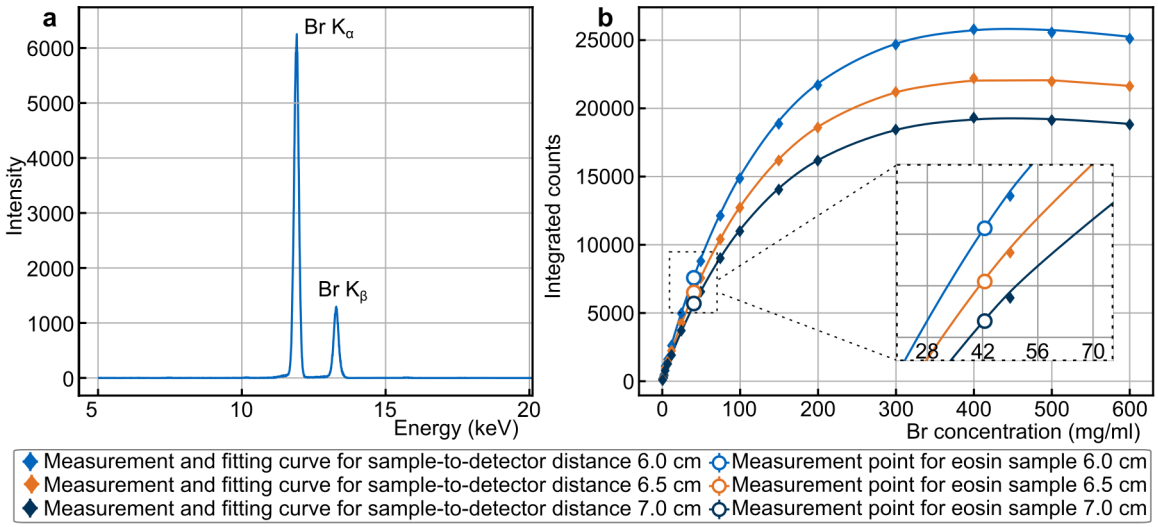

Figure 7.13: **a** Zoom into the XRF spectrum obtained from a sample containing 600 mg/ml of bromine. The absorption in the sample is so strong that the contribution by Compton scattered X-radiation is negligible; **b** Fluorescent peak intensities plotted against the concentration of bromine in the sample. Since the concentrations are very high, the fluorescent signal is partially absorbed by the sample itself. In the inset, the calculated concentration for the measured intensities of the stained eosin sample can be seen.

In the development of new staining methods, the determination of the amount of contrast agent that accumulates in the sample is difficult. Concentration determination from the fluorescence signal could overcome this issue. Therefore, the fluorescent signal of a tissue sample stained with eosin (a contrast agent containing a bromine complex) was measured and the bromine concentration was determined according to the scheme described above. The result can be seen in the inset in Fig. 7.13b. The error bars of the retrieved concentrations are even smaller than the size of the symbol. The weighted average was calculated to be 43.5 ± 0.1 mg/ml. The uncertainty of the calculated concentration is very low due to the very high intensity of the fluorescent signal. The determined concentration is in the expected range. However, no independent measurement method was available to verify the result. Nonetheless, this method provides a

good estimation of the sample concentration. It should be mentioned that the concentrations determined for the other elements, for which independent tests were available, agreed very well with the ones retrieved from the fluorescence signal, and thus the real bromine concentration is expected to be very similar to the value retrieved here.

Zinc

Fig. 7.14a shows the measured fluorescent spectrum of a solution containing 1 000 µg/ml of zinc. The peaks are not disturbed by any other signal such as scattering. However, the signal strength is rather weak and is therefore relatively noisy. Since the sample containers are made of glass, the fluorescent signal is partially absorbed by them. This loss in intensity can be corrected for by estimating the absorption in glass, but this amplifies the noise as well. The retrieved intensities and the calibration curve for zinc can be seen in Fig. 7.14b. The dependency of the fluorescent intensity on the concentration is linear although the signals for 1 000 µg/ml and 750 µg/ml are slightly off the curve.

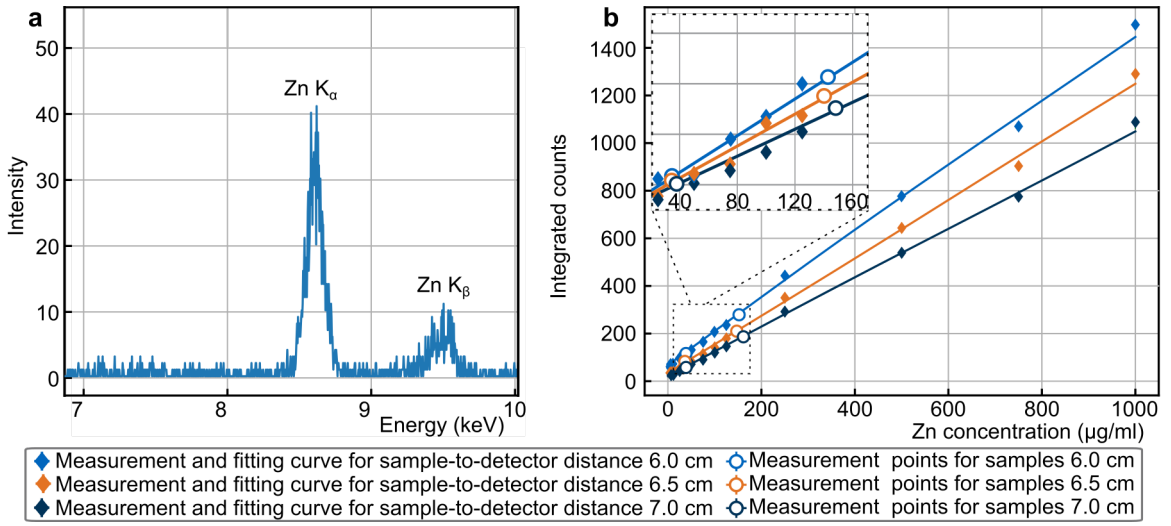

Figure 7.14: XRF signal of zinc for different concentrations as well as two unknown samples. **a** Zoom into the XRF spectrum obtained from a of sample containing 1 000 µg/ml of zinc; **b** Integrated intensities of the fluorescent line plotted against the concentration of zinc in the sample. The two samples containing unknown concentrations are marked with a circle. The inset shows a zoom into the concentrations with these samples.

Two additional tubes were filled with zinc solutions with different concentrations (36 µg/ml and 149 µg/ml). The results can be seen in the inset in Fig. 7.14b. For the higher concentrated sample, the measured concentration agreed with the actual concentration when the sample-to-detector distance is 7 cm. For the smaller distances, the concentration was underestimated. The weighted average of the retrieved concentration is 143.4 ± 0.9 µg/ml, which is lower than the actual concentration of the sample. The same is true for the sample with the smaller concentration, for which only the concentration measured at a distance of 7 cm agrees with the actual concentration and the

ones at the other two distances were underestimated. However, the weighted average concentration results in $35.2 \pm 0.6\,\mu g/ml$, which is only slightly lower than the actual concentration. Generally, the concentrations of the two samples were underestimated. The reason for this could be the uncertainty of the zinc fitting curve due to the large underground signal or to the relatively low fluorescent signal of zinc in general.

Iron

The iron solutions were measured in the PP sample tubes since their fluorescent signal was almost completely absorbed in the glass wall of the NMR tubes due to their low X-ray energy of about 6.4 keV. In addition to the K-peaks of iron contained in the sample solution, zinc peaks originating from the sample container are also visible in the measured spectra depicted in Fig. 7.15a. For small iron concentrations, the zinc signal was even larger than the one from iron. However, since they are well separated in energy, this did not disturb the evaluation of the iron peaks. Fig. 7.15b shows a linear dependence between fluorescent signal and elemental concentration in the sample. The large amount of Compton-scattered radiation limited the sample-to-detector distance in this case as well and in turn the measurement accuracy for lowly concentrated samples. For concentrations of $< 20\,\mu g/ml$, noise dominated the measured signal. Accordingly, the linear relation between signal strength and concentration breaks down.

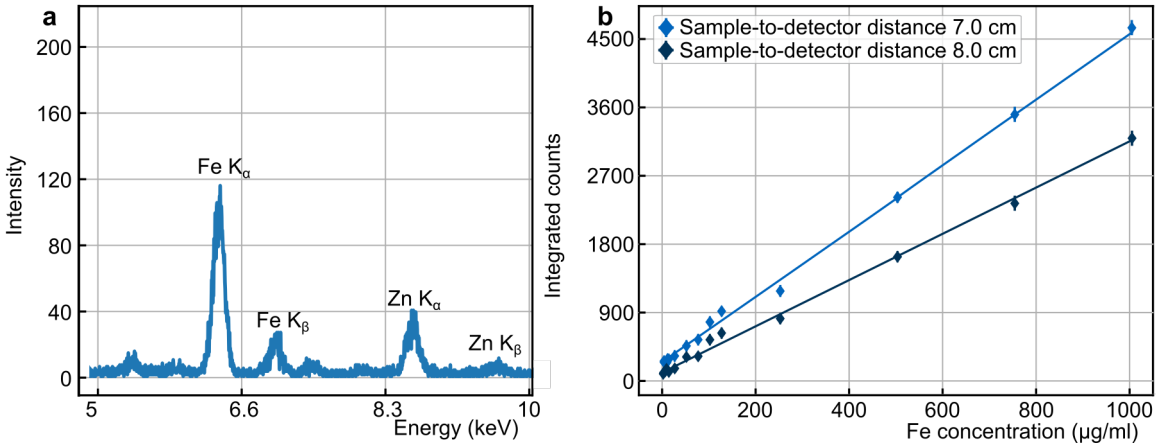

Figure 7.15: **a** Zoom into the XRF spectrum obtained from a sample containing 1 000 µg/ml of iron. Next to the iron signal, a zinc signal from the plastic sample containers is visible as well; **b** Integrated intensities of the fluorescent line plotted over the concentration of iron in the sample.

7.3.5 Discussion

The correlation of elemental concentration and fluorescent intensity has been shown for low concentrated samples as well as samples with higher elemental concentrations of up to 600 000 ppm. For samples with high sample concentrations, the fluorescent signal has a non-linear correlation with the elemental concentration. This can be explained by the absorption of the fluorescent signal in the sample. Since the elemental concentration in the sample is very high, the fluorescent light has a non-negligible probability of being re-absorbed. Therefore, the fluorescent signal will reach a maximum before decreasing for higher sample concentrations. Samples with low concentrations exhibit a linear dependency of the fluorescent intensity on the concentration. However, the measurement and fitting accuracy for the lowest concentrations was compromised by the large sample-to-detector distance and the amount of Compton scatter, leading to a saturation of the detector, prohibiting a smaller distance between sample and detector.

For several elements the concentration of a liquid or tissue sample was determined from the calibration curves derived from the concentration rows. The measured concentrations of the liquid samples of silver and zinc were slightly below the actual concentrations of the samples. However, the concentrations were smaller than 150 µg/ml (150 ppm) and thus their fluorescent signals were relatively low. A potential application of XRF is investigating the elemental concentrations in real tissue or biopsy samples to obtain information about their health state. In this case, the differences in concentration between healthy and cancerous tissue are significantly larger than the deviations experienced here ($\sim$ 1018 µg/g in healthy vs. $\sim$ 146 µg/g in cancerous prostate tissue [Zaichick, 1997]). Additionally, a tissue sample stained with eosin was investigated for its bromine content. The bromine concentration was determined to be 43.5 ± 0.1 mg/ml. Although there was no independent method to verify the calculated concentration, the good agreement of all three concentrations from different measurement distances indicates that this could be the actual concentration. For future studies, samples with known concentrations should be studied to determine the measurement accuracy for highly concentrated samples.

To further evaluate low sample concentrations, a smaller sample-to-detector distance has to be chosen. Although this will increase the fluorescent signal (as it's intensity is proportional to $1/r^2$), this will also increase the amount of Compton scattered radiation reaching the detector. Since these photons travel on the same trajectory as the fluorescent signal, they cannot be filtered from the radiation hitting the detector. Eventually, the amount of Compton scattered photons will limit the detection ability of the detector since its intensity is significantly higher than the one of the fluorescent signal. The dead time of the detector will increase and therefore the measurement of the XRF signal will become inaccurate.

These experiments showed that it is possible to determine the elemental concentration in a tissue sample using an appropriate calibration series. XRF could therefore be employed to discriminate between normal and pathological tissue according to the concentration of certain trace elements discovered in the biopsies. This can be useful

in diagnostics of diseases. Furthermore, it would be interesting to integrate the focusing setup introduced in Ch. 7.1.2 into this XRF-setup to determine whether a smaller beam size changes the detection limit of elements and to map out elemental distributions in the sample. XRF maps could be used to measure spatial micro-distributions, which indicate elemental accumulation and changes in the tissue structure and health [Gherase, 2020].

In conclusion, this proof-of-principle study accurately determined the fluorescent signal from samples with different elemental concentrations. However, at small concentrations their correct retrieval was limited by a significant contribution of Compton-scattered X-radiation to the measured signal. In combination with an appropriate calibration series, this method could provide an indication about the elemental concentration in a biopsy and thus hint at possible diseases.

8 Conclusion and Outlook

The experiments performed for this thesis show that KES at a compact synchrotron source has the potential to provide a diagnostic benefit for future clinical applications. It enhances the contrast between surrounding tissue and contrast agent and produces images only showing the contrasted structures. Additionally, the method can be a solution for situations where a structure is contrasted such that it becomes inseparable from highly absorbing body structures like bones or calcifications. While the separation of iodine and calcium in projection imaging has been shown in previous studies, KES CT was applied at the MuCLS in the course of this thesis. Thereby, it was not only possible to distinguish the two materials but also to calculate CT volumes either showing iodine or calcium, thus completely separating the two materials. In addition, subtraction experiments of a dynamically changing sample were performed and the performance of KES compared to conventional temporal subtraction was evaluated. The CNR in the KES images was significantly higher compared to the non-subtraction images and between 14.9 % and 21.5 % higher than in the temporal subtraction images. Additionally, it was shown that KES imaging of dynamically moving objects can be performed with almost no artifacts when using KES in comparison to a temporal subtraction technique, where images are acquired with significant time difference. This will allow *in vivo* imaging in future applications and the use of KES in procedures where subtraction imaging was not possible until today.

To achieve this, the experimental setup could be optimized further. At the moment, only the detector with the inefficient silicon sensor can be triggered by the light barrier of the filter wheel. By using detectors containing a more efficient GadOx or CdTe sensor or scintillator, KES imaging could be performed with much lower acquisition times. This, in turn, gives the opportunity to increase the imaging rate further towards the 30 Hz frame rate that is used in clinical angiography. When using a higher frame rate, the advantage of KES compared to temporal subtraction will increase even further since the time difference between two acquired images decreases and thus motion artifacts are minimized.

Yet, the applicability of KES around the K-edge of iodine is limited due to it relatively low X-ray energy of 33.17 keV. At this energy, the absorption of the X-rays in the human body is very high and thus leads to a high absorbed dose. To enable KES imaging in a clinical setting, the maximum energy of the compact synchrotron X-ray source would have to be increased in combination with using a contrast agent with a higher K-edge energy. Theoretically, many high-Z elements with a higher K-edge energy than iodine could be used as contrast agents for KES. One possible candidate is gadolinium, which is today commonly used in magnetic resonance imaging (MRI). In the past, studies have shown that gadolinium contrast agent could also be used in X-ray imaging [Thomas, 2016; Hamersvelt, 2017], especially for patients with renal insufficiency

[Sam, 2003; Sayin, 2007]. The gadolinium K-edge is at 50.2 keV, which would allow for dose compatible KES imaging on the human body [Eggl, 2017]. Currently, the source used at the MuCLS has its X-ray energy limit at 35 keV. However, by decreasing the laser wavelength, higher X-ray energies would be possible at the MuCLS while keeping the small footprint of the source. Several projects developing sources based on inverse Compton scattering, such as ThomX [Variola, 2011], BriXS and STAR [Faillace, 2019], that will provide higher X-ray energies are ongoing. These sources utilize higher electron energies and in the case of ThomX a larger electron storage ring than at the MuCLS. At ThomX, which is under construction in Orsay, France and is expected to start operation in 2020, KES at higher energies will be possible. KES experiments for the determination of contrast agent concentrations are already being planned [Variola, 2011]. Since the source provides an X-ray beam with energies of up to 90 keV, it could also be used to test high-Z element drugs [Jacquet, 2014; Variola, 2014] as possible contrast agents for KES. Paternò et al. [Paternò, 2019] evaluated the application of KES at an ICS using simulations based on STAR, which is a source currently under commissioning at the University of Calabria [Bacci, 2016; Faillace, 2019], and on the beam parameters of the "Marix" project. This simulation study produced very promising results for the use of KES for angiography in the future. With these ongoing developments of inverse Compton sources, KES has the potential to become dose compatible, and its application in clinically more relevant energy regimes will become possible.

XRF is another imaging technique that could profit from the monochromatic beam of a compact synchrotron source. XRF imaging was performed in the course of this thesis for different applications. This imaging method is commonly applied to degraded cultural heritage objects in order to reconstruct their original state and obtain information about their making. The X-ray beam at the MuCLS had to be focused to allow for XRF scanning of a degraded daguerreotype. While a small focus was achieved, it was not possible to reconstruct the original image of the daguerreotype from the fluorescence signal. Unfortunately, the mercury layer forming the image on the sample surface was too thin to produce a fluorescent signal strong enough to measure it within appropriate measurement time. A single row of the sample was reconstructed, but the measurement of the complete image would have taken several days rather than the several hours needed for a similar measurement at a synchrotron. Additionally, XRF at the MuCLS was used for biomedical imaging. XRF of tissue samples or biopsies can help to provide information about their state of health. The obtained results show that the measured fluorescent signals had good agreement with the theoretical dependence on the elemental concentrations. While there was a linear dependence of elemental concentration and fluorescent signal for low concentrations, self-absorption of the fluorescent X-rays in the sample played a big role for higher concentrations. It was possible to determine the elemental concentration of a stained tissue sample, which suggests that it could also be possible to distinguish cancerous and healthy biopsy samples in future experiments.

In the future, XRF could be used at the MuCLS to determine the concentrations of elements of biological interest in tissue samples, e.g., breast or prostate tissue, and

give an indication about the tissue's state of health. Since various diseases have an impact on elemental concentrations in different tissue types, degenerative diseases like Alzheimer's or Parkinson's or contamination through environmental influences could also be investigated using XRF. Additionally, XRF mapping of tissue samples could be performed using a focusing optics to achieve a small pixel size or by closing down the beam with a slit system. The latter could be of interest for incident X-ray energies higher than 25 keV since the available focusing optic is less efficient for higher energetic X-rays. Furthermore, developments of the imaging setup are needed in order to increase the sensitivity of the system. At the moment, the detection of low element concentrations is limited by the high amount of Compton scattering in the sample. Since this scattering is on-axis with the fluorescent light, it cannot be filtered properly. However, the use of a detector optimized for XRF imaging could possibly reduce this issue and additionally increase the detection of very weak fluorescent signals. At the moment, the detectability of high-Z elements is limited due to the fact that the X-ray energy is not high enough to excite the K-edge electrons of these elements. The intensity of the fluorescent L-lines is considerably lower than the intensity of the K-lines. This limits the ability to clearly detect elements like lead, mercury or gold and identify small changes in their concentration. An increase in the X-ray energy at the MuCLS would allow for the detection of very small concentrations of these and other high-Z elements. Additionally, the increase in X-ray energy could make new applications for XRF available and enable XRF of cultural heritage objects, which is limited to high flux synchrotron facilities at the moment.

All in all, both investigated imaging procedures show great potential for applications in a clinical context. However, further developments of both inverse Compton sources and contrast agents are needed to make KES dose compatible. The maximum energy of the MuCLS limits the ability to detect high-Z elements with XRF as well as the application of contrast agent with higher K-edge energies in KES. With further development of the imaging setups and by increasing the maximum energy of the MuCLS, these imaging techniques could take the next step in becoming part of pre-clinical research and potentially of clinical diagnostics.

Bibliography

[Achenbach, 2010] Stephan Achenbach et al. "Coronary computed tomography angiography with a consistent dose below 1 mSv using prospectively electrocardiogram-triggered high-pitch spiral acquisition". In: *European Heart Journal* 31 (2010), pp. 340–346 (Cited on page 11).

[Achterhold, 2013] K. Achterhold et al. "Monochromatic computed tomography with a compact laser-driven X-ray source". In: *Scientific reports* 3 (2013), p. 1313 (Cited on pages 2, 35, 60).

[Adams, 1973] Douglass F. Adams, David B. Fraser, and Herbert L. Abrams. "The Complications of Coronary Arteriography". In: *Circulation* 48 (1973), pp. 609–618 (Cited on page 51).

[Ahlgren, 1976] L. Ahlgren, K. Lidén, S. Mattsson, and S. Tejning. "X ray fluorescence analysis of lead in human skeleton in vivo". In: *Scandinavian Journal of Work, Environment and Health* 2.2 (1976), pp. 82–86 (Cited on page 102).

[AIC, 1994] AIC. *AIC Code of Ethics and Guidelines for Practice*. Tech. rep. 1994, p. 11 (Cited on page 89).

[Akagi, 2016] T. Akagi et al. "Narrow-band photon beam via laser Compton scattering in an energy recovery linac". In: *Physical Review Accelerators and Beams* 19 (2016), pp. 1–17 (Cited on page 2).

[Al-Ebraheem, 2009] A. Al-Ebraheem, M.J. Farquharson, and E. Ryan. "The evaluation of biologically important trace metals in liver, kidney and breast tissue". In: *Applied Radiation and Isotopes* 67.3 (2009), pp. 470–474 (Cited on page 101).

[Als-Nielsen, 2011] J. Als-Nielsen and D. McMorrow. *Elements of modern X-ray physics*. Second. John Wiley and Sons, Ltd, 2011 (Cited on pages 3, 15, 16, 22, 25, 27, 29–31).

[Androsov, 2010] V. Androsov et al. "Status of NESTOR facility". In: *IPAC 2010 - 1st International Particle Accelerator Conference, Kyoto, Japan*. Vol. WEPEA063. 2010, pp. 2630–2632 (Cited on page 39).

[Arhatari, 2017] Benedicta D. Arhatari, Timur E. Gureyev, and Brian Abbey. "Elemental Contrast X-ray Tomography Using Ross Filter Pairs with a Polychromatic Laboratory Source". In: *Scientific Reports* 7 (2017), p. 218 (Cited on pages 44, 59).

[Attwood, 1999] D. Attwood. *Soft X-rays and Extreme Ultraviolet Radiation: Principles and Applications*. Cambridge University Press, 1999 (Cited on page 3).

[Bacci, 2016] A. Bacci et al. "Status of the STAR Project". In: *Proceedings of IPAC2016, Busan, Korea*. Vol. TUPOW004. 2016, pp. 1747–1750 (Cited on pages 2, 38, 78, 116).

[Balewski, 2004] K. Balewski, W. Brefeld, W. Decking, H. Franz, and E. Weckert. *PETRA III: A Low Emittance Synchrotron Radiation Source Technical Design Report*. Tech. rep. Hamburg, Germany: DESY, 2004, p. 558 (Cited on page 38).

[Barger, 1995] M. Susan Barger and William B. White. *The Daguerreotype: Nineteenth-Century Technology and Modern Science*. Baltimore: Johns Hopkins University Press, 1995, p. 252 (Cited on pages 89–91).

[Bayat, 2001] S. Bayat et al. "Quantitative functional lung imaging with synchroton radiation using inhaled xenon as contrast agent". In: *Physics in Medicine and Biology* 46 (2001), pp. 3287–3299 (Cited on page 13).

[Bayat, 2006] Sam Bayat et al. "Differences in the time course of proximal and distal airway response to inhaled histamine studied by synchrotron radiation CT". In: *Journal of Applied Physiology* 100 (2006), pp. 1964–1973 (Cited on page 13).

[Bayat, 2013] Sam Bayat et al. "Effect of positive end-expiratory pressure on regional ventilation distribution during mechanical ventilation after surfactant depletion". In: *Anesthesiology* 119.1 (2013), pp. 89–100 (Cited on page 13).

[Bechara, 2012] Boulos Bechara et al. "Contrast-to-noise ratio difference in small field of view cone beam computed tomography machines." In: *Journal of Oral Science* 54.3 (2012), pp. 227–232 (Cited on page 9).

[Beckhoff, 2006] B. Beckhoff, B. Kanngieser, N. Langhoff, R. Wedell, and H. Wolff. *Handbook of Practical X-Ray Fluorescence Analysis*. Springer-Verlag Berlin Heidelberg, 2006, p. 863 (Cited on pages 22, 23).

[Bentzon, 2014] Jacob Fog Bentzon, Fumiyuki Otsuka, Renu Virmani, and Erling Falk. "Mechanisms of Plaque Formation and Rupture". In: *Circulation Research* 114 (2014), pp. 1852–1866 (Cited on page 56).

[Bertrand, 2005] Bernard Bertrand et al. “Comparison of synchrotron radiation angiography with conventional angiography for the diagnosis of in-stent restenosis after percutaneous transluminal coronary angioplasty”. In: *European Heart Journal* 26.13 (2005), pp. 1284–1291 (Cited on pages 13, 78).

[Bille, 2002] J. Bille and W. Schlegel. *Medizinische Physik 2*. 1st ed. Springer-Verlag Berlin Heidelberg, 2002 (Cited on pages 4, 7, 9).

[Boone, 1999] John M. Boone. “Glandular breast dose for monoenergetic and high-energy x-ray beams: Monte Carlo assessment”. In: *Radiology* 213.1 (1999), pp. 23–37 (Cited on page 8).

[Boone, 2002] John M. Boone. “Normalized glandular dose (DgN) coefficients for arbitrary x-ray spectra in mammography: Computer-fit values of Monte Carlo derived data”. In: *Medical Physics* 29.5 (2002), pp. 869–875 (Cited on page 8).

[Brody, 1982] William R Brody. “Digital Subtraction Angiography”. In: *IEEE Transactions on Nuclear Science* 29.3 (1982), pp. 1176–1180 (Cited on page 11).

[Bunker, 2010] Grant Bunker. “3 Experimental”. In: *Introduction to XAFS: A Practical Guide to X-ray Absorption Fine Structure Spectroscopy*. Cambridge University Press, 2010. Chap. 3, pp. 36–105 (Cited on page 22).

[Camara Neiva, 2014] Augusto Camara Neiva, Marli A. Marcondes, Herbert Prince Favero Pinto, and Paula Aline Durães Almeida. “Analysis of photographs and photo-paintings by energy-dispersive X-ray fluorescence spectroscopy”. In: *Radiation Physics and Chemistry* 95 (2014), pp. 378–380 (Cited on pages 89, 90).

[Carroll, 2003a] Frank E. Carroll, Marcus H. Mendenhall, Robert H. Traeger, Charles Brau, and James W. Waters. “Pulsed Tunable Monochromatic X-Ray Beams from a Compact Source: New Opportunities”. In: *American Journal of Roentgenology* 181.5 (2003), pp. 1197–1202 (Cited on page 13).

[Carroll, 2003b] Frank E. Carroll. “Tunable, monochromatic x-rays: An enabling technology for molecular/cellular imaging and therapy”. In: *Journal of Cellular Biochemistry* 90.3 (2003), pp. 502–508 (Cited on page 14).

[Centeno, 2011] Silvia A. Centeno, Franziska Schulte, Nora W. Kennedy, and Alejandro G. Schrott. “The formation of chlorine-induced alterations in daguerreotype image particles: A high resolution SEM-EDS study”. In: *Applied Physics A: Materials Science and Processing* 105 (2011), pp. 55–63 (Cited on page 90).

[Chappard, 2006] Christine Chappard et al. "Subchondral bone micro-architectural alterations in osteoarthritis: a synchrotron micro-computed tomography study". In: *OsteoArthritis and Cartilage* 14 (2006), pp. 215–223 (Cited on page 59).

[Chaytor, 2016] Richard J. Chaytor, Krishnamoorthy Rajbabu, Paul A. Jones, and Liam McKnight. "Determining the composition of urinary tract calculi using stone-targeted dual-energy CT: Evaluation of a low-dose scanning protocol in a clinical environment". In: *British Journal of Radiology* 89.1067 (2016) (Cited on page 68).

[Chi, 2017] Zhijun Chi et al. "Recent progress of phase-contrast imaging at Tsinghua Thomson-scattering X-ray source". In: *Nuclear Instruments and Methods in Physics Research Section B: Beam Interactions with Materials and Atoms* 402 (2017), pp. 364–369 (Cited on page 39).

[Chi, 2018] Zhijun Chi et al. "Experimental feasibility of dual-energy computed tomography based on the Thomson scattering X-ray source". In: *Journal of Synchrotron Radiation* 25.6 (2018), pp. 1797–1802 (Cited on page 39).

[Cho, 2012] Eun Suk Cho et al. "CT angiography of the renal arteries: Comparison of lower-tube-voltage CTA with moderate-concentration iodinated contrast material and conventional CTA". In: *American Journal of Roentgenology* 199.1 (2012), pp. 96–102 (Cited on page 68).

[Cooper, 2012] D. M.L. Cooper et al. "Three dimensional mapping of strontium in bone by dual energy K-edge subtraction imaging". In: *Physics in Medicine and Biology* 57 (2012), pp. 5777–5786 (Cited on pages 13, 78).

[Da Silva, 2010] Eric Da Silva, Mike Robinson, Christopher Evans, Ana Pejović-Milić, and Darrick V. Heyd. "Monitoring the photographic process, degradation and restoration of 21st century Daguerreotypes by wavelength-dispersive X-ray fluorescence spectrometry". In: *Journal of Analytical Atomic Spectrometry* 25 (2010), pp. 654–661 (Cited on page 90).

[Daguerre, 1839] L.-J.-M. Daguerre. *Historical and Descriptive Account of the Various Processes of the Daguerreotype and the Diorama*. London: Mc Lean, 1839 (Cited on page 89).

[Davis, 2016] Jeffrey M. Davis and Edward P. Vicenzi. "Optimizing compositional images of daguerreotype photographs using post processing methods". In: *Heritage Science* 4.14 (2016), pp. 1–8 (Cited on page 90).

[Deitrick, 2018] K. E. Deitrick, G. A. Krafft, B. Terzić, and J. R. Delayen. "High-brilliance, high-flux compact inverse Compton light source". In: *Physical Review Accelerators and Beams* 21 (2018), p. 080703 (Cited on page 34).

[Desai, 2010] Nikunj Desai, Abhinav Singh, and Daniel J. Valentino. "Practical evaluation of image quality in computed radiographic (CR) imaging systems". In: *SPIE Medical Imaging 2010: Physics of Medical Imaging*. Vol. 7622. 2010, 76224Q (Cited on page 9).

[DESY, 2018] DESY. *Photon Science DESY - PETRA III - Facility Information*. 2018 (Cited on page 38).

[Dik, 2008] Joris Dik et al. "Visualization of a Lost Painting by Vincent van Gogh Using Synchrotron Radiation Based X-ray Fluorescence Elemental Mapping". In: *Analytical Chemistry* 80.16 (2008), pp. 6436–6442 (Cited on page 89).

[Dilmanian, 1991] F. A. Dilmanian et al. "Computed tomography with monochromatic X-rays from the National Synchrotron Light Source". In: *Nuclear Instruments and Methods in Physics Research B* 56 (1991), pp. 1208–1213 (Cited on pages 13, 59).

[Dilmanian, 1997] F. A. Dilmanian et al. "Single- and dual-energy CT with monochromatic synchrotron x-rays". In: *Physics in Medicine and Biology* 42 (1997), pp. 371–387 (Cited on pages 13, 59, 68, 78).

[Dix, 1995] W.-R. Dix. "Intravenous coronary angiography with synchrotron radiation". In: *Progress in Biophysics and Molecular Biology* 63 (1995), pp. 159–191 (Cited on pages 13, 78).

[Dix, 2003] W. R. Dix et al. "Comparison of intravenous coronary angiography using synchrotron radiation with selective coronary angiography". In: *Journal of Synchrotron Radiation* 10.3 (2003), pp. 219–227 (Cited on pages 13, 44, 59).

[Dössel, 2016] O. Dössel. *Bildgebende Verfahren in der Medizin*. 2nd ed. Springer-Verlag Berlin Heidelberg, 2016, p. 537 (Cited on pages 10, 12).

[Durham, 2006] Troy R. Durham and Elizabeth T. Snow. "Metal Ions and carcinogenesis". In: *Cancer: Cell Structures, Carcinogens and Genomic Instability*. Ed. by Leon P. Bignold. Birkhäuser Verlag: Basel, Switzerland, 2006, pp. 97–130 (Cited on page 101).

[Egan, 2015] C. K. Egan et al. "3D chemical imaging in the laboratory by hyperspectral X-ray computed tomography." In: *Scientific reports* 5 (2015), p. 15979 (Cited on page 44).

[Eggl, 2016] Elena Eggl et al. "The Munich Compact Light Source: initial performance measures". In: *Journal of Synchrotron Radiation* 23.5 (2016), pp. 91–100 (Cited on pages 2, 31, 33, 35).

[Eggl, 2017] Elena Eggl et al. "Mono-Energy Coronary Angiography with a Compact Synchrotron Source". In: *Scientific Reports* 7 (2017), p. 42211 (Cited on pages 2, 14, 52, 53, 78, 116).

[Elad, 2006] Michael Elad and Michal Aharon. "Image Denoising Via Sparse and Redundant Representations Over Learned Dictionaries". In: *IEEE Transactions on Image Processing* 15.12 (2006), pp. 3736–3745 (Cited on page 74).

[Elleaume, 2000] H. Elleaume et al. "First human transvenous coronary angiography at the European Synchrotron Radiation Facility." In: *Physics in Medicine and Biology* 45.9 (2000), pp. L39–L43 (Cited on pages 1, 13, 44, 51, 78).

[Elleaume, 2002] H. Elleaume, A. M. Charvet, S. Corde, F. Estève, and J. F. Le Bas. "Performance of computed tomography for contrast agent concentration measurements with monochromatic x-ray beams : comparison of K-edge versus temporal subtraction". In: *Phys. Med. Biol.* 47 (2002), pp. 3369–3385 (Cited on pages 13, 51, 68, 78).

[Ene, 2010] Antoaneta Ene, Alina Boşneagă, and L. Georgescu. "Determination of heavy metals in soils using XRF technique". In: *Romanian Reports of Physics* 55.7-8 (2010), pp. 815–820 (Cited on page 102).

[Excillum AB, 2020] Excillum AB. *MetalJet X-ray sources*. 2020. URL: `https://www.excillum.com/products/metaljet/` (visited on 03/20/2020) (Cited on page 27).

[Faillace, 2019] Luigi Faillace et al. "Status of compact inverse Compton sources in Italy: BriXS and STAR". In: *Proc. SPIE 11110, Advances in Laboratory-based X-Ray Sources, Optics, and Applications VII, SPIE Optical Engineering + Applications,2019, San Diego, California, United States*. Vol. 1111005. 2019, p. 4 (Cited on pages 38, 116).

[Fessler, 2000] Jeffrey Fessler. "Statistical Image Reconstruction Methods for Transmission Tomography". In: *Handbook of Medical Imaging, Volume 2. Medical Image Processing and Analysis*. Ed. by J M Fitzpatrick and M Sonka. Bellingham, USA: SPIE Press, 2000, pp. 1–70 (Cited on pages 18, 19, 64).

[Gallardo, 2016] Helena Gallardo, Ignasi Queralt, Josefina Tapias, Lucila Candela, and Eva Margui. "Bromine and bromide content in soils: Analytical approach from total reflection X- ray spectrometry". In: *Chemosphere* 156 (2016), pp. 294–301 (Cited on page 102).

[Geraki, 2008] K. Geraki, M.J. Farquharson, D. A. Bradley, O. Gundogdu, and G. Falkenberg. "The localisation of biologically important metals in soft and calcified tissues using a synchrotron x-ray fluorescence technique". In: *X-Ray Spectrometry* 37 (2008), pp. 12–20 (Cited on page 101).

[Gherase, 2020] Mihai R. Gherase and David E.B. Fleming. "Probing Trace Elements in Human Tissues with Synchrotron Radiation". In: *Crystals* 10.12 (2020), pp. 1–24 (Cited on pages 1, 101, 114).

[Giacomini, 1998] J. C. Giacomini et al. "Bronchial imaging in humans using xenon K-edge dichromography". In: *Nuclear Instruments and Methods in Physics Research, Section A* 406 (1998), pp. 473–478 (Cited on page 13).

[Gianoncelli, 2018] Alessandra Gianoncelli, Clara Rizzardi, Damien Salomon, Vincenzo Canzonieri, and Lorella Pascolo. "Nano-imaging of environmental dust in human lung tissue by soft and hard X-ray fluorescence microscopy". In: *Spectrochimica Acta Part B: Atomic Spectroscopy* 147 (2018), pp. 71–78 (Cited on page 102).

[Golosio, 2012] Bruno Golosio et al. "Measurement of an inverse Compton scattering source local spectrum using k-edge filters". In: *Applied Physics Letters* 100.16 (2012) (Cited on page 13).

[Gradl, 2018] Regine Gradl et al. "In vivo Dynamic Phase-Contrast X-ray Imaging using a Compact Light Source". In: *Scientific Reports* 8.1 (2018), p. 6788 (Cited on page 82).

[Graham, 2004] S. A. Graham and J. M. O'Meara. "The feasibility of measuring silver concentrations in vivo with x-ray fluorescence". In: *Physics in Medicine and Biology* 49.15 (2004), N259–N266 (Cited on page 102).

[Graves, 2009] W. S. Graves, W. Brown, F. X. Kaertner, and D. E. Moncton. "MIT inverse Compton source concept". In: *Nuclear Instruments and Methods in Physics Research, Section A* 608 (2009), S103–105 (Cited on page 39).

[Graves, 2017] W. S. Graves et al. "Asu Compact XFEL". In: *38th International Free Electron Laser Conference* TUB03 (2017) (Cited on pages 2, 39).

[Gruberg, 2000] Luis Gruberg et al. “The Prognostic Implications of Further Renal Function Deterioration Within 48 h of Interventional Coronary Procedures in Patients With Pre-existent Chronic Renal Insufficiency”. In: *Journal of the American College of Cardiology* 36.5 (2000), pp. 1542–1548 (Cited on page 51).

[Günther, 2020] B. Günther et al. “The versatile X-ray beamline of the Munich Compact Light Source: Design, instrumentation and applications”. In: *Journal of Synchrotron Radiation* 27 (2020) (Cited on page 37).

[Hahn, 2014] Dieter Hahn. “Statistical Iterative Reconstruction for X-ray Phase-Contrast Computed Tomography”. PhD thesis. Technische Universität München, 2014 (Cited on page 19).

[Hamersvelt, 2017] Robbert W. van Hamersvelt et al. “Feasibility and accuracy of dual-layer spectral detector computed tomography for quantification of gadolinium: a phantom study”. In: *European Radiology* 27.9 (2017), pp. 3677–3686 (Cited on page 115).

[Hartung, 2011] Michael P. Hartung, Thomas M. Grist, and Christopher J. Fran- çois. “Magnetic resonance angiography: Current status and future directions”. In: *Journal of Cardiovascular Magnetic Resonance* 13.19 (2011), pp. 1–11 (Cited on page 11).

[Hemberg, 2003] O. Hemberg, M. Otendal, and H. M. Hertz. “Liquid-metal-jet anode electron-impact x-ray source”. In: *Applied Physics Letters* 83.7 (2003), pp. 1483–1485 (Cited on page 27).

[Henzler, 2012] Thomas Henzler, Christian Fink, Stefan O. Schoenberg, and U. Joseph Schoepf. “Dual-energy CT: Radiation Dose Aspects”. In: *American Journal of Roentgenology* 199.5 Suppl (2012), pp. 16–25 (Cited on page 68).

[Hippert, 2006] Françoise Hippert, Erik Geissler, Jean Louis Hodeau, Eddy Lelièvre-Berna, and Jean-René Regnard. *Neutron and X-ray Spectroscopy*. Springer, 2006, p. 566 (Cited on page 22).

[Hochmuth, 2002] Albrecht Hochmuth, Uwe Spetzger, and Martin Schumacher. “Comparison of three-dimensional rotational angiography with digital subtraction angiography in the assessment of ruptured cerebral aneurysms”. In: *American Journal of Neuroradiology* 23 (2002), pp. 1199–1205 (Cited on page 51).

[Houk, 1979] Theodore L Houk et al. “Real-Time Digital K-Edge Subtraction Fluoroscopy”. In: *Investigative Radiology* 14.4 (1979), pp. 270–278 (Cited on pages 1, 78).

[Hounsfield, 1973] G. N. Hounsfield. “Computerized transverse axial scanning (tomography): Part 1. Description of system”. In: *British Journal of Radiology* 46.522 (1973), pp. 1016–22 (Cited on page 58).

[Howard, 2012] Daryl L. Howard et al. "High-definition X-ray Fluorescence Elemental Mapping of Paintings". In: *Analytical Chemistry* 84 (2012), pp. 3278–3286 (Cited on page 89).

[Huang, 1998] Zhirong Huang and Ronald D. Ruth. "Laser-Electron Storage Ring". In: *Physical Review Letters* 80.5 (1998), pp. 976–979 (Cited on pages 2, 31, 78).

[Huber, 1964] Peter J. Huber. "Robust Estimation of a Location Parameter". In: *The Annals of Mathematical Statistics* 35.1 (1964), pp. 73–101 (Cited on page 19).

[Hughes, 1985] E. B. Hughes et al. "Prospects for non-invasive angiography with tunable X-rays". In: *Nuclear Instruments and Methods in Physics Research Section B: Beam Interactions with Materials and Atoms* 10-11.1 (1985), pp. 323–328 (Cited on page 13).

[IAEA, 2007] International Atomic Energy Agency (IAEA). *Dosimetry in Diagnostic Radiology: An Interantional Code of Practice*. Tech. rep. 2007, p. 372 (Cited on page 8).

[ICRP, 2012] ICRP. *ICRP Publication 119 - Compendium of Dose Coefficients based on ICRP Publication 60*. Tech. rep. 1. 2012, p. 130 (Cited on pages 7, 8).

[Ide-Ektessabi, 2002] A. Ide-Ektessabi, S. Fujisawa, K. Sugimura, Y. Kitamura, and A. Gotoh. "Quantitative analysis of zinc in prostate cancer tissues using synchrotron radiation microbeams". In: *X-Ray Spectrometry* 31 (2002), pp. 7–11 (Cited on pages 1, 101).

[IMV, 2017] International Marketing Ventures. *2017 CT Market Outlook Report*. Tech. rep. 2017, p. 140 (Cited on page 58).

[Iyengar, 1981] G. V. Iyengar. "Human Health and Trace Element Research: Problems and Prospects Trace". In: *The Science of the Total Environment* 19 (1981), pp. 105–109 (Cited on page 101).

[Jacobson, 1953] Bertil Jacobson. "Dichromatic Absorption Radiography. Dichromography". In: *Acta Radiologica* 39.6 (1953), pp. 437–452 (Cited on pages 13, 78).

[Jacquet, 2014] Marie Jacquet. "High intensity compact Compton X-ray sources: Challenges and potential of applications". In: *Nuclear Instruments and Methods in Physics Research, Section B* 331 (2014), pp. 1–5 (Cited on pages 2, 31, 32, 34, 38, 78, 116).

[Jacquet, 2015] Marie Jacquet and Pekka Suortti. "Radiation therapy at compact Compton sources". In: *Physica Medica* 31 (2015), pp. 596–600 (Cited on page 34).

[Jaklevic, 1977] J. Jaklevic et al. "Fluorescence detection of EXAFS: Sensitivity enhancement for dilute species and thin films". In: *Solid State Communications* 23.9 (1977), pp. 679–682 (Cited on page 22).

[Jepperson, 2014] Maria A. Jepperson et al. "In Vivo Comparison of Radiation Exposure of Dual-Energy CT Versus Low-Dose CT Versus Standard CT for Imaging Urinary Calculi". In: *Journal of Endourology* 29.2 (2014), pp. 141–146 (Cited on page 68).

[Kalender, 2006] Willi A. Kalender. "X-ray computed tomography". In: *Physics in Medicine and Biology* 51 (2006), R29–R43 (Cited on pages 58, 67).

[Klockenkämper, 1993] R. Klockenkämper, A. von Bohlen, L. Moens, and W. Devos. "Analytical characterization of artists' pigments used in old and modern paintings by total-reflection X-ray fluorescence". In: *Spectrochimica Acta Part B: Atomic Spectroscopy* 48B.2 (1993), pp. 239–246 (Cited on page 89).

[Klockenkämper, 2000] R. Klockenkämper, A. Von Bohlen, and L. Moens. "Analysis of Pigments and Inks on Oil Paintings and Historical Manuscripts Using Total Reflection X-ray Fluorescence Spectrometry". In: *X-Ray Spectrometry* 29 (2000), pp. 119–129 (Cited on page 89).

[Knez, 2001] Andreas Knez et al. "Usefulness of multislice spiral computed tomography angiography for determination of coronary artery stenoses". In: *American Journal of Cardiology* 88.10 (2001), pp. 1191–1194 (Cited on page 11).

[Kozachuk, 2018a] Madalena. S. Kozachuk, T. K. Sham, R. R. Martin, A. J. Nelson, and I. Coulthard. "Exploring tarnished daguerreotypes with synchrotron light: XRF and μ-XANES analysis". In: *Heritage Science* 6.12 (2018), pp. 1–12 (Cited on page 90).

[Kozachuk, 2018b] Madalena S. Kozachuk et al. "Recovery of Degraded-Beyond-Recognition 19th Century Daguerreotypes with Rapid High Dynamic Range Elemental X-ray Fluorescence Imaging of Mercury L Emission". In: *Scientific Reports* 8.9565 (2018), pp. 1–10 (Cited on pages 90, 97).

[Kozachuk, 2019] Madalena S. Kozachuk et al. "Recovering Past Reflections: X-Ray Fluorescence Imaging of Electrocleaned 19th Century Daguerreotypes". In: *Heritage* 2 (2019), pp. 568–586 (Cited on pages 89, 90).

[Krieger, 2012] H. Krieger. *Grundlagen der Strahlungsphysik und des Strahlenschutzes*. 4th ed. Springer Spektrum, 2012, pp. 318–387 (Cited on pages 7, 8).

[Kuhlmann, 2014] Inga Kuhlmann, Dawn Chin, and Gerald Rimbach. *Prävention kardiovaskulärer Erkrankungen und Atherosklerose*. Springer Spektrum essentials, 2014, p. 32 (Cited on page 56).

[Kulpe, 2018] Stephanie Kulpe et al. "K-edge subtraction imaging for coronary angiography with a compact synchrotron X-ray source". In: *PLoS ONE* 13.12 (2018), e0208446 (Cited on pages 41, 42, 52, 54, 55, 78, 86).

[Kulpe, 2019] Stephanie Kulpe et al. "K-edge Subtraction Computed Tomography with a Compact Synchrotron X-ray Source". In: *Scientific Reports* 9 (2019), p. 13332 (Cited on pages 58, 64–67, 78).

[Kulpe, 2020a] Stephanie Kulpe et al. "Dynamic K-edge Subtraction Fluoroscopy at a Compact Inverse-Compton Synchrotron X-ray Source". In: *Scientific Reports* 10 (2020), p. 9612 (Cited on pages 70, 79, 81, 84, 85).

[Kulpe, 2020b] Stephanie Kulpe et al. "K-edge subtraction imaging for iodine and calcium separation at a compact synchrotron x-ray source". In: *Journal of Medical Imaging* 7.2 (2020), p. 023504 (Cited on pages 52, 56, 57).

[Kump, 1996] P. Kump, M. Nečemer, and J. Šnajder. "Determination of trace elements in bee honey, pollen and tissue by total reflection and radioisotope X-ray fluorescence spectrometry". In: *Spectrochimica Acta - Part B Atomic Spectroscopy* 51 (1996), pp. 499–507 (Cited on page 102).

[Kuroda, 2011] R. Kuroda et al. "Quasi-monochromatic hard X-ray source via laser Compton scattering and its application". In: *Nuclear Instruments and Methods in Physics Research, Section A: Accelerators, Spectrometers, Detectors and Associated Equipment* 637.1 SUPPL. (2011), S183–S186 (Cited on pages 14, 38).

[Kuroda, 2014] R. Kuroda, Y. Taira, M. Yasumoto, H. Toyokawa, and K. Yamada. "K-edge imaging with quasi-monochromatic LCS X-ray source on the basis of S-band compact electron linac". In: *Nuclear Instruments and Methods in Physics Research Section B: Beam Interactions with Materials and Atoms* 331 (2014), pp. 257–260 (Cited on page 14).

[Layachi, 2013] Skander Layachi et al. "Role of cellular effectors in the emergence of ventilation defects during allergic bronchoconstriction". In: *Journal of Applied Physiology* 115 (2013), pp. 1057–1064 (Cited on page 13).

[Le Duc, 2000] G. Le Duc et al. “Feasibility of synchrotron radiation computed tomography on rats bearing glioma after iodine or gadolinium injection”. In: *European Radiology* 10 (2000), pp. 1487–1492 (Cited on pages 13, 68).

[Loewen, 2003] Roderick J. Loewen. “A Compact Light Source: Design and Technical Feasibility Study of a Laser-Electron Storage Ring X-ray Source”. PhD thesis. Standford University, 2003, p. 117 (Cited on pages 32, 37).

[Martin, 1851] Anton Martin. *Handbuch der Photographie oder Vollständige Anleitung zur Erzeugung von Lichtbildern auf Metall, Papier und auf Glas, Daguerreotypie, Talbotypie, Niepcotypie.* 2nd ed. Verlag von Carl Gerold, Wien, Österreich, 1851, p. 393 (Cited on pages 90, 91).

[Mechlem, 2018] Korbinian Mechlem et al. “Spectral Angiography Material Decomposition Using an Empirical Forward Model and a Dictionary-Based Regularization”. In: *IEEE Transactions on Medical Imaging* 37.10 (2018), pp. 2298–2309 (Cited on page 74).

[Meijering, 1999] Erik H. W. Meijering, Karel J. Zuiderveld, and Max A. Viergever. “Image Registration for Digital Subtraction Angiography”. In: *International Journal of Computer Vision* 31.2/3 (1999), pp. 227–246 (Cited on pages 10, 11, 51, 77).

[Menken, 1985] Matthew Menken, Gordon H DeFriese, Thomas R Oliver, and Irwin Litt. “Introduction to Digital Subtraction Angiography”. In: *The Cost effectiveness of digital subtraction angiography in the diagnosis of cerebrovascular disease.* DIANE Publishing, 1985, p. 56 (Cited on page 11).

[Mikla, 2014] Victor I. Mikla and Victor V. Mikla. “Advances in imaging from the first X-Ray images”. In: *Medical Imaging Technology.* 2014, pp. 559–570 (Cited on pages 7–9).

[Miller, 2006] Lisa M. Miller et al. “Synchrotron-based infrared and X-ray imaging shows focalized accumulation of Cu and Zn co-localized with β-amyloid deposits in Alzheimer’s disease”. In: *Journal of Structural Biology* 155 (2006), pp. 30–37 (Cited on pages 1, 101).

[Mino, 2005] Yoshiki Mino and Mayumi Yukita. “Detection of high levels of bromine in vegetables using X-ray fluorescence spectrometry”. In: *Journal of Health Science* 51.3 (2005), pp. 365–368 (Cited on page 102).

[Molen, 2004] Aart J. van der Molen, Henrik S. Thomsen, and Sameh K. Morcos. “Effect of iodinated contrast media on thyroid function in adults”. In: *European Radiology* 14 (2004), pp. 902–907 (Cited on page 51).

[Monard, 2018] H. Monard. *ThomX Status General Meeting*. Tech. rep. 2018 (Cited on page 38).

[Monfraix, 2005] Sylvie Monfraix et al. "Quantitative measurement of regional lung gas volume by synchrotron radiation computed tomography". In: *Physics in Medicine and Biology* 50 (2005), pp. 1–11 (Cited on page 13).

[Mowatt, 2008] G. Mowatt et al. "64-Slice computed tomography angiography in the diagnosis and assessment of coronary artery disease: Systematic review and meta-analysis". In: *Heart* 94 (2008), pp. 1386–1393 (Cited on page 11).

[Murrie, 2016] R. P. Murrie, D. M. Paganin, A. Fouras, and K. S. Morgan. "Phase contrast x-ray velocimetry of small animal lungs: optimising imaging rates". In: *Biomedical Optics Express* 7.1 (2016), pp. 79–92 (Cited on page 82).

[Nachaliel, 1992] E. Nachaliel et al. "Monochromatic computed tomography of the human brain using synchrotron X-rays: technical feasibility". In: *Nuclear Instruments and Methods in Physics Research Section A: Accelerators, Spectrometers, Detectors and Associated Equipment* 319.1-3 (1992), pp. 305–310 (Cited on pages 13, 59).

[Nakazawa, 2011] Emiko Nakazawa et al. "Silver speciation in liver of marine mammals by synchrotron X-ray absorption fine structure and X-ray fluorescence spectroscopies". In: *Journal of Environmental Monitoring* 13 (2011), pp. 1678–1686 (Cited on page 102).

[Niu, 2015] Kai Niu et al. "Ultra Low Radiation Dose Digital Subtraction Angiography (DSA) Imaging using Low Rank Constraint". In: *Medical Imaging 2015: Physics of Medical Imaging* 9412 (2015), 94121O (Cited on page 11).

[Okamoto, 2000] K. Okamoto, J. Ito, K. Sakai, and S. Yoshimura. "The Principle of Digital Subtraction Angiography and Radiological Protection". In: *Interventional Neuroradiology* 6 (2000), pp. 25–31 (Cited on page 11).

[Panahifar, 2016] Arash Panahifar, Nazanin Samadi, Treena M. Swanston, L. - Dean Chapman, and David M.L. Cooper. "Spectral K-edge subtraction imaging of experimental non-radioactive barium uptake in bone". In: *Physica Medica* 32 (2016), pp. 1765–1770 (Cited on page 13).

[Pani, 2012] Silvia Pani et al. "Optimization of K-edge subtraction imaging using a pixellated spectroscopic detector". In: *IEEE Nuclear Science Symposium Conference Record* (2012), pp. 3063–3066 (Cited on page 44).

[Pascolo, 2013] Lorella Pascolo et al. "The interaction of asbestos and iron in lung tissue revealed by synchrotron-based scanning X-ray microscopy". In: *Scientific Reports* 3.1123 (2013), pp. 1–11 (Cited on page 101).

[Paternò, 2019] G. Paternò et al. "Inverse Compton radiation: a novel x-ray source for K-edge subtraction angiography?" In: *Physics in Medicine and Biology* 64.18 (2019), p. 185002 (Cited on page 116).

[Pelz, 1985] David M. Pelz, Allan J. Fox, and Fernando Vinuela. "Digital Subtraction Angiography: Current Clinical Applications". In: *Stroke* 16.3 (1985), pp. 528–536 (Cited on pages 11, 13).

[Podorsak, 2006] Ervin B. Podorsak. *Radiation Physics for Medical Physicists*. 2nd ed. Springer-Verlag Berlin Heidelberg, 2006 (Cited on page 20).

[Pogorelsky, 2016] I. V. Pogorelsky. "Progress and Prospects of a Compton X-ray Source Driven by a High-Power CO2 Laser". In: *X-Ray Lasers 2014, Springer Proceedings in Physics*. Vol. 169. Springer International Publishing Switzerland, 2016, p. 133 (Cited on pages 20, 21, 39).

[Pogorelsky, 2000] I. V. Pogorelsky et al. "Demonstration of 8×10^{18} photons/second peaked at 1.8 Å in a relativistic Thomson scattering experiment". In: *Physical Review Special Topics - Accelerators and Beams* 3.090702 (2000), pp. 8–15 (Cited on page 39).

[Popescu, 2009] Bogdan F. Gh. Popescu et al. "Mapping metals in Parkinson's and normal brain using rapid-scanning x-ray fluorescence". In: *Physics in Medicine and Biology* 54 (2009), pp. 651–663 (Cited on pages 1, 101).

[Qu, 2015] Mingliang Qu et al. "Radiation dose reduction in dual-energy CT: Does it affect the accuracy of urinary stone characterization?" In: *American Journal of Roentgenology* 205.2 (2015), W172–W176 (Cited on page 68).

[Reinhold, 2014] Hillary A. Reinhold and Michele P. West. *Acute Care Handbook for Physical Therapists*. Ed. by Jaime C. Paz and Michelle P. West. 4th ed. Elsevier Health Sciences, 2014 (Cited on page 51).

[Roessl, 2007] E. Roessl and R. Proksa. "K-edge imaging in x-ray computed tomography using multi-bin photon counting detectors". In: *Physics in Medicine and Biology* 52 (2007), pp. 4679–4696 (Cited on pages 44, 59).

[Rubenstein, 1981] E. Rubenstein et al. "Synchrotron Radiation And Its Application to Digital Subtraction Angiography". In: *Proc. SPIE* 0314 (1981), p. 42 (Cited on pages 1, 13, 51).

[Rubenstein, 1986] E. Rubenstein et al. "Synchrotron Radiation for Transvenous Coronary Angiography". In: *Trans Am Clin Climatol Assoc.* 97 (1986), pp. 27–31 (Cited on pages 1, 13, 44, 51, 78).

[Ryan, 2014] C. G. Ryan et al. "Maia X-ray fluorescence imaging: Capturing detail in complex natural samples". In: *Journal of Physics: Conference Series* 499.1 (2014), p. 012002 (Cited on page 97).

[Sam, 2003] Albert D. Sam et al. "Safety of gadolinium contrast angiography in patients with chronic renal insufficiency". In: *Journal of Vascular Surgery* 38.2 (2003), pp. 313–318 (Cited on page 116).

[Sandstede, 1999] Jörn J. W. Sandstede et al. "Three-Dimensional MR Coronary Angiography Using the Navigator Technique Compared with Conventional Coronary Angiography". In: *American Journal of Roentgenology* 172 (1999), pp. 135–139 (Cited on page 11).

[Sarnelli, 2004] A. Sarnelli et al. "K-edge digital subtraction imaging based on a dichromatic and compact x-ray source". In: *Physics in Medicine and Biology* 49 (2004), pp. 3291–3305 (Cited on page 78).

[Sarnelli, 2006] A. Sarnelli, H. Elleaume, A. Taibi, M. Gambaccini, and A. Bravin. "K-edge digital subtraction imaging with dichromatic x-ray sources : SNR and dose studies". In: 51 (2006), pp. 4311–4328 (Cited on pages 47, 64).

[Sayin, 2007] T. Sayin, S. Turhan, O. Akyürek, and M. Kilickap. "Gadolinium:nonionic contrast media (1:1) coronary angiography in patients with impaired renal function". In: *Angiology* 58.5 (2007), pp. 561–4 (Cited on page 116).

[Schlather, 2019] Andrea E. Schlather, Paul Gieri, Mike Robinson, Silvia A. Centeno, and Alejandro Manjavacas. "Nineteenth-century nanotechnology: The plasmonic properties of daguerreotypes". In: *Proceedings of the National Academy of Sciences of the United States of America* 116.28 (2019), pp. 13791–13798 (Cited on page 91).

[Schleede, 2013] Simone Schleede. "X-ray Phase-Contrast Imaging at a Compact Laser-Driven Synchrotron Source". PhD thesis. Technical University of Munich, 2013, p. 168 (Cited on pages 32, 34).

[Schlomka, 2008] J. P. Schlomka et al. "Experimental feasibility of multi-energy photon-counting K-edge imaging in pre-clinical computed tomography". In: *Physics in Medicine and Biology* 53 (2008), pp. 4031–4047 (Cited on pages 44, 59).

[Schültke, 2005] E. Schültke et al. "The potential for neurovascular intravenous angiography using K-edge digital subtraction angiography". In: *Nuclear Instruments and Methods in Physics Research A* 548 (2005), pp. 84–87 (Cited on pages 1, 13, 52, 78).

[Schültke, 2011] E. Schültke et al. "Dual energy CT at the synchrotron: A piglet model for neurovascular research". In: *European Journal of Radiology* 79 (2011), pp. 323–327 (Cited on pages 59, 68, 78).

[Shcherbakov, 2013] A. A. Shcherbakov et al. "The Kharkov X-ray Generator Facility NESTOR". In: *IPAC 13 - 4th International Particle Accelerator Conference, May 2013, Shanghai, China*. Vol. in2p3-0082. 2013, pp. 2253–2255 (Cited on page 39).

[Shikhaliev, 2008] Polad M. Shikhaliev. "Computed tomography with energy-resolved detection: a feasibility study". In: *Physics in Medicine and Biology* 53 (2008), pp. 1475–1495 (Cited on page 44).

[Silva, 2009] M. P. Silva, A. Tomal, C. A. Pérez, A. Ribeiro-Silva, and M. E. Poletti. "Determination of Ca, Fe, Cu and Zn and their correlations in breast cancer and normal adjacent tissues". In: *X-Ray Spectrometry* 38 (2009), pp. 103–111 (Cited on pages 1, 101).

[Skarzynski, 2013] Tadeusz Skarzynski. "Collecting data in the home laboratory: Evolution of X-ray sources, detectors and working practices". In: *Acta Crystallographica Section D: Biological Crystallography* 69.7 (2013), pp. 1283–1288 (Cited on page 37).

[Söderman, 2013] Michael Söderman et al. "Image Noise Reduction Algorithm for Digital Subtraction Angiography: Clinical Results". In: *Radiology* 269.2 (2013), pp. 553–561 (Cited on page 11).

[Speck, 2018] Ulrich Speck. *X-Ray Contrast Media - Overview, Use and Pharmaceutical Aspects*. 5th ed. Vol. 18. 3. Springer-Verlag GmbH, 2018, p. 139 (Cited on pages 9, 10).

[Stary, 2000] Herbert C. Stary. "Natural History and Histological Classification of Atherosclerotic Lesions". In: *Aterioscler Thromb Vasc Biol* 20 (2000), pp. 1177–1178 (Cited on page 56).

[Stepanek, 1998] J. Stepanek. "Parametric study of laser Compton-backscattering from free relativistic electrons". In: *Nuclear Instruments and Methods in Physics Research, Section A: Accelerators, Spectrometers, Detectors and Associated Equipment* 412.1 (1998), pp. 174–182 (Cited on page 34).

[Stonestrom, 1981] J. Peter Stonestrom, Robert E. Alvarez, and Albert Macovski. "A Framework for Spectral Artifact Corrections in X-Ray CT". In: *IEEE Transactions on Biomedical Engineering* BME-28.2 (1981), pp. 128–141 (Cited on page 59).

[Stössel, 1985] Rolf-Peter Stössel and Andreas Prange. "Determination of Trace Elements in Rainwater by Total-Reflection X-ray Fluorescence". In: *Analytical Chemistry* 57.14 (1985), pp. 2880–2885 (Cited on page 102).

[Strengell, 2014] S. Strengell et al. "Radiation dose and image quality in K-edge subtraction computed tomography of lung in vivo". In: *Journal of Synchrotron Radiation* 21 (2014), pp. 1305–1313 (Cited on pages 59, 60, 68).

[Strong, 2003] David Strong and Tony Chan. "Edge-preserving and scale-dependent properties of total variation regularization". In: *Inverse Problems* 19 (2003), S165–S187 (Cited on page 74).

[Suhonen, 2008] H. Suhonen, L. Porra, S. Bayat, A. R. A. Sovijärvi, and P. Suortti. "Simultaneous in vivo synchrotron radiation computed tomography of regional ventilation and blood volume in rabbit lung using combined K-edge and temporal subtraction". In: *Physics in Medicine and Biology* 53 (2008), pp. 775–791 (Cited on page 68).

[Suortti, 1993] P. Suortti et al. "A single crystal bent Laue monochromator for coronary angiography". In: *Nuclear Inst. and Methods in Physics Research, A* 336.1-2 (1993), pp. 304–309 (Cited on page 59).

[Suortti, 2000] P. Suortti et al. "Fixed-exit monochromator for computed tomography with synchrotron radiation at energies 18-90 keV". In: *Journal of Synchrotron Radiation* 7.5 (2000), pp. 340–347 (Cited on page 13).

[Takeda, 2011] Akira Takeda et al. "Determination of total contents of bromine, iodine and several trace elements in soil by polarizing energy-dispersive X-ray fluorescence spectrometry". In: *Soil Science and Plant Nutrition* 57 (2011), pp. 19–28 (Cited on page 102).

[Tavakol, 2011] Morteza Tavakol, Salman Ashraf, and Sorin J. Brener. "Risks and Complications of Coronary Angiography: A Comprehensive Review". In: *Global Journal of Health Science* 4.1 (2011), pp. 65–93 (Cited on page 51).

[Thomas, 2016] John V. Thomas et al. "Gadoxetate Disodium enhanced spectral dual-energy CT for evaluation of cholangiocarcinoma: Preliminary data". In: *Annals of Medicine and Surgery* 6 (2016), pp. 17–22 (Cited on page 115).

[Thomlinson, 2018] W. Thomlinson, H. Elleaume, L. Porra, and P. Suortti. "K-edge subtraction synchrotron X-ray imaging in bio-medical research". In: *Physica Medica* 49 (2018), pp. 58–76 (Cited on pages 13, 59).

[Thompson, 1984] A.C. Thompson et al. "Computed tomography using synchrotron radiation". In: *Nuclear Instruments and Methods in Physics Research* 222 (1984), pp. 319–323 (Cited on page 13).

[Thompson, 1989] A.C. Thompson et al. "Coronary angiography using synchrotron radiation (invited)". In: *Rev. Sci. Instrum.* 60.7 (1989), pp. 1674–1679 (Cited on pages 13, 44).

[Tobis, 1983] Jonathan M. Tobis, Orhan Nalcioglu, and Walter L. Henry. "Digital Subtraction Angiography". In: *Chest* 84.1 (1983), pp. 63–86 (Cited on pages 10, 13, 78).

[Torikoshi, 2001] M. Torikoshi et al. "Design of synchrotron light source and its beamline dedicated to dual-energy x-ray computed tomography". In: *Journal of Biomedical Optics* 6.3 (2001), pp. 371–377 (Cited on page 68).

[Torikoshi, 2003] M. Torikoshi et al. "Electron density measurement with dual-energy x-ray CT using synchrotron radiation". In: *Physics in Medicine and Biology* 48 (2003), pp. 673–685 (Cited on pages 13, 68).

[Tsunoo, 2008] Takanori Tsunoo, Masami Torikoshi, Yumiko Ohno, Kentaro Uesugi, and Naoto Yagi. "Measurement of electron density in dual-energy x-ray CT with monochromatic x rays and evaluation of its accuracy". In: *Medical Physics* 35.11 (2008), pp. 4924–4932 (Cited on pages 13, 68).

[Umetani, 1991] K. Umetani et al. "Iodine K-edge dual-energy imaging for subtraction angiography using synchrotron radiation and a 2-dimensional detector". In: *Nuclear Instruments and Methods in Physics Research A* 301 (1991), pp. 579–588 (Cited on pages 13, 41, 44, 52).

[Umetani, 1993] K. Umetani et al. "Iodine filter imaging system for subtraction angiography using synchrotron radiation". In: *Nuclear Instruments and Methods in Physics Research A* 335 (1993), pp. 569–579 (Cited on pages 13, 41, 52).

[Vandenabeele, 2001] Peter Vandenabeele, Francis Verpoort, and Luc Moens. "Non-destructive analysis of paintings using Fourier Transform Raman spectroscopy with fibre optics". In: *Journal of Raman Spectroscopy* 32 (2001), pp. 263–269 (Cited on page 89).

[Variola, 2011] A. Variola. "The ThomX Project". In: *2nd International Particle Accelerator Conference (IPAC'11), Sep 2011, San Sebastian, Spain*. Vol. in2p3-0063. 2011, pp. 1903–1905 (Cited on pages 2, 38, 116).

[Variola, 2014] A. Variola, J. Haissinski, A. Loulergue, and F. Zomer. *ThomX Technical Design Report*. Tech. rep. ThomX, 2014, p. 164 (Cited on page 116).

[Venegas, 2005] Jose G. Venegas et al. "Self-organized patchiness in asthma as a prelude to catastrophic shifts". In: *Nature* 434 (2005), pp. 777–782 (Cited on page 13).

[Vincenzi, 2015] A. Vincenzi et al. "Energy characterization of Pixirad-1 photon counting detector system". In: *Journal of Instrumentation* 10 (2015), p. C04010 (Cited on page 44).

[Williams, 2009] O. Williams et al. "Characterization results of the BNL ATF Compton X-ray source using K-edge absorbing foils". In: *Nuclear Instruments and Methods in Physics Research, Section A: Accelerators, Spectrometers, Detectors and Associated Equipment* 608.1 SUPPL. (2009), pp. 2462–2464 (Cited on page 13).

[Willmott, 2011] P. Willmott. *An Introduction to Synchrotron Radiation: Techniques and Applications*. John Wiley and Sons, Ltd, 2011 (Cited on pages 3, 19–21, 29, 30, 33, 44).

[Winklhofer, 2016] Sebastian Winklhofer et al. "Reduction of peristalsis-related gastrointestinal streak artifacts with dual-energy CT : a patient and phantom study". In: *Abdom Radiol (NY)* 41.8 (2016), pp. 1456–1465 (Cited on page 78).

[Yamada, 2009] K. Yamada et al. "A trial for fine and low-dose imaging of biological specimens using quasi-monochromatic laser-Compton X-rays". In: *Nuclear Instruments and Methods in Physics Research Section A: Accelerators, Spectrometers, Detectors and Associated Equipment* 608.1 (2009), S7–S10 (Cited on page 14).

[Yamamoto, 2009] M. Yamamoto et al. "Development of Digital Subtraction Angiography for Coronary Artery". In: *Journal of Digital Imaging* 22.3 (2009), pp. 319–325 (Cited on pages 10–12, 51, 78).

[Zaichick, 1997] V. Ye Zaichick, T. V. Sviridova, and S. V. Zaichick. "Zinc in the Human Prostate Gland: Normal, Hyperplastic and Cancerous". In: *International Urology and Nephrology* 29.5 (1997), pp. 565–574 (Cited on page 113).

[Zankl, 1997] M. Zankl, N. Petoussi-Henß, G. Drexler, and K. Saito. *The Calculation of Dose from External Photon Exposures Using Reference Human Phantoms and Monte Carlo Methods Part VII: Organ Doses due to Parallel and Environmental Exposure Geometries*. Tech. rep. GSF - Forschungszentrum fuer Umwelt und Gesundheit Neuherberg GmbH, 1997, p. 195 (Cited on pages 8, 9, 64).

[Zeitler, 1992] E. Zeitler. "Digital subtraction angiography (DSA) - Myth or reality?" In: *European Radiology* 2 (1992), pp. 279–281 (Cited on page 11).

[Zhang, 2008] Ming Zhang and Bahadir K. Gunturk. "Multiresolution Bilateral Filtering for Image Denoising". In: *IEEE Transactions on Image Processing* 17.12 (2008), pp. 2324–2333 (Cited on page 74).

[Zhang, 2013] Hua Zhang et al. "Threshold choices of Huber regularization using global- and local-edge-detecting operators for x-ray computed tomographic reconstruction". In: *Proceedings of the Annual International Conference of the IEEE Engineering in Medicine and Biology Society, EMBS* (2013), pp. 2352–2355 (Cited on page 19).

List of Figures

List of Tables

List of Abbreviations

BW ..... bandwidth
CCD ..... charge-coupled device
CLS ..... Compact Light Source
CNR ..... contrast-to-noise ratio
CTDI ..... computed tomography air-kerma dose index
CT ..... computed tomography
CTA ..... computed tomography angiography
DLP ..... air-kerma dose-length product
DNA ..... deoxyribonucleic acid
DSA ..... digital subtraction angiography
ERL ..... energy-recovery linac
FBP ..... filtered backprojection
FEL ..... free electron laser
FOV ..... field-of-view
FOP ..... fiber optical plate
fps ..... frames per second
FT ..... Fourier transform
FWHM ..... full width at half maximum, $[2\sqrt{2\log(2)} \cdot \mathrm{rms}]$
GadOx ..... gadolinium oxysulfide
IAEA ..... International Atomic Energy Agency
ICRP ..... International Commission on Radiological Protection
ICS ..... inverse Compton source
IP ..... interaction point
KES ..... K-edge subtraction
LAD ..... left anterior descending artery
linac ..... linear accelerator
MRI ..... magnetic resonance imaging
NMR ..... nuclear magnetic resonance
PP ..... polypropylene
PVP ..... polyvinylpyrrolidone
PSF ..... point spread function
MuCLS ..... Munich Compact Light Source
RF ..... radio-frequency
rms ..... root mean square
ROI ..... region of interest
SASE ..... self-amplified spontaneous emission
SIR ..... statistical iterative reconstruction
SNR ..... signal-to-noise ratio

TTL ..... transistor-transistor logic
TV ..... total-variation
WHO ..... World Health Organization
XRF ..... X-ray fluorescence
XFM ..... X-ray fluorescence microscopy

List of Publications

First-authored publications (peer-reviewed)

- Stephanie Kulpe, Martin Dierolf, Eva Braig, Benedikt Günther, Klaus Achterhold, Bernhard Gleich, Julia Herzen, Ernst Rummeny, Franz Pfeiffer and Daniela Pfeiffer. "K-edge subtraction imaging for coronary angiography with a compact synchrotron X-ray source". *PLoS ONE* 13(12), e0208446 (2018); doi: 10.1371/journal.pone.0208446

- Stephanie Kulpe. Martin Dierolf, Benedikt Günther, Madleen Busse, Klaus Achterhold, Bernhard Gleich, Julia Herzen, Ernst Rummeny, Franz Pfeiffer and Daniela Pfeiffer. "K-edge Subtraction Computed Tomography with a Compact Synchrotron X-ray Source". *Scientific Reports* 9, 13332 (2019); doi: 10.1038/s41598-019-49899-z.

- Stephanie Kulpe, Martin Dierolf, Eva-Maria Braig, Benedikt Günther, Klaus Achterhold, Bernhard Gleich, Julia Herzen, Ernst Rummeny, Franz Pfeiffer and Daniela Pfeiffer. "K-edge subtraction imaging for iodine and calcium separation at a compact synchrotron x-ray source". *Journal of Medical Imaging* 7(2), 023504 (2020); doi: 10.1117/1.JMI.7.2.023504.

- Stephanie Kulpe, Martin Dierolf, Benedikt Günther, Johannes Brantl, Madleen Busse, Klaus Achterhold, Bernhard Gleich, Franz Pfeiffer and Daniela Pfeiffer. "Dynamic K-edge Subtraction Fluoroscopy at a Compact Inverse-Compton Synchrotron X-ray Source". *Scientific Reports* 10, 9612 (2020); doi:10.1038/s41598-020-66414-x

Co-authored publications (peer-reviewed)

- Benedikt Günther, Regine Gradl, Christoph Jud, Elena Eggl, Juanjuan Huang, Stephanie Kulpe, Klaus Achterhold, Bernhard Gleich, Martin Dierolf and Franz Pfeiffer. "The versatile X-ray beamline of the Munich Compact Light Source: Design, instrumentation and applications". *Journal of Synchrotron Radiation* 27, 1395-1414 (2020); doi:10.1107/S1600577520008309

Oral presentations

- January 2018: "Mono-Energy Coronary Angiography with a Compact Light Source", IMXP 2018, Garmisch-Partenkirchen, Germany.
- March 2019: "K-edge subtraction imaging at the Munich Compact Light Source", European Congress of Radiology, Vienna, Austria.
- April 2019: "K-edge subtraction imaging at a compact synchrotron source", DPG Spring Meeting, Regensburg, Germany.
- August 2019: "K-edge subtraction imaging for angiography at a compact synchrotron source", at Advances in Laboratory-based X-Ray Sources, Optics, and Applications VII, SPIE, San Diego, USA.
- December 2019: "K-edge subtraction imaging with a mono-energetic compact synchrotron X-ray source", at 105^{th} Scientific Assembly and Annual Meeting of the Radiological Society of North America (RSNA), Chicago, USA.

Awards

- April 2019: Best Presentation Award of DPG Radiation and Medical Physics Association at DPG Spring Meeting 2019

Conference Proceedings

- Stephanie Kulpe, Martin Dierolf, Eva-Maria Braig, Benedikt Günther, Klaus Achterhold, Bernhard Gleich, Julia Herzen, Ernst Rummeny, Franz Pfeiffer, Daniela Pfeiffer. "K-edge subtraction imaging for angiography at a compact synchrotron source". Proc. SPIE 11110, Advances in Laboratory-based X-Ray Sources, Optics, and Applications VII, 111100J (9 September 2019); doi: 10.1117/12.2526771.

- Benedikt Günther, Regine Gradl, Christoph Jud, Elena Eggl, Stephanie Kulpe, Eva-Maria Braig, Lisa Heck, Johannes Brantl, Klaus Achterhold, Bernhard Gleich, Martin Dierolf, Franz Pfeiffer. "Evaluation and optimization of multimodal x-ray imaging techniques for inverse Compton x-ray sources". Proc. SPIE 11110, Advances in Laboratory-based X-Ray Sources, Optics, and Applications VII, 1111008 (9 September 2019); doi: 10.1117/12.2529667.

Acknowledgements

Throughout the whole period of this Ph.D. project, I have experienced great support and assistance. Therefore I would like to thank...

- Franz Pfeiffer for giving me the opportunity to do my doctorate at his Chair of Biomedical Physics and letting me work at this unique X-ray source. Thank you for setting up a framework such that I never lacked equipment and financial support and giving me the opportunity to present my findings at various conferences.
- my mentor Daniela Pfeiffer for supporting all of my projects. Your medical expertise and advice made my projects possible in this form in the first place.
- Martin Dierolf for his support with getting the experimental setups and detectors up and running, and for the endless hours he spent troubleshooting MuCLS and IT issues. Thank you for sharing your expertise with me, for the extensive proofreading of all manuscripts and the helpful, enthusiastic discussions and explanations.
- the MuCLS team for the fruitful discussions and motivating working atmosphere. In particular Benedikt Günther, Johannes Brantl and Martin Dierolf for running the MuCLS and their support and advice on implementing any of my experimental ideas.
- Johannes Brantl for building the light barrier system for the dynamic KES experiments. Thank you for your endless support on building CAD drawings of my setup ideas in SolidWorks and saving me a lot of struggles with the programme.
- Benedikt Günther for the critical reading of all of my manuscripts and helping me answer even the most difficult reviewer comments. Thanks a lot for keeping me motivated to write my thesis during corona times.
- Lorenz Hehn and Sebastian Allner for sharing your python knowledge and the patience in explaining the codes to me. Thank you Lorenz for providing the reconstruction algorithms and helping me out when my reconstructions didn't quite look the way they should have.
- Benedikt Günther, Johannes Brantl, Eva Prexl, Lisa Heck, Juanjuan Huang and Martin Dierolf for the thorough proofreading of this thesis.
- Klaus Achterhold and Nelly De Leiris for helping me with all administrative work.
- Korbinian Mechlem for helping me with the dictionary denoising.

- Nikolai Gustschin and Alan Begic for 3D printing and manufacturing everything I needed for my experimental setups.
- Madleen Busse for the support on developing the solid iodine filter and helping me with all chemical questions.
- Lyncean Technologies Inc. for the technical support of the MuCLS both remotely and during the regular service-visits.
- All people who keep our nice IT-infrastructure up and running.
- The whole group for providing this nice working atmosphere. I really enjoyed my time at E17. Not only working with all of you was a pleasure, also the seminar days, the conference visits and the free time activities would have not been the same without you.

Last but not least, I would like to family for their support. Thank you for always being there for me, keeping me motivated when things weren't going as planned, for the critical questions and for giving me new perspectives on the challenges I faced. Thank you, Albrecht, for your love and support and all of your effort in getting the commas in this thesis into place. I couldn't have done it without you!